Performance and Stability Optimization of Solar Fuel Devices

Thesis by

Xinghao Zhou

In Partial Fulfillment of the Requirements for the
degree of
Doctor of Philosophy

CALIFORNIA INSTITUTE OF TECHNOLOGY
Pasadena, California

2018
Defended April 23, 2018

Xinghao Zhou
ORCID: 0000-0001-9229-7670

ACKNOWLEDGEMENTS

I would like to thank my advisor, Prof. Nathan Lewis, who gave me opportunity to do interesting research in his group, as well as a lot of support and directions.

In addition, I also thank Dr. Chengxiang Xiang (CX), who gave me plenty of advice and instruction on my projects.

Many thanks to Kimberly M. Papadantonakis and Bruce S. Brunschwig for helps in my manuscript writing, and also for giving me support during projects.

I also thank my parents, my sister, and my girlfriend Hangwen Lu, all of whom gave me a lot of encourangements.

Many thanks to everyone who spent time on my projects in this thesis; I would like to express special gratitute to people listed below:

Rui Liu and Ke Sun, who taught me how to do electrochemical experiments at the beginning of my PhD career and with whom I collaborated for almost four years. It is really fun to work with you!

Sonja A. Francis, who gave me instruction on CO_2 reduction experiments and product analysis.

Dennis Friedrich, Matthew T. McDowell, Fan Yang, Fadl H. Saadi, Adam C. Nielander and Nathan F. Dalleska, for the technical support.

Yikai Chen, Jingjing Jiang, Sisir Yalamanchili, Ivan Moreno-Hernandez, Paul Nunez, Stefan T. Omelchenko, Pai Buabthong, Michael Lichterman, Ethan Simonoff, Dan Torelli, Weilai Yu, and my PhD labmates, for the great time spent with you!

ABSTRACT

Fossil fuels enabled the Industrial Revolution, and have been the most important power for promoting the world's economic growth ever since. However, burning fossil fuels have also been causing severe air pollution, and global warming is also related to excessive use of fossil fuels. Solar energy is considered to be the largest renewable clean energy resource. The principal problems of solar energy are low energy concentration and intermittency. Storing solar energy in chemical bonds, similar to photosynthesis in nature, is a possible way to overcome these two problems. Carbon-free chemicals, like hydrogen gas produced by solar-driven water splitting, or carbon-neutral chemicals, like methane, ethylene, formic acid, carbon monoxide, etc. produced from solar-driven CO_2 reduction, are all promising clean fuels for solar storage, as they feature high energy/power intensity, are easy and cheap to store and transport, and have direct interface with existing infrastructures.

In this thesis, we focus on improving the efficiency and stability of the solar-driven fuel generation devices, which consist of (photo-)anode and (photo-)cathode. For the anode part, cobalt oxide Co_3O_4 ultrathin (2 nm) films by atomic layer deposition (ALD) were deposited onto silicon photoanode prior to deposition of thick nickel oxide (NiO_x) layers. The photovoltage of the photoanode increased from 200 mV to 580 mV after including the interfacial Co_3O_4 layer, and the anode was stable in 1.0 M KOH(aq) for 1700 hours, which was equivalent to one year of operation in the field at a maximum photocurrent density of 30 mA cm^{-2} assuming a 20% solar capacity factor. Furthermore, the non-uniform sputtered NiO_x layer of the n-Si/SiO_x/Co_3O_4/NiO_x photoanode was removed, and the 2 nm Co_3O_4 film was thickened to 50 nm, and the stability of n-Si/SiO_x/50 nm$-Co_3O_4$ was improved to 2500 hours with lower efficiency decay rate. For the cathode part, an optimized Pd/C nanoparticle coated Ti mesh cathode exhibited < 100 mV overpotential at 8.5 mA cm^{-2} current density, and > 94% Faradaic efficiency for the reduction of 1 atm of CO_2(g) to formate in 2.8 M $KHCO_3$. A solar-driven CO_2 reduction (CO_2R) cell was constructed with this cathode, showing 10% solar-to-fuels conversion efficiency.

This thesis can be divided into three parts. The first part discusses importance of solar fuels, as well as gives an introduction of solar-fuel generators. The second part includes Chapter II and Chapter III, which deal with performance improvement of silicon photoanode with ALD Co_3O_4 thin films. The third part is Chapter IV, in which we study the cathode for CO_2 reduction to formate, and demonstrate a 10% efficiency solar-driven CO_2 reduction cell with the cathode.

PUBLISHED CONTENT AND CONTRIBUTIONS

[1] X. Zhou et al. "Interface Engineering of the Photoelectrochemical Performance of Ni-oxide-coated n-Si Photoanodes by Atomic-Layer Deposition of Ultrathin Films of Cobalt Oxide". In: *Energy Environ. Sci.* 8.9 (2015), pp. 2644–2649.
DOI: 10.1039/C5EE01687H. X.Z. participated in the concept of the project, deposited cobalt oxide ALD thin films and nickel oxide thin films, prepared data for electrochemical measurements, Kelvin probe force microscope (KPFM), external quantum efficiency, etc., and participated in writing the manuscript.

[2] X. Zhou et al. "570 mV Photovoltage, Stabilized n-Si/CoOx Heterojunction Photoanodes Fabricated using Atomic Layer Deposition". In: *Energy Environ. Sci.* 9.3 (2016), pp. 892–897.
DOI: 10.1039/c5ee03655k. X.Z. participated in the concept of the project, materials deposition, prepared data for electrochemical measurements, transmission electron microscope (TEM), external quantum efficiency, etc., and participated in writing the manuscript.

[3] X. Zhou et al. "Solar-Driven Reduction of 1 atm of CO2 to Formate at 10% Energy-Conversion Efficiency by Use of a TiO2-Protected III-V Tandem Photoanode in Conjunction with a Bipolar Membrane and a Pd/C Cathode". In: *ACS Energy Letters* 1.4 (2016), pp. 764–770.
DOI: 10.1021/acsenergylett.6b00317. X.Z. participated in the design of the photoelectrochemical cell, electrodes preparation, prepared data for electrochemical measurements, electrolyte ion leakage tests, and participated in writing the manuscript.

[4] K. Sun et al. "Stable Solar-Driven Oxidation of Water by Semiconducting Photoanodes Protected by Transparent Catalytic Nickel Oxide Films". In: *Proc. Natl. Acad. Sci. U.S.A.* 112 (2015), pp. 3612–3617.
DOI: 10.1073/pnas.1423034112. X.Z. participated in electrodes preparation, and experiment discussion.

[5] X. Zhou et al. "Solar-Driven Reduction of 1 atm CO2 to Formate at 10% Energy-Conversion Efficiency by Use of a TiO2-Protected III-V Tandem Photoanode in Conjunction with a Bipolar Membrane and a Pd/C Cathode Electrocatalyst". In: *ECS Transactions* 77.4 (2017), pp. 31–41.
DOI: 10.1149/07704.0031ecst. X.Z. participated in the experiment design, electrodes preparation, electrochemical data preparation, and participated in writing the manuscript.

[6] K. Sun et al. "A Comparison of the Chemical, Optical and Electrocatalytic Properties of Water-oxidation Catalysts for Use in Integrated Solar-fuel Generators". In: *Energy Environ. Sci.* 10.4 (2017), pp. 987–1002.
DOI: 10.1039/C6EE03563A. X.Z. participated in the electrodes preparation and experiment discussion.

TABLE OF CONTENTS

LIST OF ILLUSTRATIONS

LIST OF TABLES

Chapter 1

INTRODUCTION

1.1 The importance of the solar-to-fuel conversion system

Demand for fossil fuels

The energy demand has experienced an explosive growth since the Industrial Revolution. And to support the current economy and population growth, we are still using a large amount of energy and will continuously increase our energy demand in the next two decades as shown in Figure 1.1. Of all the fuels we are currently using, 80% are fossil fuels [1], which emit an enormous amount of carbon dioxide and pollutants including Particulate Matter 2.5 (PM2.5, atmospheric particulate matter with a diameter of less than 2.5 micrometers), sulfides, and nitrides into the atmosphere, and cause severe environmental issues.

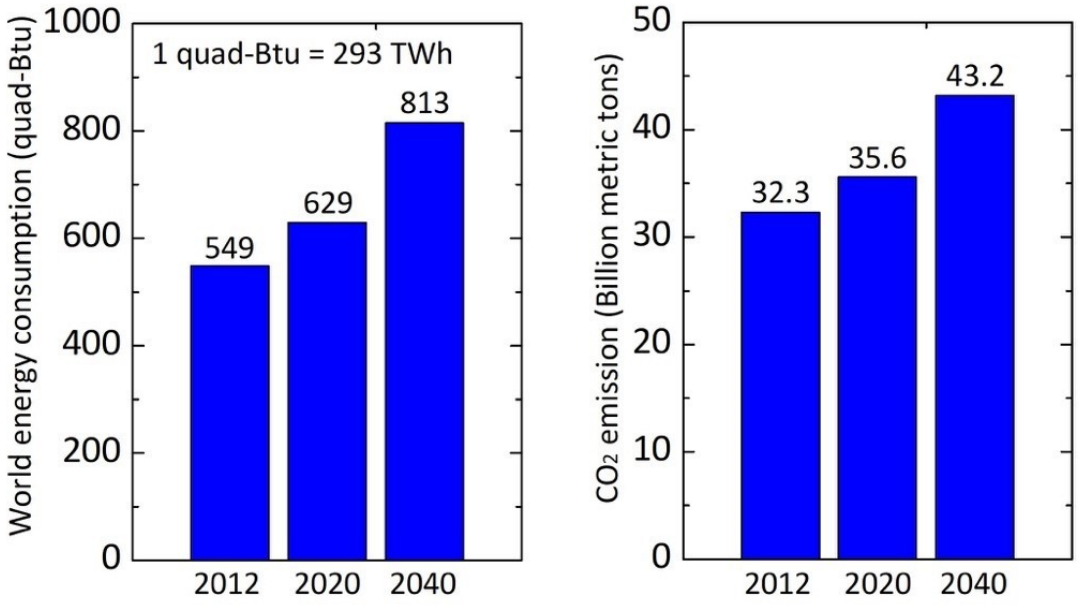

Figure 1.1: World energy consumption and CO_2 emission from 2012 to 2040. (Plotted with data from source [1])

Burning fossil fuels and global temperature increase

Excessive use of carbon-based fossil fuels in recent periods have been releasing large amounts of carbon dioxide into the atmosphere that have been stored in coal and oil underground for hundreds of millions of years. As seen in Figure 1.2, the anthropogenic greenhouse gas (GHG) emissions have increased from 27 $GtCO_2$-eq/yr in 1970 to 49 $GtCO_2$-eq/yr in 2010, with 1.3%/yr increase rate from 1970 to 2000, and 2.2%/yr increase rate from 2000 to 2010. And 78% of the total GHG emissions increase from 1970 to 2010 came from emissions of CO_2 from fossil fuel combustion and industrial processes.

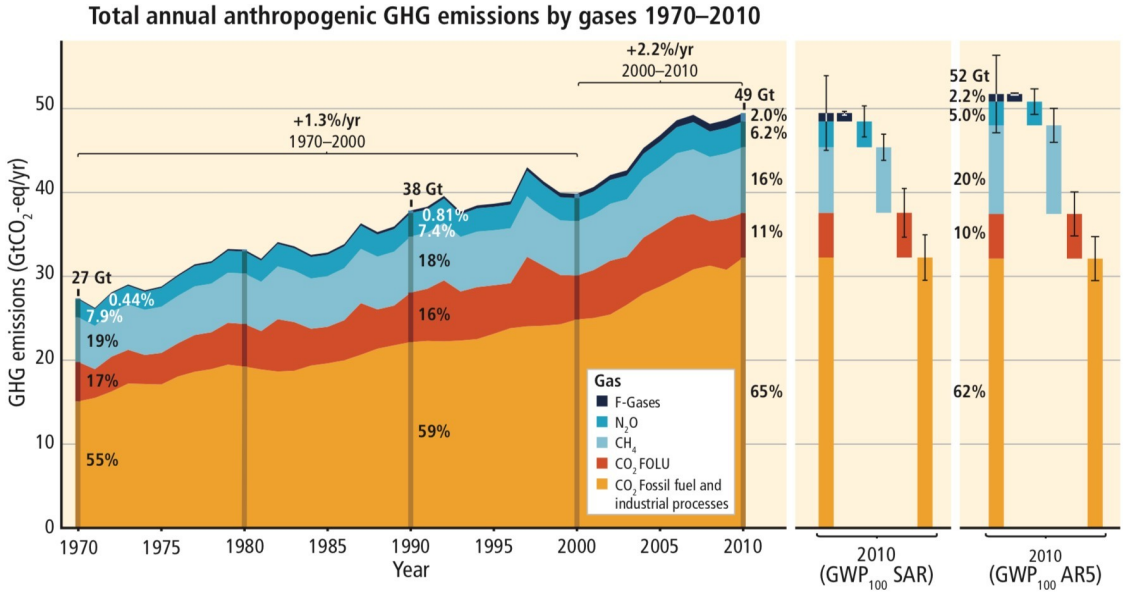

Figure 1.2: Total annual anthropogenic greenhouse gas (GHG) emissions (gigatonne of CO_2-equivalent per year, $GtCO_2$-eq/yr) for the period 1970 to 2010 by gases: CO_2 from fossil fuel combustion and industrial processes; CO_2 from Forestry and Other Land Use (FOLU); methane (CH_4); nitrous oxide (N_2O); uorinated gases covered under the Kyoto Protocol (F-gases). Right hand side shows 2010 emissions, using alternatively CO_2-equivalent emission weightings based on IPCC Second Assessment Report (SAR) and AR5 values. (Reprinted with permission from ref [2].)

With the rapid increase of the CO_2 emissions from fossil fuel combustion and industrial processes in the recent decades, the CO_2 concentration in atmosphere has increased rapidly, especially after the 1970s [3]). The observed CO_2 385 parts per million (ppm) concentration in 2008 is about 30 % more than the highest level in the past 800000 years [3]. The CO_2 concentration will continue to increase to 550 ppm in 2100 with a lower emissions scenario and 900 ppm in 2100 with a higher emission scenario [3]. The trend of global annual average temperature change is also strongly correlated with change of CO_2 concentration in the atmosphere [3].

With the increase of the global temperature, the ocean water expands and takes up more space, and, even more importantly, the glaciers and ice sheets start to melt and add more water into the sea, all of which result in the rise of the sea level. Over the past century, the sea level has risen by 8 inches. Satellite data shows that the speed of the sea level rising has double over the past 15 years compared to that observed in the past century [4].

Burning fossil fuels and ocean pH decrease

About 30% of the emitted anthropogenic CO_2 will be absorbed by the ocean [1], which causes ocean acidification. Ocean acidification may impact coral reefs[5], calcareous plankton[6], and other species that contain calcium carbonate. Figure 1.3 shows the emission scenario, corresponding CO_2 concentration in atmosphere, and ocean pH change based on horizontally averaged chemistry from 1750 to 3000 [7]. The CO_2 emission data from 2000 to 2100 are from the Intergovernmental Panel on Climate Change's IS92a scenario [8]; and the emission data after 2100 follows a logistic function assuming 5270 GtC in 1750. Under this emission scenario, the atmospheric CO_2 concentration will go to almost 2000 ppm in about the year of 2250, and the ocean surface pH change will reach -0.7, which means a 5 times increase of proton concentration in the ocean. Increase of proton concentration may impact the environment of the surface of ocean, where most marine organisms live.

Burning fossil fuels and air contamination

Besides carbon, fossil fuels also contain sulfur and nitrogen elements, which will form SO_2 and NO_x pollutants, which cause significant irritation to the upper respiratory tract. What's more, SO_2 and nitrogen containing chemicals will form fine particulate matter (<2.5 um) (PM2.5) after a series of atmospheric chemistry reactions:

$$SO_2 + H_2O = H_2SO_3$$
$$H_2SO_3 + O_2\ (O_3) = H_2SO_4$$
$$H_2SO_4 + NH_3 = NH_4HSO_4$$
$$H_2SO_4 + 2NH_3 = (NH_4)_2SO_4$$
$$HNO_3 + NH_3 = NH_4NO_3$$

Although PM2.5 has a relatively small diameter, it has larger specific surface area, higher activity, and absorbs poisonous chemicals more easily, compared to other larger

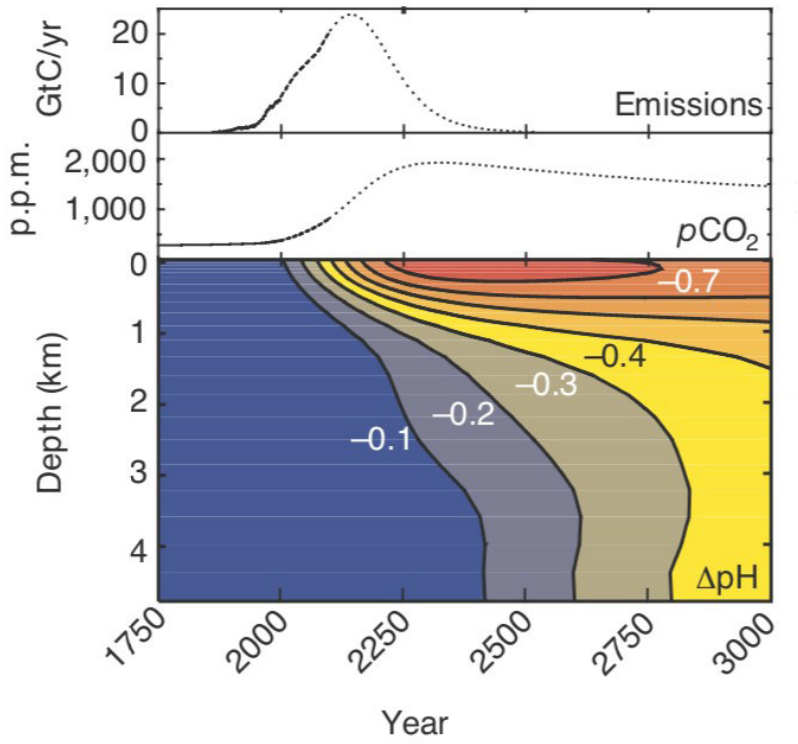

Figure 1.3: Atmospheric release of CO_2 from the burning of fossil fuels may give rise to a marked increase in ocean acidity. Atmospheric CO_2 emissions, historical atmospheric CO_2 levels, and predicted CO_2 concentrations from this emissions scenario, together with changes in ocean pH based on horizontally averaged chemistry (gigatonnes of carbon = GtC). (Reprinted with permission from ref [7]. Copyright 2003 Nature.)

particulates. Besides, PM2.5 is able to stay for longer time travel longer distances in air. Therefore, PM2.5 has a greater impact on the atmospheric environment and human health.

Figure 1.4 shows a real time air quality index visual map at 21:49 on March 11, 2018. Most of the East Asia, North America, and Western Europe are covered by yellow, red, and even purple and brown marks, which indicate heavy pollution, especially areas in China, Indian, and some places in the west part of North America. It is very urgent that strong action needs to be taken to curb the deteriorating trend of air pollution for the good of our next generation.

Renewable energy

Renewable energy includes solar, hydro, wave, geothermal, wind, nuclear, etc. Traditional nuclear fission energy is not exactly renewable energy source. U-235 source on earth is limited and will be depleted if fission energy is used as the main source of energy

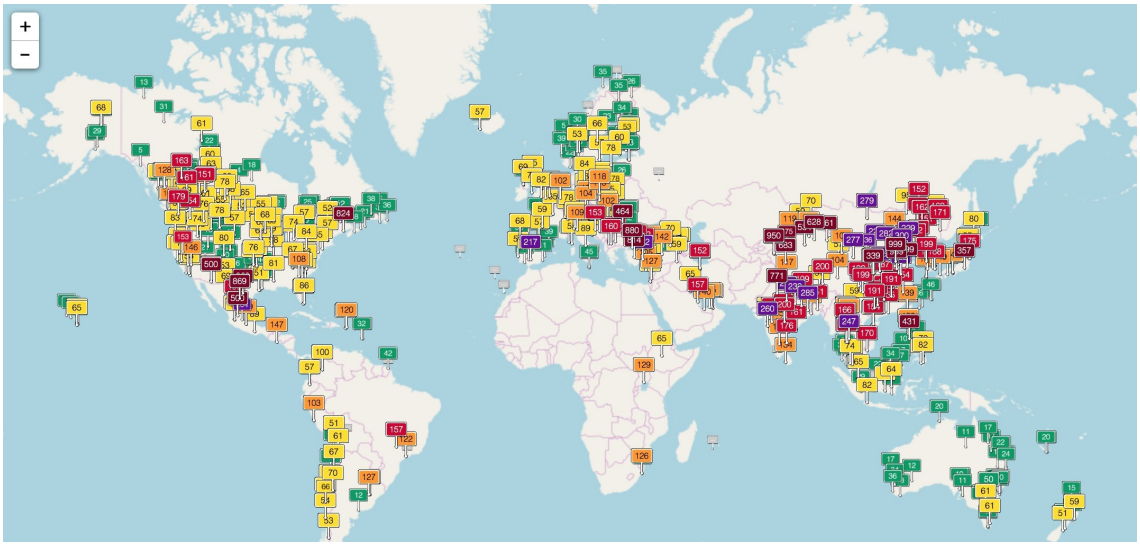

Figure 1.4: Air quality index visual map at 21:49 on March 11, 2018. (From http://aqicn.org/map/world/)

by human being. Besides, the dangerous nuclear waste from the traditional fission energy also imposes a high risk to the environment. Nuclear fusion energy, on the other hand, may possibly provide endless clean energy in the future, but controlled fusion energy release is still in the early stage of research, and will not provide energy to human beings in the near future.

Of the other renewable energy, solar energy is the most abundant clean energy on the earth. The solar energy flux reaching the earth is about 100,000 TW, and 36,000 TW of the energy reaches the land [9]. Table 1.1 shows that the power supplied by the sun is four orders of magnitude higher than hydro, wave, geothermal, and biomass energy, two orders of magnitude higher than wind energy, and three orders of magnitude higher than the world consumption rate. The solar energy will satisfy the world energy demand if we are capable of utilizing this infinite and clean energy source.

Solar energy needs to be stored

Though abundant, solar energy also has problems of intermittency and low power density. The utilization of the solar energy is restricted by diurnal variation, seasonal change, geographic latitude, and altitude. Figure 1.5 shows a power output curve from a 4.5 MW solar PV array in northeastern Arizona by Tuscon Electric power [12], and a utility load curve during the day. The fluctuations of the power output curve are due to intermittency of solar energy supply, like intermittent cloudy weather, which makes it difficult for continuous and sufficient power supply. What's more, the sun provides peak

Renewable energy	Power supply/consumption (TW or TWy/y)
Solar reaching on land	36000
Hydro	3-4
Wave	0.2-2
Geothermal	0.2-3
Wind	75-130
Biomass	2-6
World consumption	18.3

Table 1.1: Comparison of power supply of different renewable energy, and world energy consumption in 2014 (Data from source [10, 11])

power in the middle of the day, while the utility load reaches its maximum at about 16, and remains at a high level after the sunset. The mismatch of the demand and supply is difficult to compromise without storage of the solar energy. Storage helps the introduction of solar energy to our existing energy systems, provides flexibility to the power grid and balance the solar energy supply and demand.

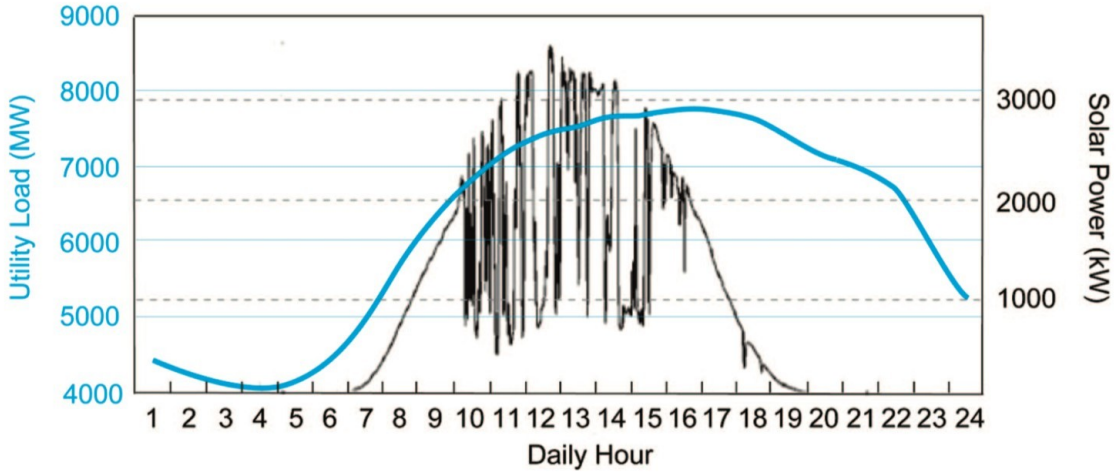

Figure 1.5: Utility load versus solar power output. Overlaid on demand curves is the power output (kW) sampled every minute for a 4.6 MW solar PV array in northeastern Arizona over the period of one day. (Reprinted with permissions from ref [12, 13]. Copyright 2010 American Chemical Society and copyright 2007 John Wiley and Sons)

We can use giant batteries to store solar energy, like flow batteries, zinc-air, and lithium-ion batteries. However, large scale energy storage using giant batteries is difficult due to high cost, short service life, or poor performance of batteries.

Looking back to the fossil fuels, we have been using them because they feature high

energy density, power density, and durability, and are easy to transport and storage. Therefore, we can use the chemical fuel as a cheap battery, and store the solar energy in the chemical bonds.

If we can store solar energy by converting water and carbon dioxide into chemical fuels at high efficiency, low cost, and high rate for a long time (Figure 1.6), we can realize carbon-neutral goal in the case of carbon-based fuels from CO_2, and carbon-free goal in the case of hydrogen fuel from water. The generated clean chemical fuels have the same high power and energy density as traditional fossil fuels, are easy to store and transport, and have direct interface with existing infrastructures. For example, we can provide high energy density fuels to heavy duty vehicles that cannot be driven electrically.

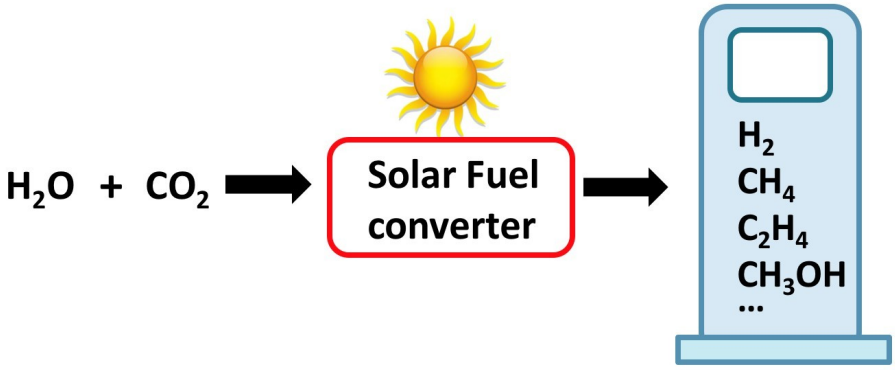

Figure 1.6: Scheme of solar-to-fuel conversion

1.2 Solar fuel conversion system

There are mainly two types of integrated system: one is electrode based and the other is particle based. This thesis focuses on electrode based integrated system. Most of the solar-to-fuel conversion system consists of (photo)anode, (photo)cathode, and an ion exchange membrane. At least one of the two electrodes has a light absorber for solar energy harvest. The membrane in the system serves as a gas and electrolyte separator. Common membranes include the cation ion exchange membrane, anion exchange membrane, and bipolar membrane. Chapter IV will discuss these membranes in detail.

Figure 1.7 shows a highly integrated photoelectrochemical system for water splitting. The light absorbers are fabricated into microwire array to reduce the material usage and purity requirements because of the orthogonalized directions between light and minority-carrier collection [14–19]. Besides, compared to planar light absorbers microwires array shows stronger broadband absorption[20–24], and can hold more catalyst per geometry area due to increased surface area[25, 26]. The anode wires are coated with oxygen

evolution reaction (OER) catalysts where the reaction below occurs:

$$2H_2O = O_2 + 4H^+ + 4e^-$$

The protons migrate across the ion exchange membrane and are reduced to hydrogen by the electron transferred to the cathode:

$$2H^+ + 2e^- = H_2$$

The overall reaction:

$$2H_2O = 2H_2 + O_2,\ E = 1.23V$$

If CO_2 reduction occurs at the cathode, and CO_2 is reduced to CH_3OH, for example:

$$CO_2 + 6e^- + 6H^+ = CH_3OH + H_2O$$

Then the following overall reaction occurs:

$$2CO_2 + 4H_2O = 2CH_3OH + 3O_2$$

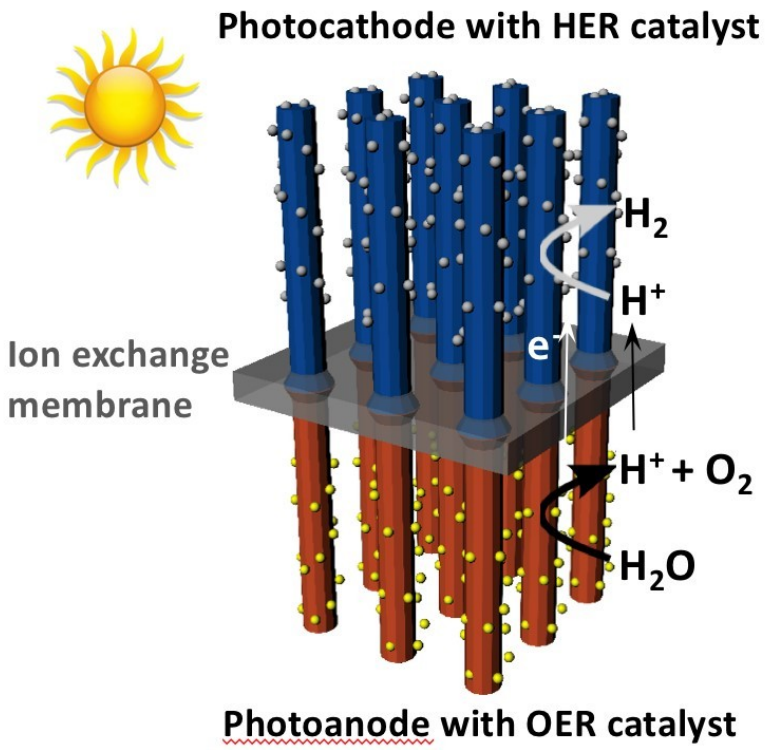

Figure 1.7: Scheme for a highly integrated photoelectrochemical system. (Adapted with permission from ref [27]. Copyright 2011 Royal Society of Chemistry.)

An efficient system with the structure shown in Figure 1.7 has not been fabricated yet. Integrated systems usually show limited performance due to low efficiency, high cost, and poor stability. More advanced light absorbers, catalysts, interfaces between light absorbers and catalysts, and new systems need to be discovered for better performance.

Though solar conversion systems with microwires as Figure 1.7 are the ultimate design for solar energy storage, a more straightforward planar system (Figure 1.8) can be implemented to study the behavior of light absorbers and catalysts, along the path towards improved performance of solar-to-fuel conversion system. This thesis discusses performance and stability study of anode (Chapter II and III), cathode (Chapter IV), and membrane (Chapter IV), and a brief research background of these components will be introduced in the following sections.

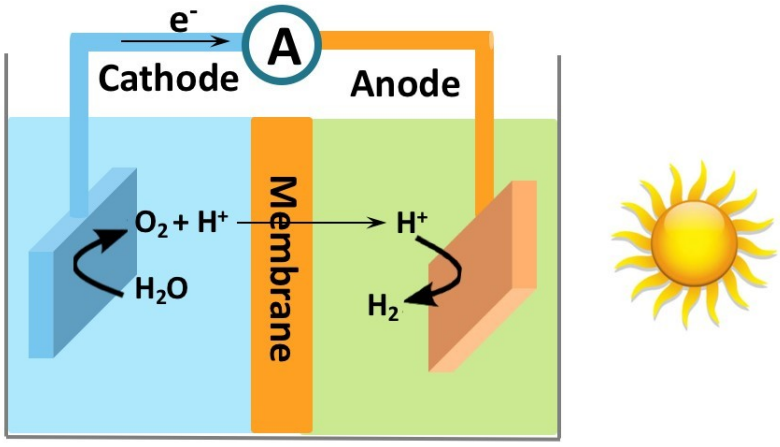

Figure 1.8: Scheme for planar photoelectrochemical system

1.3 Anode

Water oxidation is an important process of solar fuel generation, including both water oxidation and CO_2 reduction[28, 29]. It is considered to be a kinetic bottleneck for water splitting or CO_2 reduction due to the relatively high activation energy required[28]. Therefore, efforts towards new and efficient catalysts for water oxidation should be taken to reduce the OER overpotential.

For the photoanode, efforts towards long semiconductor stability should be made for optimal photoanode lifetime. In this thesis, we study protection of small bandgap semiconductors as they are important as the bottom junction of the tandem cells. Silicon, III-V semiconductors such as GaAs, InP, and II-VI semiconductors such as CdTe all are promising candidates for bottom junction cell. However, these semiconductors are prone to corrode in strong acid or base under photoanodic condition[30]. Therefore, a layer of

stable and transparent metal oxide on top of the semiconductor can be used to protect the surface of semiconductor from corrosion in aqueous solution.

Another aspect of photoanode that needs to be considered is the semiconductor/catalyst interface, which should be well engineered for optimal photoanode photovoltage and efficiency. The heterojunction of semiconductor/catalyst can be tuned by deposition of metal oxides with different work functions, which is the main research focus of Chapter II.

The above three aspects of anode all require metal oxides with suitable properties. An ideal metal oxide should show good catalytic activity, protect the underlying semiconductor, and engineer the semiconductor interface for high photovoltage. The research regarding such a metal oxide will be discussed in Chapter III.

In this section, the properties of an excellent OER catalyst that is utilized in my research will be introduced, followed by a brief introduction of other OER catalysts, as well as the discussion of photoanode interface for photovoltage improvement.

NiO_x as OER catalysts

Sun et al. reported a transparent, anti-reflective, highly conductive, highly OER active and chemically stable nickel oxide film by reactive sputtering method. The NiO_x catalyst showed 330 mV overpotential at 10 mA cm^{-2} in 1.0 M KOH [30, 31], but it is important to note that about ten cyclic voltammetry scans were required to activate the NiO_x catalyst to desired OER activity[31]. XPS study showed trace amount of Fe was found on the surface of KOH-treated NiO_x film, which may contribute to the OER activity improvement. Recent research also found similar phenomena and studied the effect of Fe impurity on NiO_x activity [32–36]. Therefore, "NiO_x" film should be nickel iron oxide, but in this thesis, we will call it NiO_x for short.

In addition to OER activity, catalysts need to be transparent and anti-reflective so that the light-absorber can utilize as much of the visible light as possible. Figure 1.9A shows that a 150 nm thick sputtered NiO_x film by Sun et al. is more transparent than a 15 nm Ni film. Furthermore, Sun et al. also calculated that a 75 nm NiO_x coating on Si, CdTe, and amorphous silicon (a-Si) would lead to reflection suppression at the visible wavelength region, both in water and in air medium (Figure 1.9B and 1.9C). Therefore, most of the NiO_x coating in this thesis is around 75 nm.

The sputtered NiO_x is highly stable, and can protect np^+-Si from corrosion for 1200 hours, n-CdTe for 1000 hours, heterojunction silicon device (HTJ-Si), and a-Si for 100

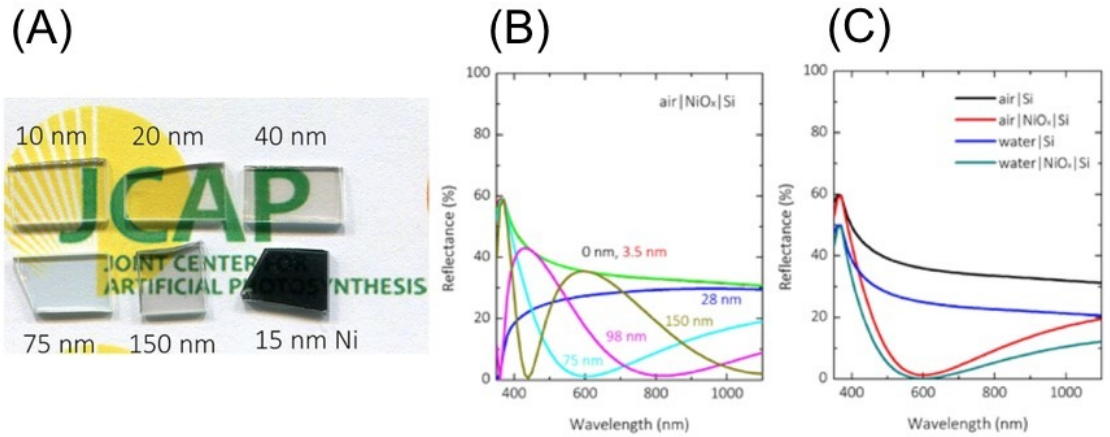

Figure 1.9: (A) Optical images of NiO_x films with various thicknesses and of 15-nm metallic Ni on quartz substrates. (B) Reflectance from air/NiO_x/Si interfaces with varied thickness of NiO_x (C) Reflectance showing the effect of the incident media (water versus air) from media/NiO_x/Si and media/Si interfaces. (Reprinted with permission from ref [30]. Copyright 2015 National Academy of Sciences)

hours, as well as np^+-InP for 48 hours in 1.0 M KOH under 1 sun illumination [30, 31, 37].

It is found that sputtered NiO_x layer is not uniform[38] and alkaline solution have direct contact with the semiconductor surface. However, the photoanode protected with NiO_x still showed much longer stability compared to photoanode without protection. Sun et al. claimed that it was due to the semiconductor passivation effect. When in contact with the alkaline solution under anodic bias, exposed surface of some semiconductors would form non-soluble oxides to prevent further corrosion, and the charge would pass from semiconductor with protection to the conducting protection layer (Figure 1.10). Silicon oxide from silicon, cadmium (III) oxide from CdTe, and indium(III) oxide from InP are alkaline stable oxides, and therefore can protect these semiconductors from further corrosion. However, both gallium oxide or arsenic oxide from GaAs are soluble in KOH, and thus GaAs cannot passivate in strong alkaline solution, and NiO_x is not able to provide protection for GaAs against corrosion in strong alkaline solution.

Other OER catalysts

Typical OER catalysts in alkaline solutions are summarized in Table 1.2 [39]. Other catalysts for OER in alkaline solutions may show lower OER overpotential than the sputtered NiO_x film by Sun et al.[30, 31, 40], for example, the NiFe oxide synthesized with electrodeposition by Merrill and Dougherty showed only 30 mV overpotential at 1

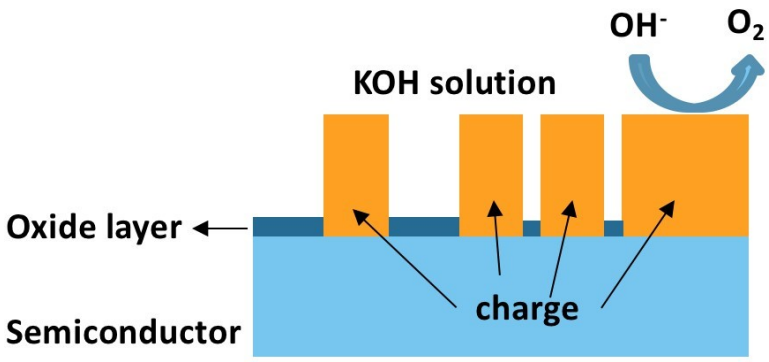

Figure 1.10: Scheme for semiconductor passivation

mA cm^{-2} or 300 mV overpotential at 500 mA cm^{-2} [39, 41], which is the record OER performance up to now. However, the electrodeposited $NiFeO_x$ is not transparent and may not be suitable for use as a photoanode catalyst coating.

Catalyst	Overpotential (mV) at 10 mA cm^{-2}	pH	Reference
NiO_x	330	14	[31]
$NiFeO_x$	30 (1 mA cm^{-2})	14	[41]
Co_3O_4	433	14	[42]
CoO_x	390 (1 mA cm^{-2})	9.2	[43]
CoP	345	14	[44]
FeCoW oxyhydroxides	191	14	[45]
MnO_x	300 (1 mA cm^{-2})	14	[46]
CoMP	330	14	[47]

Table 1.2: Typical OER catalysts in alkaline solutions. (From source [39])

Many of the nickel containing catalysts show decent OER activity [32–36, 48, 49]. For the nickel-free catalysts, a FeCoW oxyhydroxides OER catalyst with 191 mV overpotential at 10 mA cm^{-2} was reported in 2016 by Zhang et al.[45]. The authors predicted that non-3d high valence band metals such as tungsten can modulate 3d metal oxides, such as cobalt and iron, to provide near-optimal adsorption energies for OER intermediates. Then they synthesized gelled and homogeneous FeCoW oxyhydroxides at room temperature, which showed high OER activity and 500 hours of stability in 1.0 M KOH under water oxidation operation.

The catalysts discussed above are all alkaline stable OER catalysts, and the photoanode in this thesis focuses on alkaline stable systems. But it is worthwhile to mention OER

catalysts that operate in acid. Research of OER stable catalysts are challenging, due to the fact that metal oxides are more likely to dissolve in acid than in alkaline solutions, especially under anodic bias. Moreno-Hernandez et al. reported an earth-abundant crystalline nickel manganese antimonate as an acid stable OER catalyst in 1.0 M H_2SO_4 in 2017[50]. The catalyst was prepared by sputter deposition, followed by annealing at 700 C, which greatly improved the acid stability. The authors showed that the catalyst was stable for 168 hours of continuous operation at 10 mA cm^{-2} with little degradation, which was a big improvement compared to the previous work regarding IrO_x and RuO_x[51, 52], even though the overpotential reached about 700 mV.

Photoanode interface

n-Si photoanode with sputtered NiO_x showed months of stability in 1.0 M KOH under 1 Sun conditions[31]. However, n-Si/NiO_x showed low open-circuit voltage (V_{oc}) due to non-optimal interface energetics between n-Si and protection layer. Although NiO_x protected np^+ buried homojunctions can be made to obtain much higher V_{oc} values, many semiconductors for photoelectrochemistry cannot be doped to form high quality homojunctions. Besides, homojunctions for semiconductor microwire and nanowire structures, which are promising structures for highly integrated photoelectrochemical system as Figure 1.7 shows, are difficult to fabricate, especially for GaAs and InP semiconductors. Therefore, interface study of a high quality heterojunction photoanode becomes important.

Figure 1.11 shows the band diagram change before and after the semiconductor is in equilibrium with the redox pair in liquid, as well as the change after the junction is illuminated [28]. After the n-type semiconductor contacts the liquid containing redox pair (A/A^-), the electrons will flow from the conducting band edge to the liquid until equilibrium is established. A region with positive charge and width W is present in the semiconductor, and the resulting electrostatic potential balances the initial electrochemical potential difference between the semiconductor and the liquid [28, 53]. The electrostatic potential versus distance curve looks the same as the bending as shown in Figure 1.11B. Under steady-state illumination, the electrons and holes are not in equilibrium, but in quasi-thermal equilibrium. The quasi-Fermi levels are descriptions of electrochemical potential that are calculated from Fermi-Dirac statistics [28, 54–57]. As Figure 1.11 shows, both the barrier height and the V_{oc} are directly related to the electrochemical potential $-qE^\circ(A/A^-)$. Lower $-qE^\circ(A/A^-)$ would theoretically lead to higher photoanode V_{oc}, if not considering other effects.

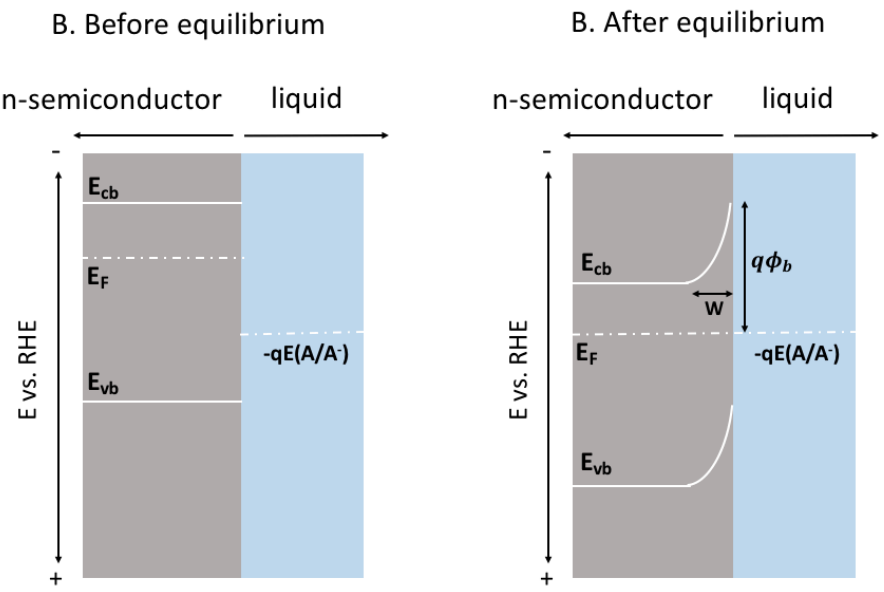

Figure 1.11: The band energetics of a semiconductor/liquid contact are shown in three cases: (A) before equilibration between the two phases; (B) after equilibration in the dark [28]. $q\phi_b$ is the barrier height, and its magnitude determines the theoretical maximum energy that can be extracted from a separated electron-hole pair at the semiconductor/liquid junction [28]. The open-circuit voltage of the semiconductor under light is related with the barrier height.

The band bending diagram of solid semiconductor junction is the same as Figure 1.11, except that the electrochemical potential $-qE^{\circ}(A/A^{-})$ should be the Fermi level of the solid film on the semiconductor. Photoanode with metal or metal oxides of higher work function should exhibit higher V_{oc} values, however, the surface states on the semiconductor/metal or metal oxides junction, if present, would buffer the semiconductor from electrochemical potential change, which is referred to as Fermi level pinning [53]. Fermi level pinning would significantly lower the V_{oc} values of photoanodes, even though high work function metal or metal oxides are coated on the semiconductors.

Table 1.3 shows previous research on improving the V_{oc} values of heterojunction semiconductor/metal or metal oxide. The definition of solar-to-O_2(g) conversion efficiency is introduced in Appendix A.1. Some photoanodes show decent V_{oc}, for example, n-Si/SiO_x/TiO_2/Ir [58] and n-Si/SiO_x/Ni [59] photoanodes; however, due to high resistance of the oxide layer, the fill factor of the current-voltage curve is low, resulting in low solar-to-O_2(g) conversion efficiency. The n-Si photoanode protected by sputtered NiO_x show 1000 hours stability of continuous operation in 1.0 M KOH under 1 Sun condition, however, due to non-optimal interface energetics, the V_{oc} value is low, and the solar-to-

O_2(g) conversion efficiency is nearly zero. Therefore, further research on engineering of semiconductor/metal or metal oxide interface while maintaining long time stability is desired.

Photoanode	Solar-to O_2(g) conversion efficiency (%)	V_{oc} (mV)	Stability	Reference
n-Si/SiO_x/TiO_2/Ir	~ 0.3	550	< 24 h	[58]
n-Si/SiO_x/Ni	~ 0.2	500	< 24 h	[59]
n-Si/SiO_x/TiO_2/Ni	~ 0.4	400	~ 100 h	[60]
n-Si/SiO_x/NiFe	N.A.	280	N.A.	[61]
n-Si/NiO_x	~ 0.	200	~ 1000 h	[31]

Table 1.3: Previous research of heterojunction photoanodes

1.4 Membrane

Most of the membranes used for photoelectrochemical water splitting or CO_2 reduction include cation exchange membranes (CEM) such as Nafion membrane, anion exchange membrane (AEM), and bipolar membrane (BPM), which are introduced below.

Cation exchange membrane and anion exchange membrane

CEM has negative fixed ions with positive free ions, and thus it only allows cations to go through and block anions. Similarly, AEM has positive fixed ions with negative free ions, and thus it only allows anions to go through and block cations. Both membranes block gas molecules, and therefore AEM and CEM separate the products generated by the anode and cathode, preventing the formation of explosive mixtures during water splitting or CO_2 reduction. However, photoelectrochemical cells with AEM or CEM may develop a pH gradient between the anode and cathode chamber, and thus increase the overall voltage required to drive the reaction. Figure 1.12 shows the scheme for ion generation, reaction, and transfer for CO_2 reduction cells with CEM and AEM membrane. Take CO_2 reduction to CH_4 as an example, and the cathode reaction below occurs:

$$CO_2 + 8e^- + 6H_2O = CH_4 + 8OH^-$$

When 8 electrons are passed to reduce CO_2, 8 OH^- ions are produced on the cathode, 8 OH^- ions are produced into the catholyte, 8 K^+ ions go across the CEM, and 8 OH^- ions are oxidized into 2 O_2 molecules and 4 H_2O molecules:

$$8OH^- - 8e^- = 2O_2 + 4H_2O$$

Therefore, the pH in the catholyte will increase, and the pH in the anolyte will decrease, resulting in a increase of the overall cell voltage. Vermaas et al. in 2016 showed this phenomenon in the CO_2 reduction to CO device with Ag as the catalyst, and Nafion as the membrane [62]. They found that the pH in the anolyte started decreasing right after the current was applied, and was stable at about pH 2 (Figure 1.13). The pH in the catholyte was stable at around pH 7 because CO_2 was continuously purging into the catholyte. Waste of CO_2 needs to be paid for stable pH. The pH gradient formation is similar for AEM, except that HCO_3^- ion crosses the AEM, instead of K^+ ion.

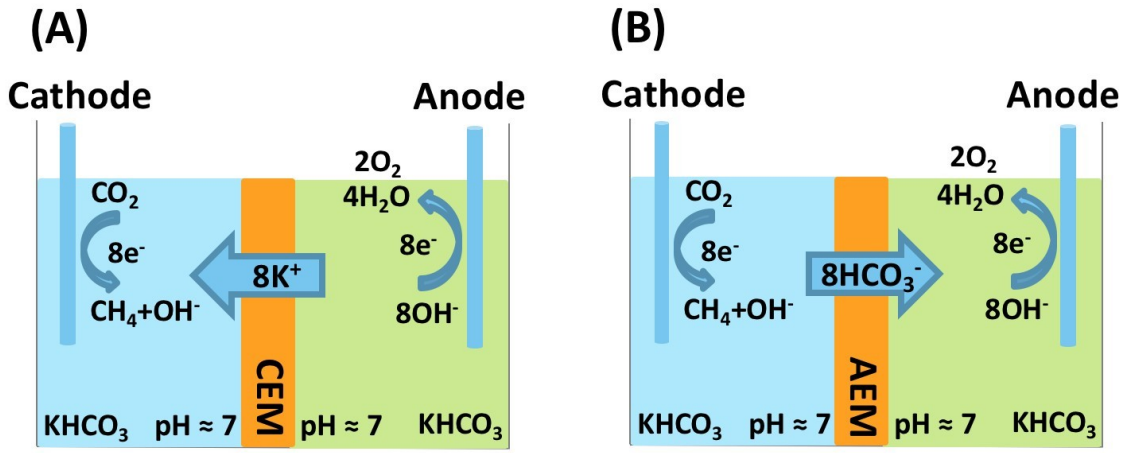

Figure 1.12: CO_2 reduction with (A) CEM and (B) AEM in CO_2 saturated $KHCO_3$ solution

One solution to overcome the pH graident problem is to circulate between the anolyte and catholyte with a pump. However, the liquid products and gas products dissolved in the catholyte will also be circulated into the anolyte, and will be oxided at the anode, resulting in overall Faradaic efficiency decrease. Besides, pump also requires additional energy input, which further decrease the energy conversion efficiency.

Bipolar membrane

BPMs are comprised of an anion exchange layer and (AEL) an cation exchange layer (CEL), as shown in Figure 1.14. CEL has negative fixed ions and only allows positive ions to go through, while AEL has positive fixed ions and only allows negative ions to go through. Therefore, at forward bias, which means CEL on the anode side and AEL on the cathode side, protons and other cations in the anolyte migrate through CEL under electric field, and are blocked at the AEL, while hydroxide ions and other anions in the catholyte migrate through AEL, and are blocked at the CEL. In this case, water or salt will be accumulated at the interface of the BPM, which damages BPM. Under reverse

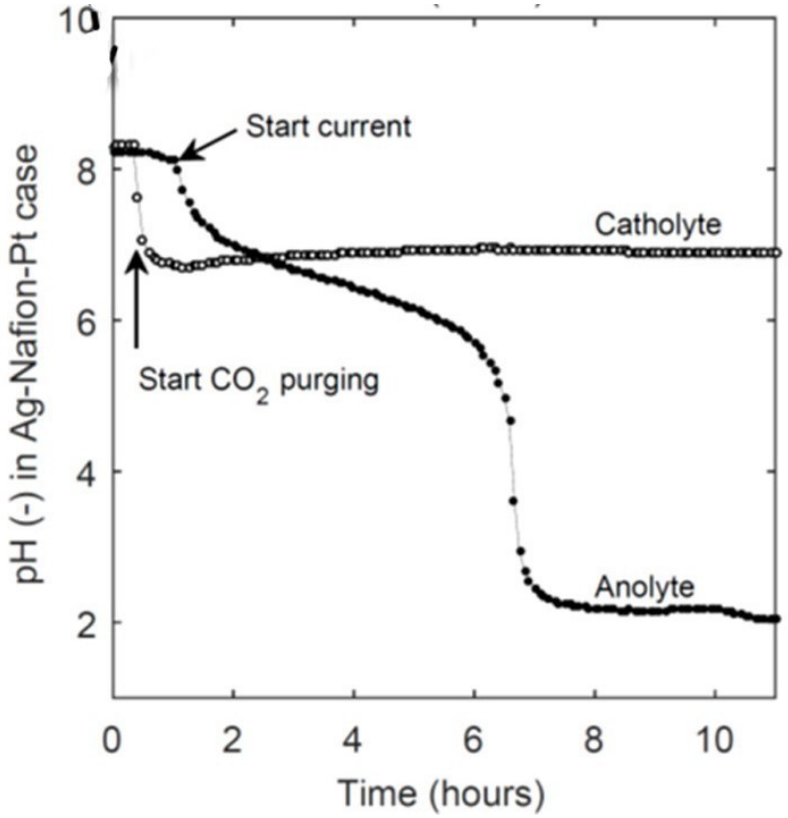

Figure 1.13: Anode and cathode pH change during CO_2 reduction to CO with Nafion. (Reprinted with permission from ref [62]. Copyright 2016 American Chemical Society)

bias as shown in Figure 1.14B, anions in the catholyte are blocked by negative fixed ions in CEL, and cations in the anolyte are blocked by positive fixed ions in the AEL. Most of the mobile ions at the junction of AEL and CEL are driven out by electric field under reverse bias, and a depletion region will form at the junction. Water dissociation to H^+ and OH^- will occur when a threshold electric field is reached at the AEL/CEL junction[63]. The dissociated H^+ and OH^- will migrate across CEL and AEL, and compensate those consumed at cathode and anode, respectively, and thus a steady-state pH gradient between catholyte and anolyte will be maintained.

A typical J-V curve of BPM is shown in Figure 1.15A. BPM is highly conductive at forward bias due to facile migration of cations and anions as shown in Figure 1.14A. Current conduction is impeded at reverse bias until a threshold voltage is reached for water dissociation at the junction. The J-V curve shape of BPM is very similar to that of p-n junction (Figure 1.15B), which forms when p-type semiconductor contacts n-type semiconductor. It is interesting to find several similarities between BPM and p-n junction as shown in Table 1.4. BPM has protons and hydroxide ions as the basic conducting

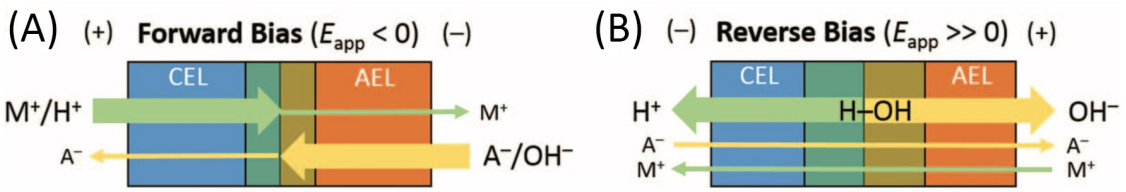

Figure 1.14: Scheme depicting directions of migration for each ion, under conditions of (A) forward bias ($E_{app} < 0$) and (B) large reverse bias ($E_{app} \gg 0$), and where a thick arrow qualitatively indicates that the transport number of that ion(s) is large. (Reprinted with no changes from ref [64], licensed under CC BY 4.0)

ions, while p-n junction has electrons and holes as conducting species; both BPM and p-n junction have mass action law, and they have similar unilateral conductivity.

	Semiconductor p-n junction	BPM
Carrier	Electrons and holes	H^+ and OH^-
Mass action law	$np = Ce^{-E_g/kT}$	$[H^+][OH^-] = 10^{-14}$ at r.t.
Current	$J = J_0(e^{eU/kT} - 1)$	Similar unilateral conductivity

Table 1.4: Comparison between semiconductor p-n junction and BPM

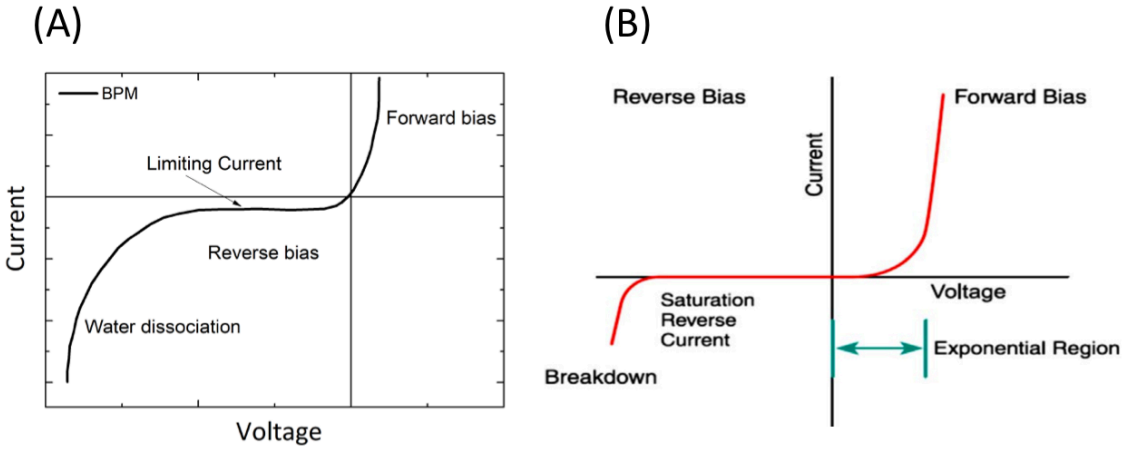

Figure 1.15: (A) Typical shape of the I-V curve of a BPM. The breakdown of the saturation regime given by the limiting current indicates the onset of the electric field enhanced water dissociation [65]. (B) Current-voltage (I-V) curve of a silicon p-n junction diode. (Reprinted with permission from ref [66]. Copyright 2016 Elsevier)

Figure 1.16 shows a scheme for a fuel generation cell. Suppose only HER occurs on the cathode. Reaction on the cathode:

$$2H^+ + 2e^- = H_2$$

Nernst potential:

$$\phi_{H^+/H_2} = \phi^{\ominus}_{H^+/H_2} + 0.059log[H^+] = \phi^{\ominus}_{H^+/H_2} - 0.059pH_2$$

Reaction on the anode:

$$O_2 + 4H^+ + 4e^- = 2H_2O$$

Nernst potential:

$$\phi_{O_2/H_2O} = \phi^{\ominus}_{O_2/H_2O} + 0.059log[H^+] = \phi^{\ominus}_{O_2/H_2O} - 0.059pH_1$$

So required overall voltage for splitting water:

$$\begin{aligned} V &= (\phi_{O_2/H_2O} + \eta_{OER}) - (\phi_{H^+/H_2} - \eta_{HER}) + V_{BPM} \\ &= \phi^{\ominus}_{O_2/H_2O} - \phi^{\ominus}_{H^+/H_2} + \eta_{OER} + \eta_{HER} + V_{BPM} - 0.059(pH_1 - pH_2) \\ &= 1.23V + \eta_{OER} + \eta_{HER} + V_{BPM} - 0.059\Delta pH \end{aligned}$$

The onset for the J-V curve of BPM is greater than ΔpH [40, 63, 67] (Figure 1.17), and water splitting at less than 1.23 V will never happen. In most of cases, more than 0.8 V is required for significant current for water dissociation under reverse bias, and therefore pH = 14 in the anolyte and pH = 0 in the catholyte will result in small voltage loss comparable to those of AEM and CEM. However, the typical pH for CO_2 reduction is 7, and pH = 7 in the catholyte and pH = 14 in the anolyte results in voltage loss of about 400 mV. But this voltage loss can be compensated by overpotential decrease at the anode. Further details will be discussed at Chapter IV.

1.5 CO_2 reduction catalyst

Methane, ethylene, methanol, acetone, etc. are typical CO_2 reduction products that require high overpotential (>500 mV) to drive reactions at > 1 mA cm^{-2} for current catalysts[69–72], while formic acid or formate and carbon monoxide require relatively small overpotentials[73–75]. Considering current light absorber maximum voltage limit, I choose formic acid as the target fuel to obtain a photoelectrochemical CO_2 reduction cell with high efficiency.

However, even for formic acid or formate as the CO_2 reduction products, photo-driven CO_2 reduction cell with solar-to-fuel conversion efficiency higher than 10% has not been made. One of the reasons is that overpotentials for CO_2 reduction to formic or formate have not been engineered to the level of HER, which requires less than 100 mV overpotential.

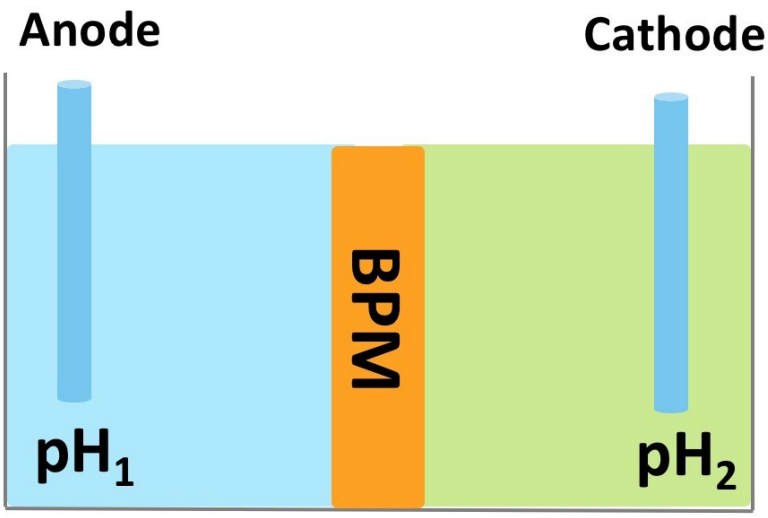

Figure 1.16: Scheme of a fuel generation cell with BPM for voltage calculation purpose.

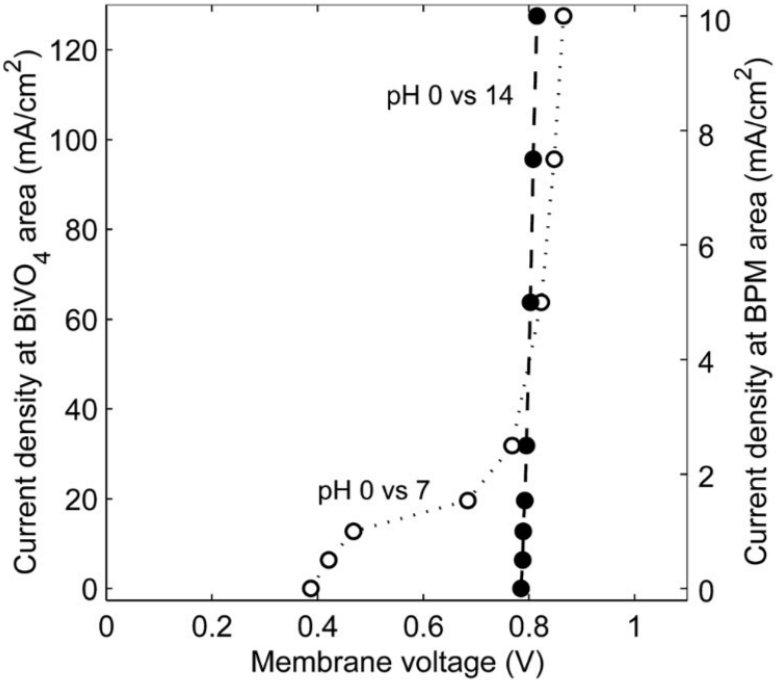

Figure 1.17: Voltage over the bipolar membrane using a pH difference of 0- 7 and 0-14 over the membrane as a function of the current density. The potentials were averaged over at least 300 s of constant current. As the bipolar membrane (BPM) area was larger than the $BiVO_4$ area, the corresponding current density for $BiVO_4$ is plotted as a secondary x-axis. No correction for ohmic losses is applied. (Reprinted with permission from ref [68]. Published by The Royal Society of Chemistry.)

Min et al. reported Pd/C as a promising CO_2 reduction catalyst to formate with low overpotential, and almost 100% Faradaic efficiency [73]. Figure 1.18A shows that at 50 mV overpotential, the CO_2 reduction current is stable at 2 mA cm^{-2}; for higher applied overpotentials, the initial current density is higher, but the corresponding current density decay rate is higher. For overpotential at 200 mV, the current density at 2 hours is even lower than that applied at 50 mV overpotential. The Faradaic efficiency maintains at around 100% for 3 hours with little decay for overpotentials from 50 mV to 150 mV, and for 200 mV overpotential, Faradaic efficiency decays to 70% after 3 hours of operation.

Even though Pd/C has relatively low overpotential and high Faradaic efficiency, the stable current density 2 mA cm^{-2} is too low for a photoelectrochemical cell with high solar-to-fuel conversion efficiency. Chapter IV will discuss improving the stable current density of Pd/C catalysts.

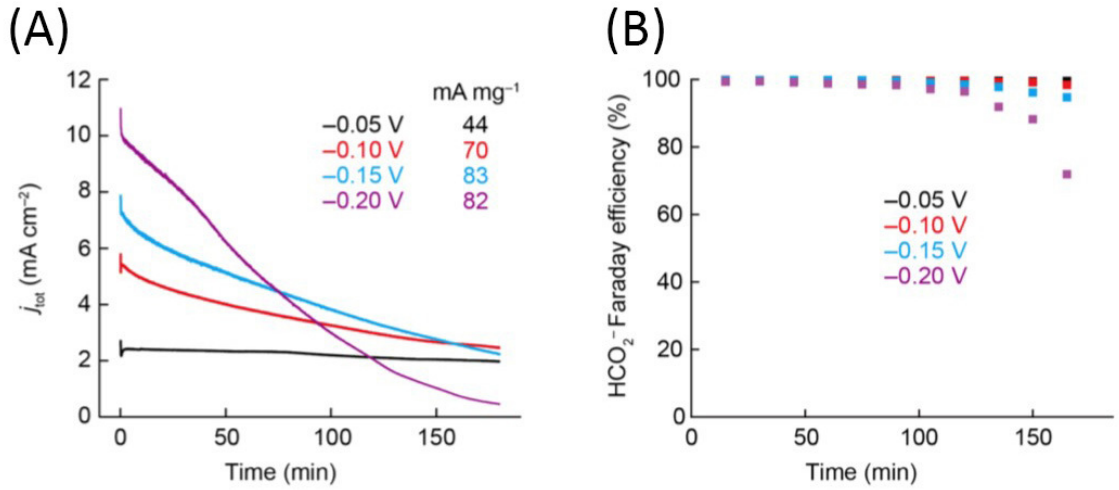

Figure 1.18: (A) Chronoamperometry data of Pd as catalyst for CO_2 reduction at different overpotentials. (B) Faradaic efficiency of Pd catalyst for CO_2 reduction at different overpotentials. (Reprinted with permission from ref [73]. Copyright 2015 American Chemical Society.)

1.6 PEC cell

Researchers have designed and fabricated solar-driven CO_2 reduction cells, but the efficiency has not reached 10% [75–79], which was mostly due to non-optimal design. Schreier et al. demonstrated a solar-driven photoelectrochemical cell in 0.5 M $NaHCO_3$(aq) with Au as CO_2 reduction catalyst and IrO_x as OER catalyst, at 6.5% solar conversion efficiency in 2015 (Figure 1.19). Arai et al. designed and demonstrated a CO_2 photoreduction to formate device in 0.1 M phosphate electrolyte, with a polymeric Ru complex as cathode and IrO_x as anode, at 4.6% solar to fuel conversion efficiency

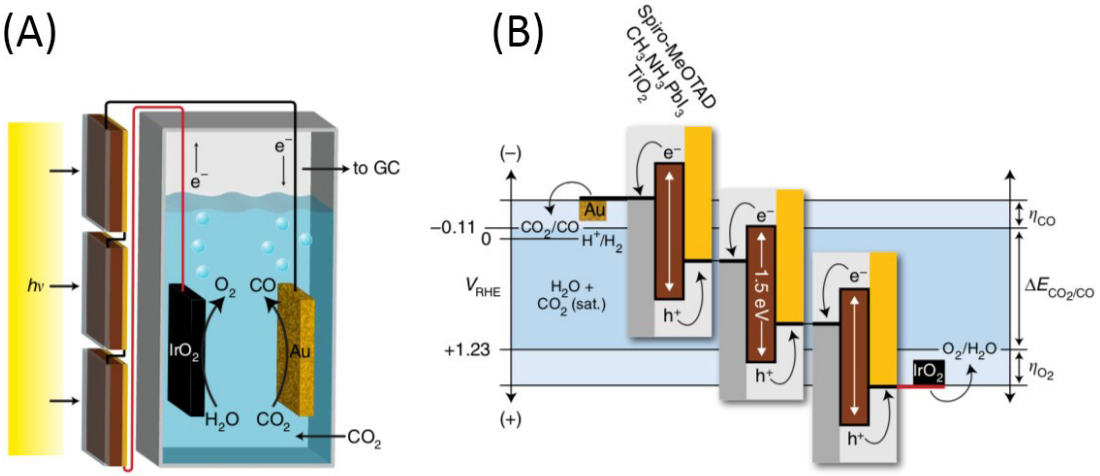

Figure 1.19: Sunlight-driven CO_2 reduction device. (a) Schematic of the device combining photovoltaics with an electrochemical cell. (b) Generalized energy diagram for converting CO_2 into CO with three perovskite solar cells. The series-connected photovoltaics produce a voltage sufficient to overcome the sum of the reaction free energy (ΔE) and the reaction overpotentials (η) at the electrodes. (From source[75], licensed under a Creative Commons Attribution 4.0 International License. It is attributed to Nature Communications.)

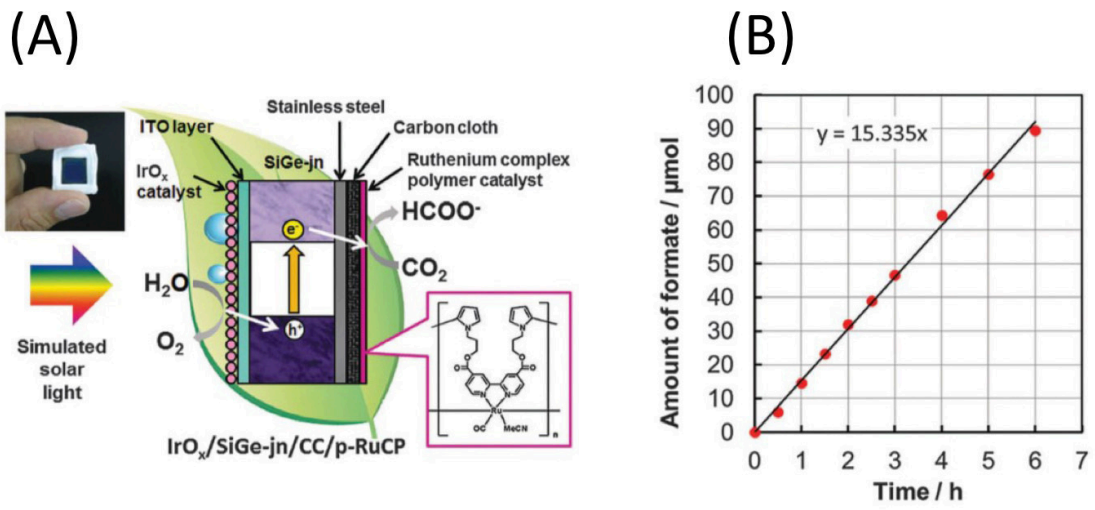

Figure 1.20: (A) Schematic illustration of the IrO_x/SiGe-jn/CC/p-RuCP monolithic tablet-shaped device for CO_2 photoreduction. (B) Time course for the generation of formate during the CO_2 photoreduction reaction using IrO_x/SiGe-jn/CC/p-RuCP under simulated solar light irradiation (1 sun, AM1.5, 0.25 cm^2). The IrO_x/SiGe-jn/CC/p-RuCP monolith was immersed in a single-compartment quartz reactor filled with CO_2-saturated phosphate buffer solution (pH 6.4). (Reprinted with permission from ref [76]. Published by The Royal Society of Chemistry.)

(Figure 1.20). Both designs used a single near-neutral pH electrolyte, which was the ideal pH range for CO_2 reduction. However, in this pH range, IrO_x as OER catalyst exhibited high overpotential (> 500 mV at 10 mA cm^{-2}), which was the main reason for the low solar-to-fuel conversion efficiency of the above two CO_2 reduction cell designs.

Almost all the OER catalysts that have been discovered up to now show state of art catalytic activity with overpotential ~250 mV - 300 mV at 10 mA cm^{-2}, but in strong alkaline solution [45, 80]. Therefore, an efficient way is required to maintain anolyte pH at 14 and catholyte at near-neutral pH, while still retaining ionic coupling between anolyte and catholyte. The solution will be discussed in detail in Chapter IV.

References

[1] *International Energy Outlook 2016*. Report DOE/EIA-0484(2016). U.S. Energy Information Administration, 2016.

[2] R. K. Pachauri and L. A. Meyer. *Climate Change 2014: Synthesis Report. Contribution of Working Groups I, II and III to the Fifth Assessment Report of the Intergovernmental Panel on Climate Change.* Report. 2015.

[3] T. R. Karl, J. M. Melillo, and T. C. Peterson. *Global Climate Change Impacts in the United States*. Report. U.S. Global Change Research Program, 2009.

[4] *Climate Change 2007: The Physical Science Basis. Contribution of Working Group I to the Fourth Assessment Report of the Intergovernmental Panel on Climate Change [Solomon, S., D. Qin, M. Manning, Z. Chen, M. Marquis, K.B. Averyt, M. Tignor, and H.L. Miller (eds.)]* Report. Cambridge University Press, 2007.

[5] J. A. Kleypas et al. "Geochemical Consequences of Increased Atmospheric Carbon Dioxide on Coral Reefs". In: *Science* 284.5411 (1999), pp. 118–120.

[6] U. Riebesell et al. "Reduced Calcification of Marine Plankton in Response to Increased Atmospheric CO2". In: *Nature* 407 (2000), p. 364.

[7] K. Caldeira and M. E. Wickett. "Anthropogenic Carbon and Ocean pH". In: *Nature* 425 (2003), p. 365.

[8] *Climate Change 2001: The Scientific Basis. Contribution of Working Group I to the Third Assesment Report of the IPCC [J. T. Houghton, Y. Ding, D. J. Griggs, M. Noguer, P. J. van der Linden, X. Dai, K. Maskell, C. A. Johnson (eds.)]* Report. Cambridge Univ. Press, 2001.

[9] C. Jiang et al. "Photoelectrochemical Devices for Solar Water Splitting - Materials and Challenges". In: *Chem. Soc. Rev.* 46.15 (2017), pp. 4645–4660.

[10] P. Murphy. *Solar Update, in Solar Heating and Cooling Programme*. Report. International Energy Agency: USA, 2009.

[11] P. Murphy. *Solar Update, in Solar Heating and Cooling Programme*. Report. International Energy Agency: USA, 2015.

[12] A. E. Curtright and J. Apt. "The Character of Power Output from Utility-scale Photovoltaic Systems". In: *Prog. Photovolt. Res. Appl.* 16.3 (2008), pp. 241–247.

[13] T. R. Cook et al. "Solar Energy Supply and Storage for the Legacy and Nonlegacy Worlds". In: *Chem. Rev.* 110.11 (2010), pp. 6474–6502.

[14] M. R. Shaner et al. "Si/TiO2 Tandem-Junction Microwire Arrays for Unassisted Solar-Driven Water Splitting". In: *J. Electrochem. Soc.* 163.5 (2016), H261–H264.

[15] M. R. Shaner et al. "Photoelectrochemistry of Core-Shell Tandem Junction n-p+-Si/n-WO3 Microwire Array Photoelectrodes". In: *Energy Environ. Sci.* 7.2 (2014), pp. 779–790.

[16] B. M. Kayes, H. A. Atwater, and N. S. Lewis. "Comparison of the Device Physics Principles of Planar and Radial p-n Junction Nanorod Solar Cells". In: *J. Appl. Phys.* 97.11 (2005), p. 114302.

[17] M. H. Lee et al. "p-Type InP Nanopillar Photocathodes for Efficient Solar-Driven Hydrogen Production". In: *Angew. Chem. Int. Ed.* 51.43 (2012), pp. 10760–10764.

[18] J. R. Maiolo et al. "High Aspect Ratio Silicon Wire Array Photoelectrochemical Cells". In: *J. Am. Chem. Soc.* 129.41 (2007), pp. 12346–12347.

[19] O. Khaselev and J. A. Turner. "A Monolithic Photovoltaic-Photoelectrochemical Device for Hydrogen Production via Water Splitting". In: *Science* 280.5362 (1998), pp. 425–427.

[20] M. D. Kelzenberg et al. "Enhanced Absorption and Carrier Collection in Si Wire Arrays for Photovoltaic Applications". In: *Nat. Mater.* 9 (2010), p. 239.

[21] H. Craighead, R. Howard, and D. Tennant. "Textured Thin-film Si Solar Selective Absorbers using Reactive Ion Etching". In: *Appl. Phys. Lett.* 37.7 (1980), pp. 653–655.

[22] K. Catchpole and M. Green. "A Conceptual Model of Light Coupling by Pillar Diffraction Gratings". In: *J. Appl. Phys.* 101.6 (2007), p. 063105.

[23] L. Hu and G. Chen. "Analysis of Optical Absorption in Silicon Nanowire Arrays for Photovoltaic Applications". In: *Nano Lett.* 7.11 (2007), pp. 3249–3252.

[24] M. Gharghi et al. "Heterojunction Silicon Microwire Solar Cells". In: *Nano Lett.* 12.12 (2012), pp. 6278–6282.

[25] A. Munoz et al. "Photoelectrochemical Conditioning of MOVPE p-InP Films for Light-induced Hydrogen Evolution: Chemical, Electronic and Optical Properties". In: *ECS J. Solid State Sci. Technol.* 2.4 (2013), Q51–Q58.

[26] E. L. Warren et al. "Hydrogen-evolution Characteristics of Ni-Mo-coated, Radial Junction, n+p-silicon Microwire Array Photocathodes". In: *Energy Environ. Sci.* 5.11 (2012), pp. 9653–9661.

[27] J. M. Spurgeon et al. “Electrical Conductivity, Ionic Conductivity, Optical Absorption, and Gas Separation Properties of Ionically Conductive Polymer Membranes Embedded with Si Microwire Arrays”. In: *Energy Environ. Sci.* 4.5 (2011), pp. 1772–1780.

[28] M. G. Walter et al. “Solar Water Splitting Cells”. In: *Chem. Rev.* 110.11 (2010), pp. 6446–6473.

[29] N. S. Lewis and D. G. Nocera. “Powering the Planet: Chemical Challenges in Solar Energy Utilization”. In: *Proc. Natl. Acad. Sci. U.S.A.* 103.43 (2006), pp. 15729–15735.

[30] K. Sun et al. “Stable Solar-Driven Oxidation of Water by Semiconducting Photoanodes Protected by Transparent Catalytic Nickel Oxide Films”. In: *Proc. Natl. Acad. Sci. U.S.A.* 112 (2015), pp. 3612–3617.

[31] K. Sun et al. “Stable Solar-Driven Water Oxidation to O2(g) by Ni-oxide Coated Silicon Photoanodes”. In: *J. Phys. Chem. Lett.* 6 (2015), pp. 592–598.

[32] X. Li, F. C. Walsh, and D. Pletcher. “Nickel Based Electrocatalysts for Oxygen Evolution in High Current Density, Alkaline Water Electrolysers”. In: *Phys. Chem. Chem. Phys.* 13.3 (2011), pp. 1162–1167.

[33] D. A. Corrigan. “The Catalysis of the Oxygen Evolution Reaction by Iron Impurities in Thin Film Nickel Oxide Electrodes”. In: *J. Electrochem. Soc.* 134.2 (1987), pp. 377–384.

[34] M. W. Louie and A. T. Bell. “An Investigation of Thin-film Ni-Fe Oxide Catalysts for the Electrochemical Evolution of Oxygen”. In: *J. Am. Chem. Soc.* 135.33 (2013), pp. 12329–12337.

[35] L. Trotochaud et al. “Nickel-Iron Oxyhydroxide Oxygen-Evolution Electrocatalysts: The Role of Intentional and Incidental Iron Incorporation”. In: *J. Am. Chem. Soc.* 136.18 (2014), pp. 6744–6753.

[36] A. M. Smith et al. “Contributions to Activity Enhancement via Fe Incorporation in Ni-(oxy) Hydroxide/borate Catalysts for Near-neutral pH Oxygen Evolution”. In: *Chem. Commun.* 51.25 (2015), pp. 5261–5263.

[37] K. Sun et al. “Sputtered NiOx Films for Stabilization of p+n-InP Photoanodes for Solar-Driven Water Oxidation”. In: *Adv. Energy Mater.* (2015), p. 1402276.

[38] X. Zhou et al. “Interface Engineering of the Photoelectrochemical Performance of Ni-oxide-coated n-Si Photoanodes by Atomic-Layer Deposition of Ultrathin Films of Cobalt Oxide”. In: *Energy Environ. Sci.* 8.9 (2015), pp. 2644–2649.

[39] I. Roger, M. A. Shipman, and M. D. Symes. “Earth-abundant Catalysts for Electrochemical and Photoelectrochemical Water Splitting”. In: *Nat. Rev. Chem.* 1 (2017), p. 0003.

[40] K. Sun et al. “A Stabilized, Intrinsically Safe, 10% Efficient, Solar-Driven Water-Splitting Cell Incorporating Earth-Abundant Electrocatalysts with Steady-State pH Gradients and Product Separation Enabled by a Bipolar Membrane”. In: *Adv. Energy Mater.* 6.13 (2016), p. 1600379.

[41] M. D. Merrill and R. C. Dougherty. “Metal Oxide Catalysts for the Evolution of O2 from H2O”. In: *J. Phys. Chem. C* 112.10 (2008), pp. 3655–3666.

[42] X. Zhou et al. “570 mV Photovoltage, Stabilized n-Si/CoOx Heterojunction Photoanodes Fabricated using Atomic Layer Deposition”. In: *Energy Environ. Sci.* 9.3 (2016), pp. 892–897.

[43] Y. Surendranath, M. Dincă, and D. G. Nocera. “Electrolyte-Dependent Electrosynthesis and Activity of Cobalt-Based Water Oxidation Catalysts”. In: *J. Am. Chem. Soc.* 131.7 (2009), pp. 2615–2620.

[44] N. Jiang et al. “Electrodeposited Cobalt-Phosphorous-Derived Films as Competent Bifunctional Catalysts for Overall Water Splitting”. In: *Angew. Chem. Int. Ed.* 127.21 (2015), pp. 6349–6352.

[45] B. Zhang et al. “Homogeneously Dispersed Multimetal Oxygen-evolving Catalysts”. In: *Science* 352.6283 (2016), pp. 333–337.

[46] F. Zhou et al. “Improvement of Catalytic Water Oxidation on MnOx Films by Heat Treatment”. In: *ChemSusChem* 6.4 (2013), pp. 643–651.

[47] D. Li et al. “Efficient Water Oxidation using CoMnP Nanoparticles”. In: *J. Am. Chem. Soc.* 138.12 (2016), pp. 4006–4009.

[48] T. N. Lambert et al. “Electrodeposited NixCo3-xO4 Nanostructured Films as Bifunctional Oxygen Electrocatalysts”. In: *Chem. Commun.* 51.46 (2015), pp. 9511–9514.

[49] J. Tian et al. “Self-supported NiMoHollow Nanorod Array: an Efficient 3D Bifunctional Catalytic Electrode for Overall Water Splitting”. In: *J. Mater. Chem. A* 3.40 (2015), pp. 20056–20059.

[50] I. A. Moreno-Hernandez et al. “Crystalline Nickel Manganese Antimonate as a Stable Water-Oxidation Catalyst in Aqueous 1.0 M H2SO4”. In: *Energy Environ. Sci.* 10.10 (2017), pp. 2103–2108.

[51] N. Danilovic et al. “Activity-stability Trends for the Oxygen Evolution Reaction on Monometallic Oxides in Acidic Environments”. In: *J. Phys. Chem. Lett.* 5.14 (2014), pp. 2474–2478.

[52] L. C. Seitz et al. “A Highly Active and Stable IrOx/SrIrO3 Catalyst for the Oxygen Evolution Reaction”. In: *Science* 353.6303 (2016), pp. 1011–1014.

[53] M. X. Tan et al. “Principles and Applications of Semiconductor Photoelectrochemistry”. In: *Prog. Inorg. Chem.* 41 (1994), pp. 21–144.

[54] M. X. Tan et al. “Behavior of Si Photoelectrodes under High Level Injection Conditions. 1. Steady-state Current-voltage Properties and Quasi-Fermi Level Positions under Illumination”. In: *J. Phys. Chem. B* 101.15 (1997), pp. 2830–2839.

[55] C. Kenyon et al. “Behavior of Si Photoelectrodes under High Level Injection Conditions. 3. Transient and Steady-state Measurements of the Quasi-Fermi Levels at Si/CH3OH Contacts”. In: *J. Phys. Chem. B* 101.15 (1997), pp. 2850–2860.

[56] M. X. Tan, C. Kenyon, and N. S. Lewis. “Experimental Measurement of Quasi-Fermi Levels at an Illuminated Semiconductor/Liquid Contact”. In: *J. Phys. Chem.* 98.19 (1994), pp. 4959–4962.

[57] O. Krüger et al. “Behavior of Si Photoelectrodes under High Level Injection Conditions. 2. Experimental Measurements and Digital Simulations of the Behavior of Quasi-Fermi Levels under Illumination and Applied Bias”. In: *J. Phys. Chem. B* 101.15 (1997), pp. 2840–2849.

[58] Y. W. Chen et al. “Atomic Layer-Deposited Tunnel Oxide Stabilizes Silicon Photoanodes for Water Oxidation”. In: *Nat. Mater.* 10.7 (2011), pp. 539–44.

[59] M. J. Kenney et al. “High-Performance Silicon Photoanodes Passivated with Ultrathin Nickel Films for Water Oxidation”. In: *Science* 342.6160 (2013), pp. 836–40.

[60] S. Hu et al. “Amorphous TiO(2) Coatings Stabilize Si, GaAs, and GaP Photoanodes for Efficient Water Oxidation”. In: *Science* 344.6187 (2014), pp. 1005–9.

[61] L. Ji et al. “Localized Dielectric Breakdown and Antireflection Coating in Metal-oxide-semiconductor Photoelectrodes”. In: *Nat. Mater.* 16.1 (2017), p. 127.

[62] D. A. Vermaas and W. A. Smith. “Synergistic Electrochemical CO2 Reduction and Water Oxidation with a Bipolar Membrane”. In: *ACS Energy Lett.* 1.6 (2016), pp. 1143–1148.

[63] N. M. Vargas-Barbosa et al. “Assessing the Utility of Bipolar Membranes for use in Photoelectrochemical Water-Splitting Cells”. In: *ChemSusChem* 7.11 (2014), pp. 3017–3020.

[64] R. S. Reiter, W. White, and S. Ardo. “Communication-Electrochemical Characterization of Commercial Bipolar Membranes under Electrolyte Conditions Relevant to Solar Fuels Technologies”. In: *J. Electrochem. Soc.* 163.4 (2016), H3132–H3134.

[65] S. Mafé and P. Ramírez. “Electrochemical Characterization of Polymer Ion-exchange Bipolar Membranes”. In: *Acta Polym.* 48.7 (1997), pp. 234–250.

[66] M. A. M. Al-Alwani et al. “Dye-sensitised solar cells: Development, structure, operation principles, electron kinetics, characterisation, synthesis materials and natural photosensitisers”. In: *Renewable and Sustainable Energy Reviews* 65 (2016), pp. 183–213.

[67] J. Luo et al. “Bipolar Membrane-Assisted Solar Water Splitting in Optimal pH”. In: *Adv. Energy Mater.* 6.13 (2016), p. 1600100.

[68] D. A. Vermaas, M. Sassenburg, and W. A. Smith. “Photo-assisted Water Splitting with Bipolar Membrane Induced pH Gradients for Practical Solar Fuel Devices”. In: *J. Mater. Chem. A* 3.38 (2015), pp. 19556–19562.

[69] F. S. Roberts, K. P. Kuhl, and A. Nilsson. “High Selectivity for Ethylene from Carbon Dioxide Reduction over Copper Nanocube Electrocatalysts”. In: *Angew. Chem. Int. Ed.* 127.17 (2015), pp. 5268–5271.

[70] D. A. Torelli et al. “Nickel-Gallium-Catalyzed Electrochemical Reduction of CO2 to Highly Reduced Products at Low Overpotentials”. In: *ACS Catal.* 6.3 (2016), pp. 2100–2104.

[71] H. Yano et al. “Selective Electrochemical Reduction of CO2 to Ethylene at a Three-phase Interface on Copper (I) Halide-confined Cu-mesh Electrodes in Acidic Solutions of Potassium Halides”. In: *J. Electroanal. Chem.* 565.2 (2004), pp. 287–293.

[72] D. Ren et al. “Selective Electrochemical Reduction of Carbon Dioxide to Ethylene and Ethanol on Copper (I) Oxide Catalysts”. In: *ACS Catal.* 5.5 (2015), pp. 2814–2821.

[73] X. Min and M. W. Kanan. “Pd-Catalyzed Electrohydrogenation of Carbon Dioxide to Formate: High Mass Activity at Low Overpotential and Identification of the Deactivation Pathway”. In: *J. Am. Chem. Soc.* 137.14 (2015), pp. 4701–4708.

[74] R. Kortlever et al. “Electrochemical CO2 Reduction to Formic Acid at Low Overpotential and with High Faradaic Efficiency on Carbon-Supported Bimetallic Pd–Pt Nanoparticles”. In: *ACS Catal.* 5.7 (2015), pp. 3916–3923.

[75] M. Schreier et al. “Efficient Photosynthesis of Carbon Monoxide from CO2 using Perovskite Photovoltaics”. In: *Nat. Commun.* 6 (2015), p. 7326.

[76] T. Arai, S. Sato, and T. Morikawa. “A Monolithic Device for CO2 Photoreduction to Generate Liquid Organic Substances in a Single-compartment Reactor”. In: *Energy Environ. Sci.* 8.7 (2015), pp. 1998–2002.

[77] T. Arai et al. “Solar CO2 Reduction Using H2O by a Semiconductor/metal-complex Hybrid Photocatalyst: Enhanced Efficiency and Demonstration of a Wireless System Using SrTiO3 Photoanodes”. In: *Energy Environ. Sci.* 6.4 (2013), p. 1274.

[78] H. S. Jeon et al. “A Monolithic and Standalone Solar-fuel Device having Comparable Efficiency to Photosynthesis in Nature”. In: *J. Mater. Chem. A* 3.11 (2015), pp. 5835–5842.

[79] S. Sato et al. “Selective CO2 Conversion to Formate Conjugated with H2O Oxidation Utilizing Semiconductor/complex Hybrid Photocatalysts”. In: *J. Am. Chem. Soc.* 133.39 (2011), pp. 15240–3.

[80] C. C. L. McCrory et al. “Benchmarking Heterogeneous Electrocatalysts for the Oxygen Evolution Reaction”. In: *J. Am. Chem. Soc.* 135.45 (2013), pp. 16977–16987.

Chapter 2

INTERFACE ENGINEERING OF THE PHOTOELECTROCHEMICAL PERFORMANCE OF NI-OXIDE-COATED N-SI PHOTOANODES BY ATOMIC-LAYER DEPOSITION OF ULTRATHIN FILMS OF COBALT OXIDE

[1]Thick (> 50 nm) multifunctional NiO_x coatings enable the use of small-band-gap non-oxide semiconductors as photoanodes in fully integrated, intrinsically safe, and efficient photoelectrosynthetic water-splitting systems. The equivalent open-circuit voltage generated by such protected n-type semiconductor heterojunction structures is, however, significantly lower than that obtained from homogeneous np^+ buried junctions. In this chapter, we demonstrate that deposition of a thin cobalt oxide film onto n-Si substrates prior to deposition of a thick multifunctional NiO_x coating significantly improves the performance of such protected n-type Si photoanodes. The approach provides a route to formation of stabilized, high-performance Si photoanodes without requiring the formation of buried p-n homojunctions, potentially simplifying the photoelectrode processing and thus reducing the cost of monolithically integrated solar-driven water-splitting devices.

2.1 Introduction

Although $SrTiO_3$, $KTaO_3$, and TaON have been used in stable wired or "wireless" configurations to effect direct solar-driven water splitting [1], all known smaller-band-gap, non-oxide semiconductors require protection from corrosion for use in stable, intrinsically safe, efficient photoelectrosynthetic or photovoltaic-(PV) biased electrosynthetic water-splitting cells [2, 3]. When the protective layer fully prevents contact between the electrolyte and the semiconductor, effective charge separation in the light absorber requires a mechanism for establishing a significant electric field at the semiconductor surface. Semiconductor/metal Schottky barriers [4, 5]; p-n homojunctions on planar electrodes [6–10], spherical electrodes [11], and radial emitters on microwires [12]; metal-insulator-semiconductor contacts [13, 14]; in situ formation of emitter layers by carrier inversion [15–18]; heterojunctions [19–21]; and mixed barrier-height semiconductor/metal/oxide/liquid systems [22] have all been investigated in either wired or "wireless" photoelectrosynthetic or PV-biased electrosynthetic systems. Generally tandem structures

[1]This chapter is based on results in: X. Zhou, R. Liu, K. Sun, D. Friedrich, M. T. McDowell, F. Yang, S. T. Omelchenko, F. H. Saadi, A. C. Nielander, S. Yalamanchili, K. M. Papadantonakis, B. S. Brunschwig and N. S. Lewis, Energy Environ. Sci., 2015, 8, 2644 - Published by The Royal Society of Chemistry.

or triple junctions are required to provide the open-circuit voltage (V_{oc}) necessary to effect unassisted water splitting in either a wired or monolithically integrated ("wireless") configuration [23–28], with noble metals or earth-abundant electrocatalysts [28] used in the full water-splitting system. The electrode surfaces require both protection or stabilization against corrosion and the deposition of an effective catalyst for use in either the photoelectrochemical anodic (water oxidation) or cathodic (fuel formation) half reactions.

Ni-oxide films formed by reactive sputtering have recently been shown to form protecting layers on a variety of semiconductor surfaces, including Si, InP, amorphous hydrogenated Si (a-Si:H), and CdTe [29–31]. The NiO_x is optically transparent in the visible region and has an index of refraction that makes the NiO_x a near-optimal anti-reflective coating on a variety of semiconductor surfaces. Furthermore, NiO_x is chemically stable at high pH, and upon activation forms a surface layer that is catalytic for the oxygen-evolution reaction (OER), with overpotentials of $\sim$ 330 mV at 10 mA cm^{-2} in 1.0 M KOH(aq) [29]. NiO_x coatings on semiconductors that form passive films under photoanodic conditions have produced high photocurrent densities for solar-driven OER from water for months of continuous operation under simulated 1 Sun conditions [29–31].

However, due to nonoptimal energetics at the interface between the NiO_x and the semiconductor, formation of a direct heterojunction contact between the n-type absorber and the p-type NiO_x layer yields relatively low V_{oc} values [29–31]. Significantly higher V_{oc} values for such stabilized systems have been obtained from electrodes formed by deposition of a NiO_x coating onto a buried p-n homojunction [29, 30]. For example, freshly etched n-Si and np^+-Si photoanodes protected by a multifunctional layer of NiO_x yielded equivalent open-circuit voltages of 180 mV and 510 mV, respectively [29]. The formation of heterojunctions between n-Si coated with a layer of SiO_x (either native or introduced by processing steps) and thin (< 20 nm) films of Ni [22], MnOx [32], and TiO_2 [33] offers some protection against corrosion to n-Si photoanodes, and in some cases yields photoanodes exhibiting $V_{oc} \geq 500$ mV. The ideal regenerative solar-to-O2 conversion efficiency [34] of these heterogeneous systems is relatively low compared to values exhibited by NiO_x protected np^+-Si photoanodes [29, 35]. The solar-to-fuel conversion efficiency is thus limited when such protected photoanodes are used in a tandem photochemical diode design [3, 36].

For technologically well-developed semiconductors such as Si and the III-V materials, p-n homojunctions can be formed to provide V_{oc} values that can approach the Shockley diode bulk recombination/diffusion limit [2, 3]. Many semiconductors of interest for use in photoelectrochemical cells, however, cannot be doped to form high-quality homojunctions.

Moreover, the doping/diffusion process generally requires high temperatures, and adds complexity to the formation of a functional photoelectrode, relative to electrodeposition or spray pyrolysis of the active semiconductor layer onto a suitable substrate. For small grain-size polycrystalline films, dopants often migrate preferentially along grain boundaries, especially during the drive-in step, producing majority-carrier shunts that degrade the performance of the resulting photoelectrode [37]. Hence methods which allow large V_{oc} values and high efficiencies to be obtained from protected semiconductor photoelectrodes in contact with aqueous electrolytes, but which do not require the formation of diffused homojunctions, are desirable.

Cobalt oxide has a relatively high work function, and is supposed to be stable in strong alkaline solution. We demonstrate herein that introduction of a thin, compositionally controlled, interfacial cobalt oxide layer between the n-Si absorber and the protective, multifunctional NiO_x film can yield V_{oc} values close to the Shockley diode limit for moderately doped n-Si(100) photoelectrodes. The performance and stability of such materials used as PV-biased electrosynthetic systems for water oxidation are comparable to that observed from diffused Si p-n homojunctions protected by the NiO_x overlayer. Such "interfacial engineering" of the junction energetics demonstrates that protection schemes can be implemented to yield high-performance photoelectrodes without the complexity of the requirement to form a diffused homojunction, while concurrently obtaining efficient separation of photogenerated charges in the semiconducting photoelectrode.

2.2 Experimental

To form the desired interfacial layers, n-Si (100) (0.1–1 ohm-cm resistivity, 525 μm thick) was first etched in an RCA SC-2 etchant solution for 10 min at 75 °C to produce a thin SiO_x layer on the Si surface (n-Si/$SiO_{x,RCA}$). Thin films of CoO_x were then deposited by atomic-layer deposition (ALD) onto the Si/$SiO_{x,RCA}$. After ALD growth of the CoO_x layer, NiO_x was deposited by reactive radio-frequency sputtering onto the CoO_x, with the Si substrates maintained at 300 °C (n-Si/$SiO_{x,RCA}$/CoO_x/NiO_x). Sixty ALD cycles of CoO_x deposition were found to optimize the photocurrent-onset potentials relative to the formal potential, $E^{\circ\prime}(Fe(CN)_6^{3-/4-})$ for the n-Si/$SiO_{x,RCA}$/CoO_x/NiO_x devices (Figure 2.1) and were thus used in the fabrication of all of the devices described herein. For detailed experimental information, please see Appendix B.

2.3 Results and Discussion

Figure 2.2A shows a high-resolution transmission-electron microscopy (TEM) image of the n-Si/$SiO_{x,RCA}$/CoO_x/NiO_x interface. An amorphous ~ 2 nm thick layer of SiO_x

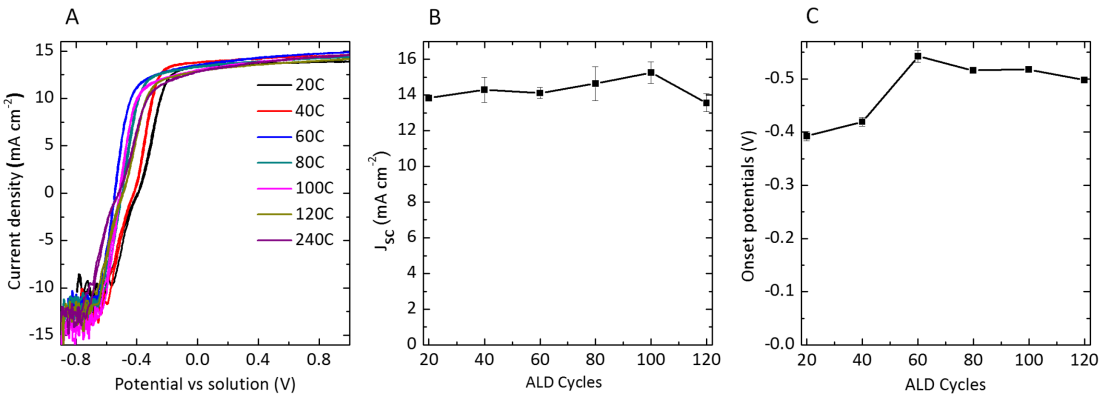

Figure 2.1: (A) J-E behavior of n-Si/$SiO_{x,RCA}$/CoO_x/NiO_x photoanodes as a function of the thickness of the CoO_x interfacial layer, ranging from 20 ALD cycles (20C) to 240 ALD cycles (240C), under 0.4-Sun simulated solar illumination in a solution of 0.35 M $K_4Fe(CN)_6$, 0.05 M $K_3Fe(CN)_6$ and 1.0 M KCl (aq). (B, C) Dependence of the photoelectrochemical behavior of n-Si/$SiO_{x,RCA}$/CoO_x/NiO_x photoanodes under 40 mW cm^{-2} of simulated solar illumination and in contact with 0.35 M $K_4Fe(CN)_6$, 0.05 M $K_3Fe(CN)_6$ and 1.0 M KCl(aq). (B) Light-limited current density and (C) Photocurrent-onset potentials relative to $E^{\circ'}(Fe(CN)_6^{3-/4-})$ (Onset potentials for short) versus the CoO_x layer thickness as indicated by the number of ALD cycles used to deposit the coating.

was observed on the surface of the crystalline Si, with a 2–3 nm thick layer of CoO_x between the SiO_x and NiO_x layers. The low difference in contrast between the CoO_x and NiO_x layers is due to the similar densities of the metal oxide films. Figure 2.2B shows the results of a scanning transmission-electron microscopy (STEM) energy-dispersive spectroscopy (EDS) line scan across the n-Si/$SiO_{x,RCA}$/CoO_x/NiO_x interface. A Co X-ray signal was evident at the interface between the Si and Ni signals, and confirmed the presence of the thin CoO_x layer, which was also detected using X-ray photoelectron spectroscopy (XPS) (Figure 2.3A, B). Peak-fitting of the XP spectra in the Co $2p_{3/2}$ region showed the co-presence of Co(II) and Co(III), possibly in the forms of CoO, Co_2O_3, Co_3O_4, and $Co(OH)_2$/CoOOH [38, 39]. Grazing incidence X-ray diffractometry (GIXRD) showed that the film was polycrystalline with peak positions consistent with Co_3O_4, and that annealing the film under the deposition conditions did not result in any significant changes to the structure, crystallinity, or preferred orientation of the film (Figure 2.3C). The root-mean-squared (rms) surface roughness of the n-Si/$SiO_{x,RCA}$ and n-Si/$SiO_{x,RCA}$/Co_3O_4 surfaces was 0.403 nm and 0.453 nm, respectively (Figure 2.4). A low-magnification high-angle annular dark-field (HAADF) STEM image of a cross-section of the n-Si/$SiO_{x,RCA}$/Co_3O_4/NiO_x film (Figure 2.2C) showed that the NiO_x film consisted of short columns with an average diameter of ~20 nm and an average height of

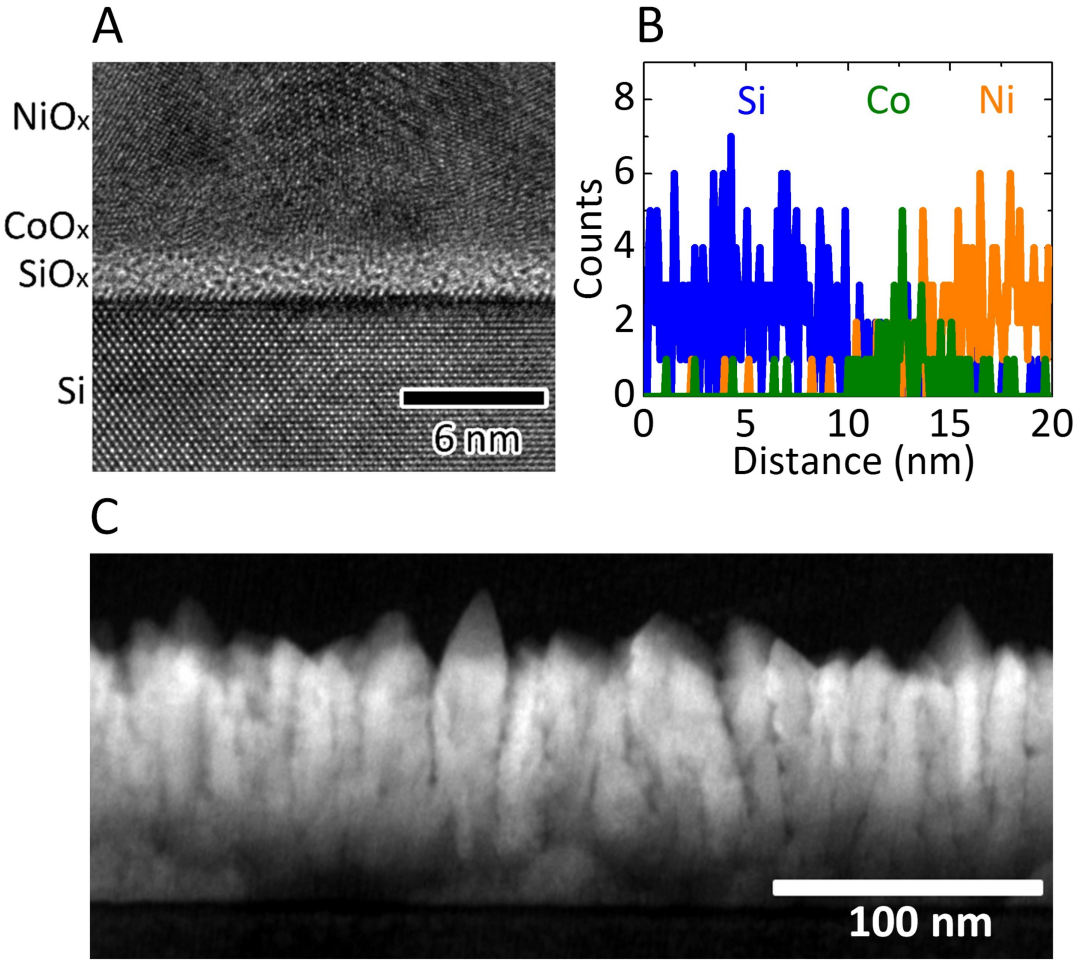

Figure 2.2: (A) High-resolution transmission-electron microscope (TEM) image of a cross-section of an n-Si/$SiO_{x,RCA}$/CoO_x/NiO_x sample. The lighter region at the surface of the Si is SiO_x. The CoO_x layer is incorporated into the highly polycrystalline region between the SiO_x and the larger NiO_x grains at the top of the image. (B) Energy-dispersive spectroscopy (EDS) line-scan across the Si/$SiO_{x,RCA}$/CoO_x/NiO_x interface in which the K_α X-rays from Si, Co, and Ni are displayed as a function of distance. (C) Low-magnification HAADF-STEM cross-sectional image of an n-Si/$SiO_{x,RCA}$/CoO_x/NiO_x electrode. The bright film is the polycrystalline NiO_x layer, which grew in a columnar fashion with vertical grain boundaries. The Si wafer is the dark layer at the bottom of the image.

~102 nm, with a mean density of ~2500 columns μm^{-2}.

Figure 2.5 shows the current-density versus potential (J-E) behavior of n-Si/$SiO_{x,RCA}$/NiO_x photoanodes with and without an interfacial layer of Co_3O_4, in contact with 1.0 M KOH(aq), illuminated by 1 sun of simulated solar illumination, and without correction for resistance losses in the system. The photocurrent-onset potentials were -239 ± 3 mV and

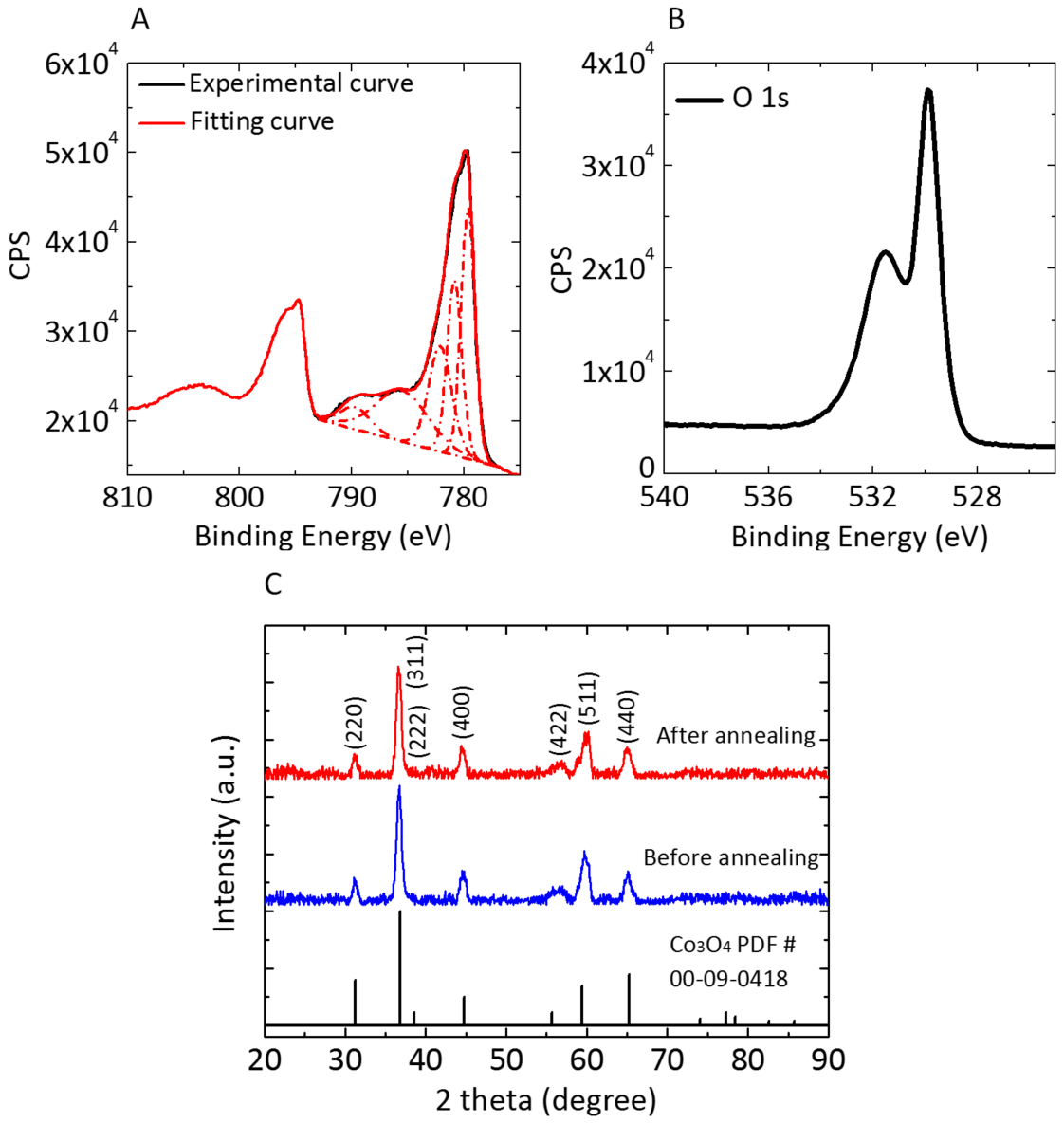

Figure 2.3: (A, B) X-Ray photoelectron spectra (XPS) for an n-Si/$SiO_{x,RCA}$/CoO_x photoelectrode. The binding energies used for fitting of the Co $2p_{3/2}$ peaks were 779.6 eV, 780.8 eV, 782.2 eV, 785.5 eV, 789.7 eV. (C) Grazing incidence X-ray diffraction (GIXRD) pattern for a CoO_x film (1000 ALD cycles) on an n-Si/$SiO_{x,RCA}$ substrate before and after annealing in an AJA high-vacuum magnetron sputtering chamber at 300 $^{\circ}C$ under the sputtering gas environment.

-74 ± 12 mV relative to the formal potential for water oxidation ($E^{o'}(O_2/H_2O) = 1.23$ V versus a reversible hydrogen electrode, RHE, at pH = 14) for the n-Si/$SiO_{x,RCA}$/Co_3O_4/NiO_x and n-Si/$SiO_{x,RCA}$/NiO_x photoanodes, respectively, with three electrodes of each type measured. Thus, the presence of the interfacial Co_3O_4 layer between the n-Si/$SiO_{x,RCA}$

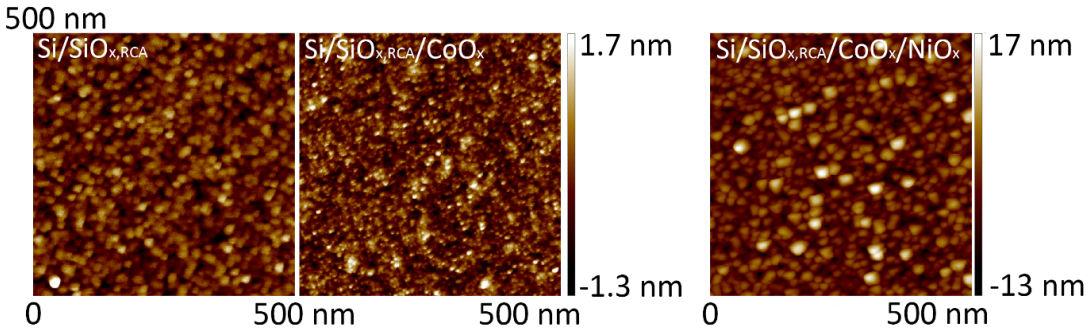

Figure 2.4: AFM images showing the surface morphology of n-Si/$SiO_{x,RCA}$, n-Si/ $SiO_{x,RCA}$/ Co_3O_4, and n-Si/$SiO_{x,RCA}$/Co_3O_4/NiO_x, respectively.

and the NiO_x resulted in a -165 mV shift in the photocurrent-onset potential of the n-Si/$SiO_{x,RCA}$/Co_3O_4/NiO_x photoanode relative to the n-Si/$SiO_{x,RCA}$/NiO_x electrode that did not contain the Co_3O_4 layer. The J-E behavior for the n-Si/$SiO_{x,RCA}$/Co_3O_4/NiO_x electrode exhibited a larger slope ($\sim$ 140.0 mA cm^{-2} V-1 measured between 1.00 V and 1.15 V versus RHE) than the J-E behavior of the n-Si/$SiO_{x,RCA}$/NiO_x electrode (slope $\sim$100 mA cm^{-2} V-1 measured between 1.25 V and 1.45 V vs RHE). The increased slope is attributable to a reduced series resistance and/or reduced surface recombination velocity, which could indicate that the Co_3O_4 layer prevents further oxidation of the Si and/or damage to the existing $SiO_{x,RCA}$ junction layer during sputter-deposition of the NiO_x film. The photocurrent density for the n-Si/$SiO_{x,RCA}$/Co_3O_4/NiO_x photoanode structure was 27.7 ± 0.4 mA cm^{-2} at $E^{o'}(O_2/H_2O)$, and the solar-to-O_2(g) ideal regenerative-cell conversion efficiency[34] (η_{IRC}, see Appendix A.1) was 2.1 ± 0.2 %, while for the n-Si/$SiO_{x,RCA}$/NiO_x photoanode structure the photocurrent density was 6.3 ± 1.5 mA cm^{-2} at $E^{o'}(O_2/H_2O)$, and the η_{IRC} for solar-to-O_2(g) was 0.11 ± 0.04 %, each with three electrodes of each type tested. A load-line analysis based on an equivalent-circuit model consisting of a photodiode connected in series with a dark electrolysis cell indicated that obtaining a shift in the J-E behavior equivalent to that observed for the n-Si/$SiO_{x,RCA}$/Co_3O_4/NiO_x photoanode relative to the p^+-Si/NiO_x anode would require a 12.3 ± 0.3% efficient photodiode with a V_{oc} of 565 ± 3 mV and a short-circuit photocurrent density (Jsc) of 32.5 ± 0.3 mA cm^{-2} [34]. The performance of the n-Si/$SiO_{x,RCA}$/Co_3O_4/NiO_x photoanode was modestly better than that reported for a homogeneous buried-junction p^+n-Si electrode that had been freshly etched and directly sputtered with NiO_x (photocurrent-onset potential of -180 ± 20 mV relative to $E^{o'}(O_2/H_2O)$ and a photocurrent density of 29 ± 1.8 mA cm^{-2} at $E^{o'}(O_2/H_2O)$), and was significantly improved relative to the performance of an HF-etched n-Si electrode that had

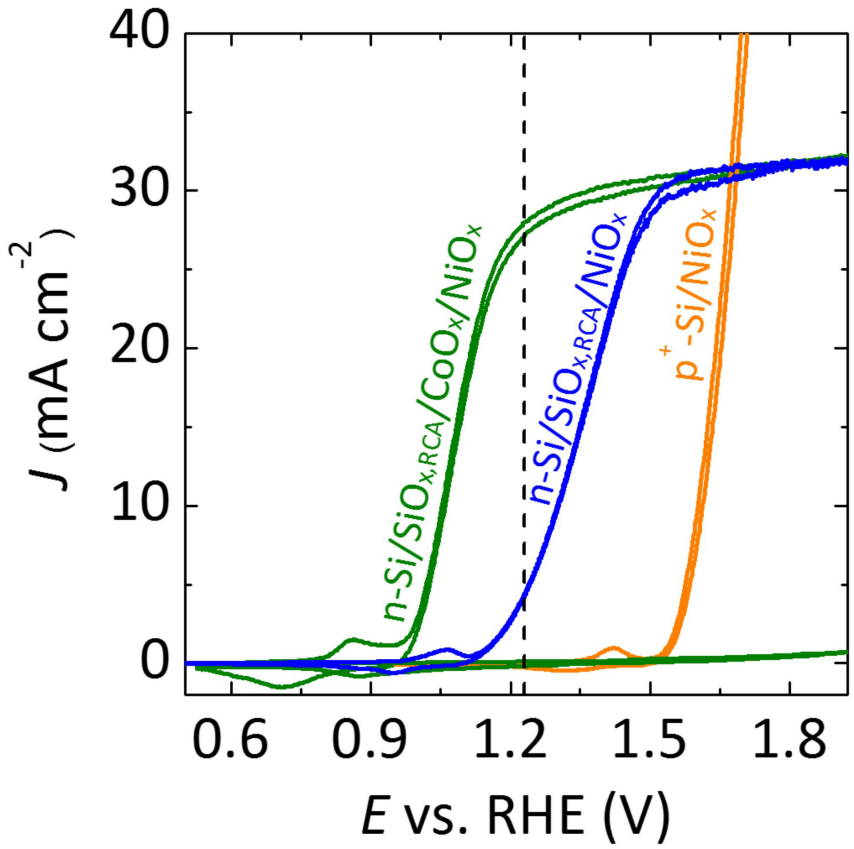

Figure 2.5: Representative current-density versus potential (J-E) behavior of n-Si/ $SiO_{x,RCA}$/ Co_3O_4/NiO_x and n-Si/$SiO_{x,RCA}$/NiO_x photoanodes in contact with 1.0 M KOH (aq) in the dark (The nonzero electrode potential vs $E^{o'}(O_2/H_2O)$ of n-Si/$SiO_{x,RCA}$/ Co_3O_4/NiO_x can be attributed to the cathodic redox peaks associated with NiO_x,, which intersect the potential axis (E axis) at a nonzero potential vs $E^{o'}(O_2/H_2O)$) in the J-E behavior.) and under 100 mW cm^{-2} of simulated AM1.5G solar illumination. The J-E behavior of a non-photoactive p^+-Si/NiO_x electrode is also shown. The dark dashed line indicates the formal potential for water oxidation, $E^{o'}(O_2/H_2O)$.

been directly sputtered with NiO_x (photocurrent-onset potential of +150 ± 20 mV relative to $E^{o'}(O_2/H_2O)$ and negligible photocurrent density at $E^{o'}(O_2/H_2O)$) [29].

With these same n-Si substrates at a comparable light-limited current density, a high-quality semiconductor/liquid junction formed between a freshly etched n-Si photoanode [17] and a non-aqueous solution containing a reversible, one-electron redox couple (e.g., CH_3OH-0.20 M 1,1'-dimethylferrocene (Me_2Fc^0)-0.010 M Me_2Fc^+) which forms an in-situ emitter by virtue of carrier inversion[40] yielded a photocurrent-onset potential of -640 mV relative to $E^{o'}(Me_2Fc^{+/0})$ (Figure 2.6). We therefore expect that improvements

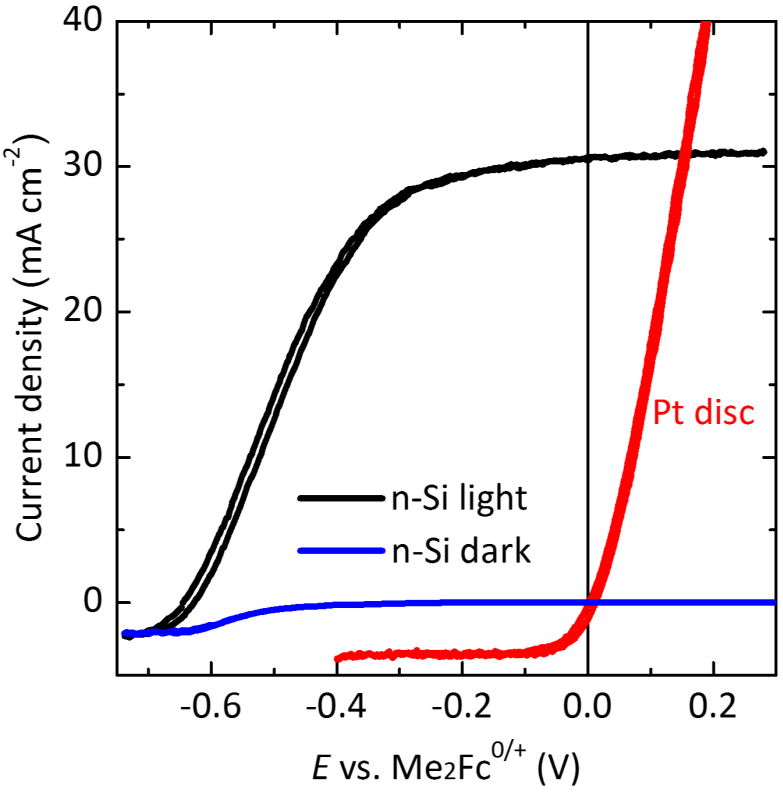

Figure 2.6: J-E behavior of a freshly etched n-Si photoanode in contact with 0.20 M Me_2Fc/0.010 M Me_2Fc^+ in CH_3OH with 1.5 M $LiClO_4$ added as a supporting electrolyte and under 100 mW cm^{-2} of ELH-type W-halogen illumination (black) and in the dark (blue).

upon the 0.56 V V_{oc} yielded by the n-Si/$SiO_{x,RCA}$/Co_3O_4/NiO_x structure could be obtained through decreasing the defect densities at the Si surface and yet further increases in the band bending in the Si.

Figure 2.7 shows the wavelength-dependent external quantum yield (ϕ_{ext}) for electrons collected from n-Si/$SiO_{x,RCA}$/Co_3O_4/NiO_x and np^+-Si/NiO_x [29] photoanodes, respectively, in contact with 1.0 M KOH(aq) while under potentiostatic control at 1.93 V versus RHE. Figure 2.7 also displays the observed absorptance spectrum of an n-Si/$SiO_{x,RCA}$/Co_3O_4/NiO_x photoanode in air for light at normal incidence. The shape of the (ϕ_{ext}) versus wavelength behavior for the n-Si/$SiO_{x,RCA}$/Co_3O_4/NiO_x electrode was consistent with the absorptance spectrum of the NiO_x-coated Si substrate measured in air [29]. The n-Si/$SiO_{x,RCA}$/Co_3O_4/NiO_x photoanodes exhibited higher (ϕ_{ext}) values at wavelengths < 500 nm relative to those of np^+-Si/NiO_x photoanodes, indicating that the

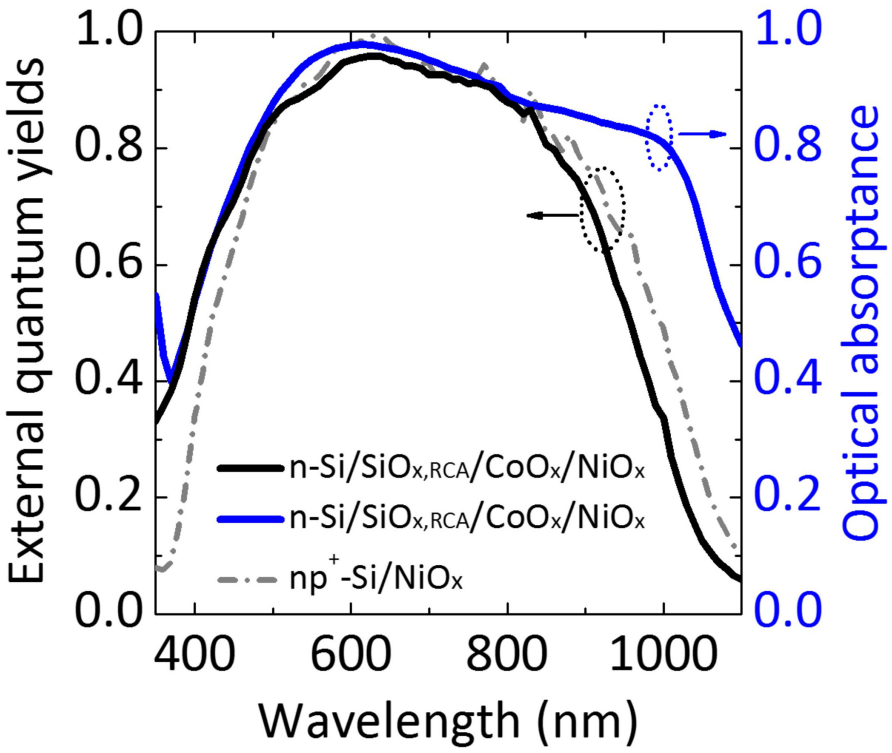

Figure 2.7: Wavelength-dependent external quantum yield for n-Si/$SiO_{x,RCA}$/Co_3O_4/NiO_x (black) and np^+-Si/NiO_x (gray dash and dot) photoanodes in contact with 1.0 M KOH(aq) and held potentiostatically at 1.93 V versus a reversible hydrogen electrode (RHE) while illuminated by light that had been passed through a monochromator. The data for the np^+-Si/NiO_x photoanode are extracted from reference [29]. The optical absorptance for the n-Si/$SiO_{x,RCA}$/Co_3O_4/NiO_x photoanode is shown in blue.

n-Si/$SiO_{x,RCA}$/Co_3O_4/NiO_x heterojunction had lower parasitic absorption losses in the near-surface layer. In the homojunction device, short-wavelength light is significantly absorbed by the thin, non-photoactive, highly doped emitter layer [29], while in commercial high-efficiency Si photovoltaic devices, short-wavelength light is absorbed primarily by the heterogeneous passivation layers [41]. For the n-Si/$SiO_{x,RCA}$/Co_3O_4/NiO_x photoanodes, (ϕ_{ext}) was > 0.9 in the wavelength range of 550–780 nm, which compared favorably to (ϕ_{ext}) values of ≤ 0.75 across the wavelength range of 400–1100 nm reported for n-Si/$SiO_{x,RCA}$/TiO_2/Ni photoanodes measured under similar conditions [42]. The increased (ϕ_{ext}) for the NiO_x-coated photoanodes at wavelengths > 550 nm was due to the anti-reflective behavior of the NiO_x coating. Consistently, NiO_x-coated n-Si photoanodes produced light-limited current densities under 1 Sun simulated AM1.5 illumination that were ~ 4.5 mA cm^{-2} greater the light-limited current densities observed under such conditions from n-Si/$SiO_{x,RCA}$/TiO_2/Ni photoanodes.

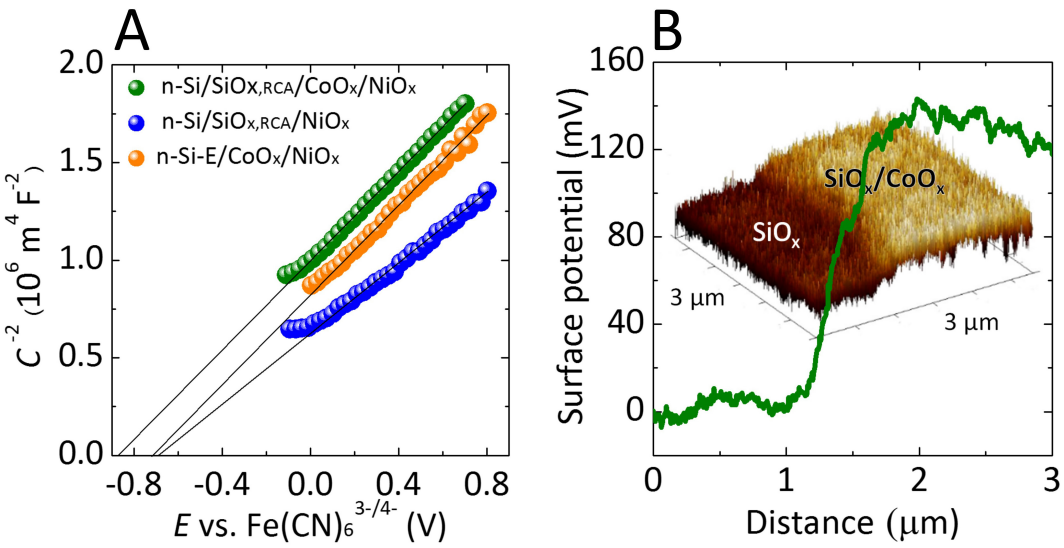

Figure 2.8: (A) Mott-Schottky (C^{-2} vs E) plots of the inverse of the differential capacitance of the electrode vs potential for an n-Si/$SiO_{x,RCA}$/NiO_x photoanode (blue), an n-Si–E/Co_3O_4/NiO_x photoanode (orange, n-Si-E indicates the n-Si was freshly etched in buffered HF (aq) before the next processing step), and an n-Si/$SiO_{x,RCA}$/Co_3O_4/NiO_x photoanode (green). (B) Kelvin probe force microscopy images showing the change in potential as the probe was scanned from the n-Si/$SiO_{x,RCA}$ surface to the n-Si/$SiO_{x,RCA}$/Co_3O_4 surface.

Electrochemical impedance spectroscopy was used to determine the differential capacitance (C) of the n-Si/$SiO_{x,RCA}$/NiO_x, n-Si–E/Co_3O_4/NiO_x (where n-Si-E indicates n-Si which was freshly etched in buffered HF (aq) before the next processing step), and n-Si/$SiO_{x,RCA}$/Co_3O_4/NiO_x electrodes, with Mott-Schottky plots (C^{-2} vs E) indicating flat-band potentials (Vfb) of -0.67 ± 0.02 V, -0.69 ± 0.03 V, and -0.83 ± 0.02 V versus $(Fe(CN)_6^{3-/4-})$, respectively (Figure 2.8A). The slopes in the linear regions of the C^{-2} vs E plots yielded a doping density of $\sim 10^{17}$ cm^{-3} for all electrodes (see Appendix A.2), which implies a corresponding resistivity of ~ 0.09 ohm cm, close to the range of 0.1 – 1 ohm cm specified by the manufacturer of the Si wafer. Kelvin-probe force microscopy (KPFM, Figure 2.8B) showed that the work function of the Co_3O_4 layer was 120 mV greater than that for n-Si/$SiO_{x,RCA}$ surfaces, indicating that the energy-band structure at the n-Si/$SiO_{x,RCA}$/Co_3O_4 interface was significantly different than that at the n-Si/$SiO_{x,RCA}$ interface. The negative shift in Vfb for the n-Si/$SiO_{x,RCA}$/Co_3O_4/NiO_x electrode relative to the n-Si/$SiO_{x,RCA}$/NiO_x electrode is in accord with the KPFM data, as well as with the J-E behavior observed in 1.0 M KOH(aq) (Figure 2.5). The barrier height within the Si of n-Si/$SiO_{x,RCA}$/Co_3O_4/NiO_x as calculated from the 0.83 V ± 0.02 V flat-band potential was 0.98 V ± 0.02 V (see Appendix A.3), close to the band gap of Si. This

large band bending would likely result in the formation of a strong inversion layer at the surface of n-Si [43], and thus would result in larger observed photovoltages due to the associated improvements in charge-carrier separation and collection, reductions in rates of electron-hole recombination, and improvements in diffusion of charge carriers [44].

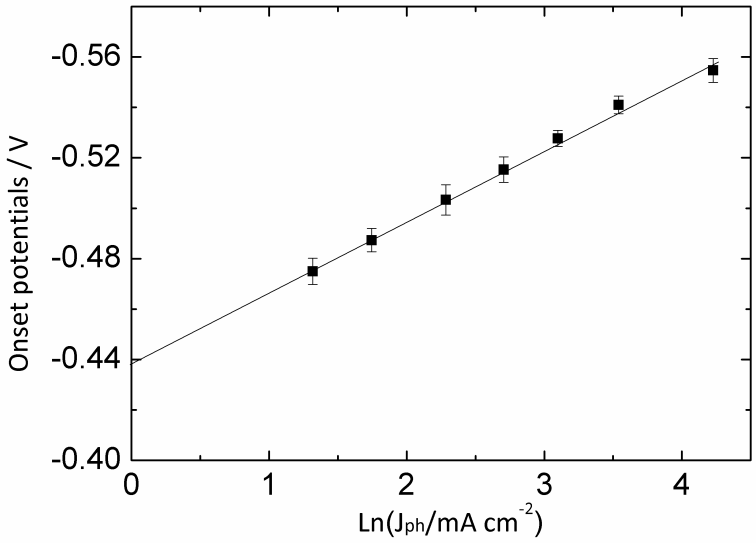

Figure 2.9: Photocurrent-onset potentials relative to $E^{\circ'}(Fe(CN)_6^{3-/4-})$ (Onset potentials for short) for an n-Si/$SiO_{x,RCA}$/Co_3O_4/NiO_x photoanode in contact with a solution of 0.35 M $K_4Fe(CN)_6$, 0.05 M $K_3Fe(CN)_6$ and 1.0 M KCl(aq) under 200 mW cm^{-2}, 100 mW cm^{-2}, 63 mW cm^{-2}, 40 mW cm^{-2}, 25 mW cm^{-2}, 16 mW cm^{-2}, and 10 mW cm^{-2} of AM 1.5G simulated illumination from a Xe lamp. Neutral density filters were used to attenuate the light intensity to produce the desired illumination levels at the sample surface.

The reverse-saturation current density and the diode quality factor for the n-Si/$SiO_{x,RCA}$/Co_3O_4/NiO_x photoanode, extracted by a linear fit of the dependence of the photocurrent-onset potentials relative to $E^{\circ'}(Fe(CN)_6^{3-/4-})$ on the logarithm of photocurrent density (J_{ph}) (Figure 2.9), were 1.50×10^{-7} mA cm^{-2} and 1.09, respectively. The diffusion current was $\sim 10^{-10}$ mA cm^{-2}, thus the thermionic emission current was the dominant contributor to the reverse-saturation current. Given a Richardson constant of 120 A cm^{-2} K^{-2} and a barrier height of 0.98 ± 0.02 V (see Appendix A.3), the transmission coefficient, α, was estimated to be on the order of unity.

Figure 2.10A shows the chronopotentiometric data for an n-Si/$SiO_{x,RCA}$/Co_3O_4/NiO_x photoanode in contact with 1.0 M KOH(aq) and held at 1.63 V versus RHE while under simulated 1 sun illumination of 100 mW cm^{-2}. The current density was 30 ± 2 mA cm^{-2}

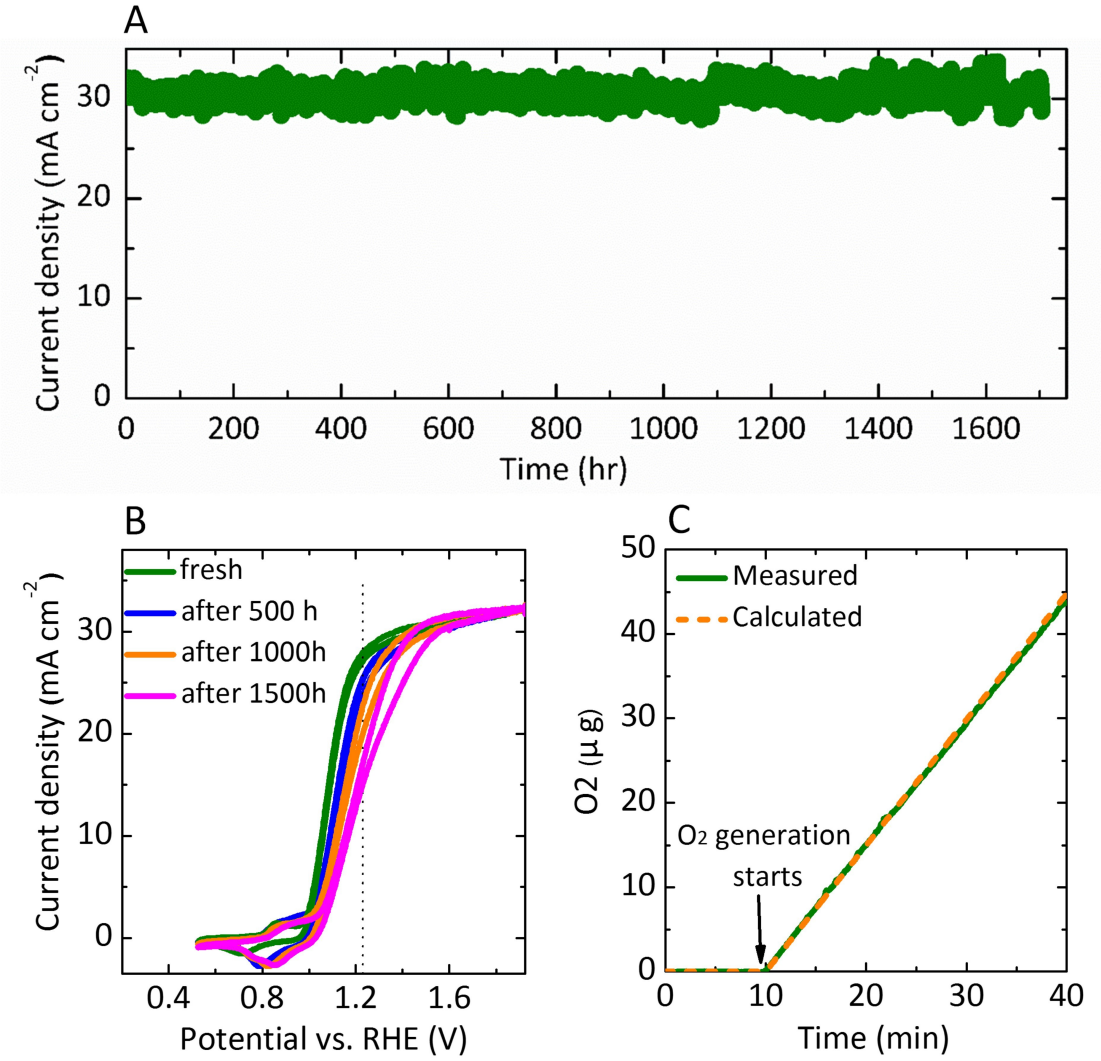

Figure 2.10: (A) Chronoamperometry of n-Si/$SiO_{x,RCA}$/Co_3O_4/NiO_x photoanodes biased at 1.63 V vs. RHE under 1 Sun of simulated 1.5G solar illumination from an ENH-type tungsten-halogen lamp. (B) Representative J-E behavior for an n-Si/$SiO_{x,RCA}$/Co_3O_4/NiO_x photoanode in contact with 1.0 M KOH(aq) under 100 mW cm^{-2} of AM 1.5G simulated solar illumination collected before, and after 500 h, 1000 h, and 1500 h of continuous operation at 1.63 V vs RHE. (C) Mass of O_2(g) generated (green line) by an n-Si/$SiO_{x,RCA}$/Co_3O_4/NiO_x photoanode held at a constant current density of 0.5 mA cm^{-2} for 30 min while under AM 1.5G simulated illumination and in contact with 1.0 M KOH(aq), as determined by a calibrated O_2 probe and as calculated based on the charge passed assuming 100% Faradaic efficiency for O_2 generation (orange dashed line).

for 1700 h of continuous operation, at which point the experiment was stopped. Cyclic voltammograms were collected every 10 h during the stability test (Figure 2.10B), and showed that the J-E behavior for the photoanode gradually shifted anodically throughout

the experiment. The photocurrent-onset potential relative to $E^{o'}(O_2/H_2O)$ shifted from -239 mV to -214 mV, -198 mV, and -185 mV while the photocurrent density at $E^{o'}(O_2/H_2O)$ decreased from 27.9 mA cm^{-2} to 24.6 mA cm^{-2}, 21.4 mA cm^{-2} and 16.2 mA cm^{-2} after 500 h, 1000 h, and 1500 h respectively. Hence the solar-to-O_2(g) value for η_{IRC} [34] decreased from 2.2% to 1.5%, 1.1%, and 0.74% after 500 h, 1000 h, and 1500 h of operation, respectively. The gradual decrease in performance may result from the generation of SiO_x islands at pinholes in the sputtered NiO_x film and/or from an increase in resistivity arising from thickening of the SiO_x layer in the interface, as well as from the slow electrochemical conversion of Co_3O_4 to $Co(OH)_2$ and then to ion-permeable CoOOH (Figure 2.11) and the loss of catalytic activity. The stability of n-Si/$SiO_{x,RCA}$/Co_3O_4/NiO_x photoanodes was comparable to the reported stability of np^+-Si/NiO_x photoanodes,[29] demonstrating that the interfacial Co_3O_4 layer did not adversely affect the stability of the NiO_x coating.

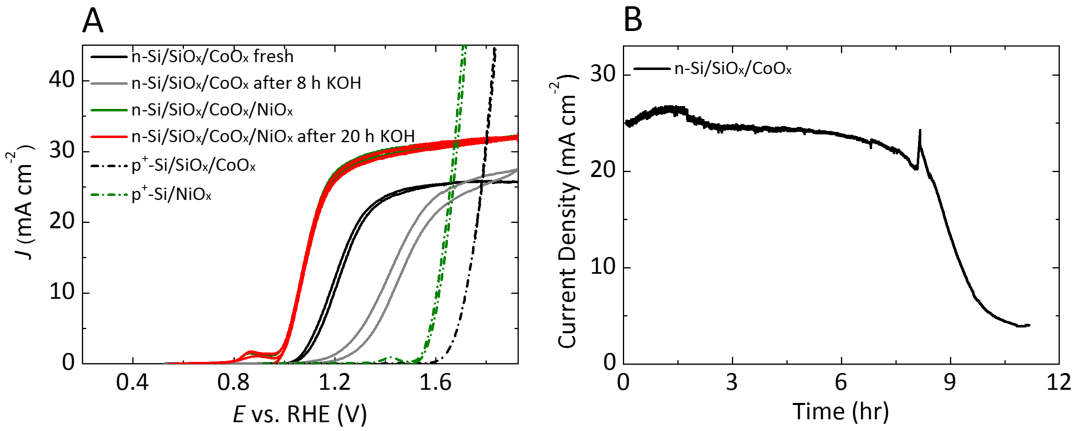

Figure 2.11: (A) Representative current-density versus potential (J-E) behavior of n-Si/$SiO_{x,RCA}$/ Co_3O_4 and n-Si/$SiO_{x,RCA}$/Co_3O_4/NiO_x photoanodes in contact with 1.0 M KOH(aq) under 100 mW cm^{-2} of AM 1.5G simulated solar illumination before and after 8 h and 20 h of continuous operation at 1.63 V vs RHE, respectively. The J-E behavior of p^+-Si/$SiO_{x,RCA}$/Co_3O_4 and p^+-Si/NiO_x is also shown. (B) Chronoamperometry of an n-Si/$SiO_{x,RCA}$/Co_3O_4 photoanode biased at 1.63 V vs RHE under 100 mW cm^{-2} of simulated 1.5 G solar illumination from an ENH-type tungsten-halogen lamp.

Figure 2.10A shows the mass of O_2(g) generated, as determined using a calibrated oxygen probe, by an n-Si/$SiO_{x,RCA}$/Co_3O_4/NiO_x photoanode in contact with 1.0 M KOH(aq) under galvanostatic control for 30 min at a current density of 0.5 mA cm^{-2}. The measured mass of O_2(g) was in agreement with that calculated based on the charge passed, assuming 100% Faradaic efficiency for the generation of O_2(g). The total charge passed during the stability test was 1×10^7 greater than the total charge needed to dissolve the

Co_3O_4 interfacial layer, and was 1×10^2 greater than the charge required to dissolve the entire Si substrate (see Appendix A.4 and A.5). Assuming a 20% solar capacity factor, the 1700 h of stable water oxidation measured for the n-Si/$SiO_{x,RCA}$/Co_3O_4/NiO_x photoanode in contact with 1.0 M KOH(aq) represented the same amount of anodic charge density as would be passed in approximately one year of operation in the field at a maximum photocurrent density of 30 mA cm^{-2}.

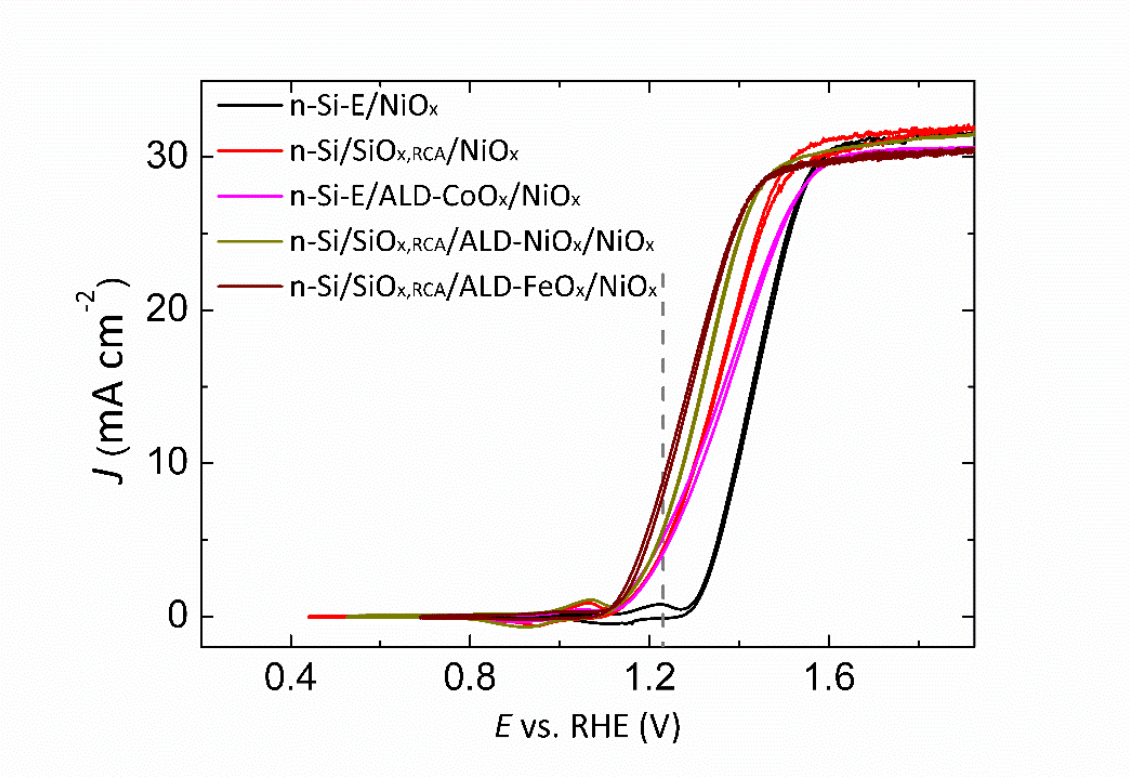

Figure 2.12: Representative J-E data for photoanodes in 1.0 M KOH(aq) under 100 mW cm^{-2} of simulated AM1.5G solar illumination. n-Si-E indicates that the n-Si was freshly etched in buffered HF(aq) before the next processing step. $SiO_{x,RCA}$ indicates that the RCA SC-2 etching procedure generated SiO_x. A nominally identical reactive RF sputtering process was used to deposit the multifunctional NiO_x layer onto each of these electrodes.

The thin layer of chemically grown silicon oxide present on the n-Si substrates prior to further processing by ALD and sputtering contributes to the improvement in performance observed when comparing n-Si/$SiO_{x,RCA}$/Co_3O_4/NiO_x photoanodes to n-Si/Co_3O_4/NiO_x photoanodes (Figure 2.8A, S7). Both ALD and sputtering result in the growth of a thin layer of SiO_x on freshly etched silicon surfaces. The properties of the SiO_x layers produced by the different processing methods vary, and affect the performance of devices. The chemically grown SiO_x layer may result in fewer trap states at the Si/SiO_x interface

than are produced by the sputtered SiO_x, and/or may serve to protect the underlying silicon from arcs and surface roughening during the RF sputtering process. In addition, the SiO_x layer likely contributes to the initiation and conformity of the ALD growth process for the Co_3O_4 interfacial films, which on freshly etched Si surfaces would be expected to proceed via inhomogeneous island growth that can result in rough films as well as in interfacial silicon oxides or silicates [45], and in reduced values for the flat-band and photocurrent-onset potentials.

Although this work has focused on the use of interfacial layers of ALD-grown Co_3O_4, other transition-metal oxides, including FeO_x and NiO_x, also hold promise for use as interfacial layers on Si photoanodes protected by sputtered NiO_x (Figure 2.12).

2.4 Conclusions

This work clearly demonstrates that the introduction of ALD layers of cobalt oxide improves the equivalent open-circuit voltage of protected n-Si photoanodes to values comparable to that obtainable from photoanodes fabricated using homogeneous p-n buried Si junctions. Interfacial cobalt oxide layers increase the band bending at the interface and thereby offer a route to high-performance photoanodes, potentially simplifying the photoelectrode processing and allowing for the use of inexpensive polycrystalline absorbers while maintaining high photoelectrode performance.

References

[1] M. S. Wrighton, P. T. Wolczanski, and A. B. Ellis. “Photoelectrolysis of Water by Irradiation of Platinized n-type Semiconducting Metal Oxides”. In: *J. Solid State Chem.* 22.1 (1977), pp. 17–29.

[2] M. X. Tan et al. “Principles and Applications of Semiconductor Photoelectrochemistry”. In: *Prog. Inorg. Chem.* 41 (1994), pp. 21–144.

[3] M. G. Walter et al. “Solar Water Splitting Cells”. In: *Chem. Rev.* 110.11 (2010), pp. 6446–6473.

[4] K. Rajeshwar, N. R. de Tacconi, and C. R. Chenthamarakshan. “Semiconductor-based Composite Materials: Preparation, Properties, and Performance”. In: *Chem. Mater.* 13.9 (2001), pp. 2765–2782.

[5] F. R. F. Fan, G. A. Hope, and A. J. Bard. “Semiconductor Electrodes .46. Stabilization of n-Silicon Electrodes in Aqueous-solution Photo-electrochemical Cells by Formation of Platinum Silicide Layers”. In: *J. Electrochem. Soc.* 129.7 (1982), pp. 1647–1649.

[6] Y. Nakato et al. “Hydrogen Evolution and Iodine Reduction on an Illuminated n-p Junction Silicon Electrode and its Application to Efficient Solar Photoelectrolysis of Hydrogen Iodide”. In: *J. Phys. Chem.* 88.19 (1984), pp. 4218–4222.

[7] Y. Nakato et al. “P-N-Junction Silicon Electrode Coated with Noble-Metal for Efficient Solar Photoelectrolysis of Hydrogen Iodide”. In: *B. Chem. Soc. Jpn.* 57.2 (1984), pp. 355–360.

[8] S. W. Boettcher et al. “Photoelectrochemical Hydrogen Evolution Using Si Microwire Arrays”. In: *J. Am. Chem. Soc.* 133.5 (2011), pp. 1216–1219.

[9] H. Morisaki et al. “Photoelectrolysis of Water with TiO2-Covered Solar-Cell Electrodes”. In: *Appl. Phys. Lett.* 29.6 (1976), pp. 338–340.

[10] M. Matsumura et al. “Photoelectrochemical Hydrogen Evolution Using Amorphous Silicon Electrodes having p-i-n or p-i-n-p-i-n Junctions”. In: *Sol. Energy Mater.* 13.1 (1986), pp. 57–64.

[11] J. D. Luttmer, D. Konrad, and I. Trachtenberg. “Electrode Materials for Hydrobromic Acid Electrolysis in Texas-Instruments Solar Chemical Converter”. In: *J. Electrochem. Soc.* 132.5 (1985), pp. 1054–1058.

[12] E. L. Warren et al. “Hydrogen-evolution Characteristics of Ni-Mo-coated, Radial Junction, n+p-silicon Microwire Array Photocathodes”. In: *Energy Environ. Sci.* 5.11 (2012), pp. 9653–9661.

[13] G. Hodes et al. “Heterojunction Silicon Indium Tin Oxide Photo-Electrodes - Development of Stable Systems in Aqueous-Electrolytes and their Applicability to Solar-Energy Conversion and Storage”. In: *J. Am. Chem. Soc.* 105.3 (1983), pp. 324–330.

[14] J. A. Switzer. “The n-Silicon Thallium(Iii) Oxide Heterojunction Photoelectrochemical Solar-Cell”. In: *J. Electrochem. Soc.* 133.4 (1986), pp. 722–728.

[15] W. Kautek and H. Gerischer. “The Photoelectrochemistry of the Aqueous Iodide Iodine Redox System at n-type MoSe2-Electrodes”. In: *Electrochim. Acta* 26.12 (1981), pp. 1771–1778.

[16] A. Heller. “Conversion of Sunlight into Electrical-Power and Photoassisted Electrolysis of Water in Photoelectrochemical Cells”. In: *Accounts Chem. Res.* 14.5 (1981), pp. 154–162.

[17] F. Gstrein et al. “Effects of Interfacial Energetics on the Effective Surface Recombination Velocity of Si/liquid Contacts”. In: *J. Phys. Chem. B* 106.11 (2002), pp. 2950–2961.

[18] D. V. Esposito et al. “H2 Evolution at Si-based Metal-insulator-semiconductor Photoelectrodes Enhanced by Inversion Channel Charge Collection and H Spillover”. In: *Nat. Mater.* 12.6 (2013), pp. 562–568.

[19] W. Siripala et al. “A Cu2O/TiO2 Heterojunction Thin Film Cathode for Photoelectrocatalysis”. In: *Sol. Energy Mat. Sol. C.* 77.3 (2003), pp. 229–237.

[20] M. Moriya et al. “Stable Hydrogen Evolution from CdS-Modified CuGaSe2 Photoelectrode under Visible-Light Irradiation”. In: *J. Am. Chem. Soc.* 135.10 (2013), pp. 3733–3735.

[21] Y. J. Hwang, A. Boukai, and P. D. Yang. “High Density n-Si/n-TiO2 Core/Shell Nanowire Arrays with Enhanced Photoactivity”. In: *Nano Lett.* 9.1 (2009), pp. 410–415.

[22] M. J. Kenney et al. “High-Performance Silicon Photoanodes Passivated with Ultrathin Nickel Films for Water Oxidation”. In: *Science* 342.6160 (2013), pp. 836–40.

[23] O. Khaselev and J. A. Turner. “A Monolithic Photovoltaic-Photoelectrochemical Device for Hydrogen Production via Water Splitting”. In: *Science* 280.5362 (1998), pp. 425–427.

[24] R. E. Rocheleau, E. L. Miller, and A. Misra. “High-efficiency Photoelectrochemical Hydrogen Production using Multijunction Amorphous Silicon Photoelectrodes”. In: *Energy Fuel.* 12.1 (1998), pp. 3–10.

[25] S. Licht et al. “Efficient Solar Water Splitting, Exemplified by RuO2-catalyzed AlGaAs/Si Photoelectrolysis”. In: *J. Phys. Chem. B* 104.38 (2000), pp. 8920–8924.

[26] E. L. Miller, R. E. Rocheleau, and X. M. Deng. “Design Considerations for a Hybrid Amorphous Silicon/Photoelectrochemical Multijunction Cell for Hydrogen Production”. In: *Int. J. Hydrogen Energy* 28.6 (2003), pp. 615–623.

[27] S. Y. Reece et al. “Wireless Solar Water Splitting Using Silicon-Based Semiconductors and Earth-Abundant Catalysts”. In: *Science* 334.6056 (2011), pp. 645–648.

[28] Y. Yamada et al. “One Chip Photovoltaic Water Electrolysis Device”. In: *Int. J. Hydrogen Energy* 28.11 (2003), pp. 1167–1169.

[29] K. Sun et al. “Stable Solar-Driven Water Oxidation to O2(g) by Ni-oxide Coated Silicon Photoanodes”. In: *J. Phys. Chem. Lett.* 6 (2015), pp. 592–598.

[30] K. Sun et al. “Sputtered NiOx Films for Stabilization of p+n-InP Photoanodes for Solar-Driven Water Oxidation”. In: *Adv. Energy Mater.* (2015), p. 1402276.

[31] K. Sun et al. “Stable Solar-Driven Oxidation of Water by Semiconducting Photoanodes Protected by Transparent Catalytic Nickel Oxide Films”. In: *Proc. Natl. Acad. Sci. U.S.A.* 112 (2015), pp. 3612–3617.

[32] N. C. Strandwitz et al. “Photoelectrochemical Behavior of n-type Si(100) Electrodes Coated with Thin Films of Manganese Oxide Grown by Atomic Layer Deposition”. In: *J. Phys. Chem. C* 117.10 (2013), pp. 4931–4936.

[33] Y. W. Chen et al. “Atomic Layer-Deposited Tunnel Oxide Stabilizes Silicon Photoanodes for Water Oxidation”. In: *Nat. Mater.* 10.7 (2011), pp. 539–44.

[34] R. H. Coridan et al. “Methods for Comparing the Performance of Energy-Conversion Systems for Use in Solar Fuels and Solar Electricity Generation”. In: *Energy Environ. Sci.* (2015).

[35] K. Sun et al. “Enabling Silicon for Solar-Fuel Production”. In: *Chem. Rev.* 114.17 (2014), pp. 8662–8719.

[36] A. J. Nozik. “Photochemical Diodes”. In: *Appl. Phys. Lett.* 30.11 (1977), pp. 567–569.

[37] A. Heller. In: *Photoeffects at Semiconductor-Electrolyte Interfaces*. Vol. 146. ACS Symposium Series. Washington, D.C.: American Chemical Society, 1981. Chap. 4, pp. 57–77.

[38] M. C. Biesinger et al. “Resolving Surface Chemical States in XPS Analysis of First Row Transition Metals, Oxides and Hydroxides: Cr, Mn, Fe, Co and Ni”. In: *Appl. Surf. Sci.* 257.7 (2011), pp. 2717–2730.

[39] J. Yang et al. “Synthesis and Characterization of Cobalt Hydroxide, Cobalt Oxyhydroxide, and Cobalt Oxide Nanodiscs”. In: *J. Phys. Chem. C* 114.1 (2010), pp. 111–119.

[40] M. L. Rosenbluth, C. M. Lieber, and N. S. Lewis. “630 mV Open Circuit Voltage, 12% Efficient n-Si Liquid Junction”. In: *Appl. Phys. Lett.* 45.4 (1984), pp. 423–425.

[41] H.-P. Wang et al. “High-Performance a-Si/c-Si Heterojunction Photoelectrodes for Photoelectrochemical Oxygen and Hydrogen Evolution”. In: *Nano Lett.* (2015).

[42] S. Hu et al. “Amorphous TiO(2) Coatings Stabilize Si, GaAs, and GaP Photoanodes for Efficient Water Oxidation”. In: *Science* 344.6187 (2014), pp. 1005–9.

[43] R. Memming. *Semiconductor Electrochemistry*. Weinheim, Federal Republic of Germany: Wiley, 2001.

[44] Z. Zhang and J. T. Yates. “Band Bending in Semiconductors: Chemical and Physical Consequences at Surfaces and Interfaces”. In: *Chem. Rev.* 112.10 (2012), pp. 5520–5551.

[45] M. M. Frank et al. “Enhanced Initial Growth of Atomic-layer-deposited Metal Oxides on Hydrogen-terminated Silicon”. In: *Appl. Phys. Lett.* 83.4 (2003), pp. 740–742.

Chapter 3

570 MV PHOTOVOLTAGE, STABILIZED N – SI/CO_3O_4 HETEROJUNCTION PHOTOANODES FABRICATED USING ATOMIC LAYER DEPOSITION

[1]Heterojunction photoanodes, consisting of n-type crystalline Si(100) substrates coated with a thin ~50 nm film of cobalt oxide fabricated using atomic-layer deposition (ALD), exhibited photocurrent-onset potentials of -205 ± 20 mV relative to the formal potential for the oxygen-evolution reaction (OER), ideal regenerative solar-to-O_2(g) conversion efficiencies of 1.42 ± 0.20%, and operated continuously for over 100 days (~2500 h) in 1.0 M KOH(aq) under simulated solar illumination. The ALD Co_3O_4 thin film (i) formed a heterojunction with the n-Si(100) that provided a photovoltage of 575 mV under 1 Sun of simulated solar illumination, (ii) stabilized Si photoanodes that are otherwise unstable when operated in aqueous alkaline electrolytes, and (iii) catalyzed the oxidation of water, thereby reducing the kinetic overpotential required for the reaction and increasing the overall efficiency relative to electrodes that do not have an inherently electrocatalytic coating. The process provides a simple, effective method for enabling the use of planar n-Si(100) substrates as efficient and durable photoanodes in fully integrated, photovoltaic-biased solar fuels generators.

3.1 Introduction

The sustainable electrochemical production of fuels from aqueous electrolytes, accomplished either by reducing water to generate H_2(g) or by reducing CO_2(g) and water to generate hydrocarbons, requires the concomitant oxidation of water to O_2(g), to liberate the electrons needed for the fuel-forming reactions[1–4]. Efficient, intrinsically safe solar-driven water-splitting systems can be constructed in strongly alkaline or strongly acidic electrolytes[5–7]. Such electrolytes also allow the use of commercially available, gas-impermeable, ion-exchange membranes, which have been developed for fuel cells and electrolyzers that use acidic or alkaline electrolytes[8].

Protective coatings can stabilize technologically important small-band-gap semiconductors for use as oxygen-evolving photoanodes, even in strongly alkaline electrolytes. At least four types of protective coatings have been developed[9, 10]: TiO_2, either in an insu-

[1]This chapter is based on results in: X. Zhou, R. Liu, K. Sun, K. M. Papadantonakis, B. S. Brunschwig and N. S. Lewis, Energy Environ. Sci., 2016, 9, 892 - Published by The Royal Society of Chemistry.

lating form as a thin (few nm thick) insulating tunnel barrier or in a "leaky" form as a thick (multiple tens of nm) anodically conductive barrier[11–16]; thin metallic coatings[3]; and p-type transparent, conductive transition-metal oxides[13, 17–21]. In addition to serving as a physical barrier between the semiconductor and electrolyte, the protective coating should provide high interfacial charge-transfer rates and either be inherently catalytic for the oxygen-evolution reaction (OER) or should support an active OER electrocatalyst, to reduce the kinetic overpotential required for the reaction as well as to assist in the removal of reactive photogenerated holes from the surface of the semiconductor[22, 23]. Protective coatings have been demonstrated to extend the lifetime of photoanodes fabricated from semiconductors such as Si, InP, and CdTe, which can form surface layers of insoluble, passivating oxides during operation[13, 18].

Integration of protection layers into efficient photoanodes generally has required deposition of the protection layer on top of a homogeneous np^+ buried junction[13, 18, 24]. However, high quality emitters or heterojunctions cannot be formed on many semiconductors. Furthermore, formation of diffused junctions on inexpensive, small grain size, polycrystalline or thin film semiconductors generally results in preferential migration of dopants down the grain boundaries, and thus produces deleterious minority-carrier recombination and majority-carrier shunts in the resulting device[25].

Co_3O_4 is an electrocatalyst for the evolution of O_2(g) from aqueous alkaline solutions[26, 27], and has been explored as a protective coating for photoanodes[10, 19, 28]. Co_3O_4 protective layers have been reported to provide only limited stability (a few hours or less) against corrosion of photoanodes in strongly alkaline solutions[10, 28], or require substrates with homogeneous np^+ buried junctions to produce high photovoltages[19]. Recently, deposition of a thin (~2 nm) film of cobalt oxide (Co_3O_4) prior to the sputter deposition of a multifunctional and protective NiO_x coating onto n-Si surfaces has yielded photoanodes with an electrochemical performance that approaches the Shockley diode limit for the substrate. The interfacially engineered n-Si/$SiO_{x,RCA}$/Co_3O_4/NiO_x structure demonstrates the fabrication of a stable and efficient device that utilizes a direct heterojunction contact between an n-Si substrate and a protective coating, thereby obviating the need for homogeneous np^+ buried junctions in this system[29].

We demonstrate herein that stable, high photovoltage anodes for the oxidation of water from strongly alkaline electrolytes can be fabricated from n-Si substrates protected by a uniform layer of Co_3O_4 formed using atomic-layer deposition (ALD). The ability to fabricate a stable photoanode by deposition of a protective and electrocatalytic coating directly onto a planar substrate without sacrificing device efficiency simplifies the

fabrication processes needed to obtain efficient and stable photoanodes for solar-driven water oxidation on Si surfaces. Though a thin interfacial layer of Co_3O_4 on n-Si, with an active OER catalyst of sputtered NiO_x film provides increased solar-to-O_2(g) conversion efficiency relative to an n-Si photoanode protected by a multi-functional layer of ALD Co_3O_4, the n-Si/$SiO_{x,RCA}$/Co_3O_4 photoanodes exhibited a lower decay rate of their solar-to-O_2(g) conversion efficiency than n-Si/$SiO_{x,RCA}$/Co_3O_4/NiO_x photoanodes due to a compact and uniform ALD Co_3O_4 protection layer, along with a simplified fabrication process including lower temperature and fewer processing steps.

3.2 Experimental

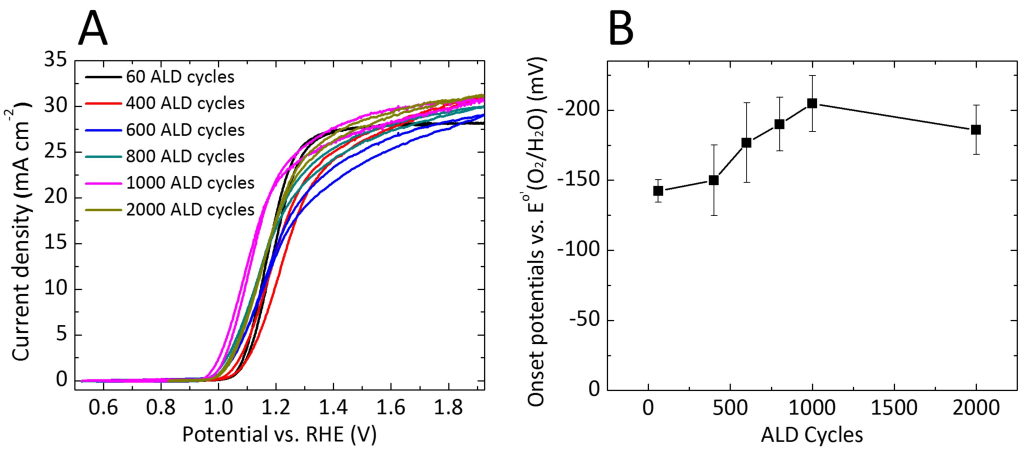

Figure 3.1: (A) Representative J-E behavior of n-Si/$SiO_{x,RCA}$/Co_3O_4 photoanodes with different Co_3O_4 thickness in 1.0 M KOH under 110 mW cm^{-2} of simulated solar illumination. (B) Dependence of photocurrent-onset potentials relative to the formal potential for the oxygen-evolution reaction (OER) on the thickness of the Co_3O_4 layer for n-Si/$SiO_{x,RCA}$/Co_3O_4 photoanodes, as indicated by the number of ALD cycles used to deposit the coating.

Detailed experimental procedures are provided in Appendix B. Briefly, planar Si(100) substrates (0.1-1 ohm cm resistivity, 525 μm thick) were immersed in a Radio Corporation of America Standard Clean-2 (RCA SC-2) etchant for 10 min at 75 °C. This procedure resulted in a thin (~2 nm) SiO_x layer on the surface of the Si (Si/$SiO_{x,RCA}$). Co_3O_4 films were deposited via ALD onto Si/$SiO_{x,RCA}$ substrates at 150 °C, with each ALD cycle consisting of a 2 s pulse of a cobaltocene precursor, a 10 s N_2(g) purge at a flow rate of 20 cm^3 min^{-1}, a 5 s pulse of ozone, and another 10 s N_2(g) purge. 1000 ALD cycles (~ 50 nm) of Co_3O_4 deposition produced optimal photocurrent-onset potentials relative to the formal potential for the oxygen-evolution reaction (OER) ($E^{o'}(O_2/H_2O)$ = 1.23 V versus

a reversible hydrogen electrode, RHE, at pH = 14) for n-Si/$SiO_{x,RCA}$/Co_3O_4 photoanodes (Figure 3.1, and Appendix A.6 discussions about trends of photocurrent-onset potentials change as a function of ALD cycles).

3.3 Results and Discussion

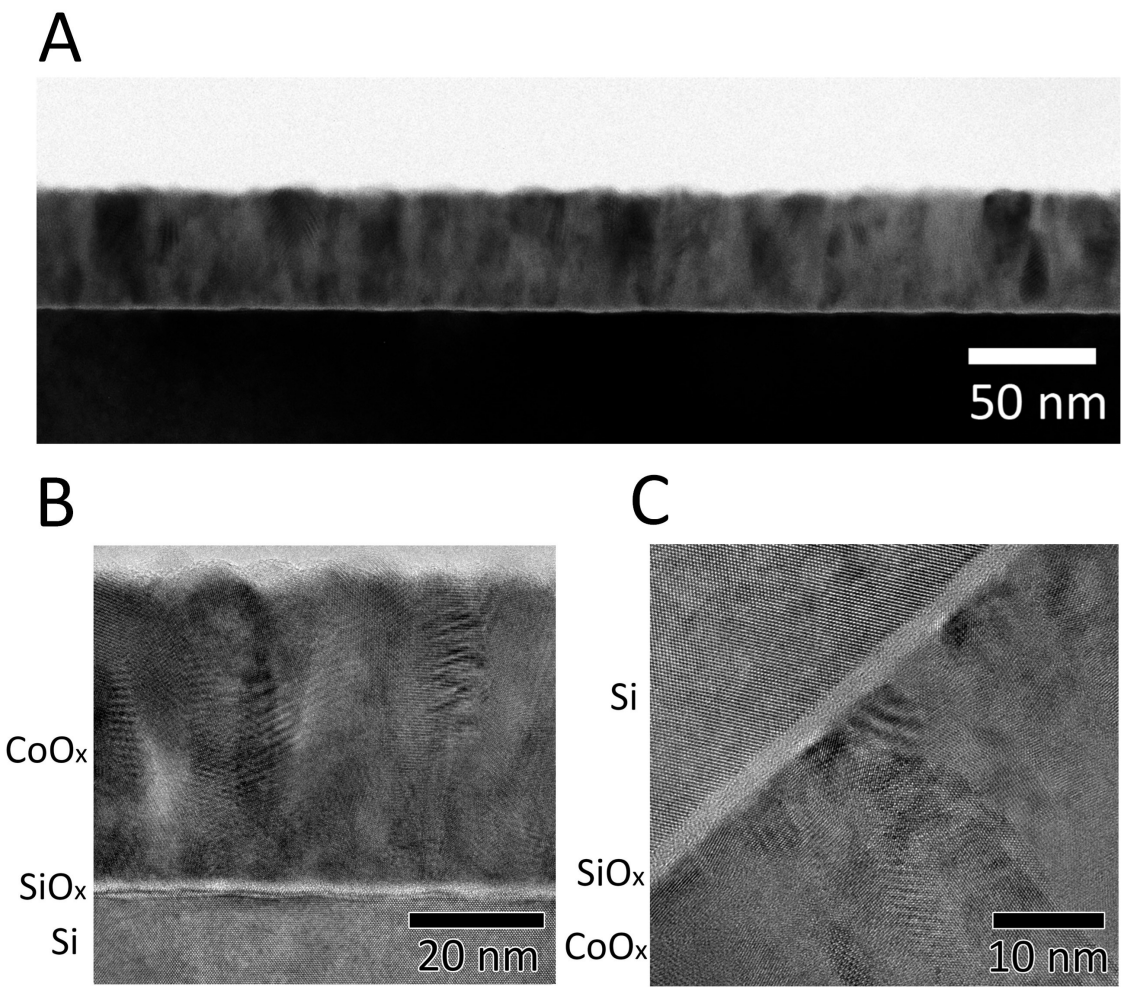

Figure 3.2: (A) Low-magnification bright-field transmission-electron micrograph (TEM) of a cross-section of an n-Si/$SiO_{x,RCA}$/Co_3O_4 electrode. (B, C) High-resolution TEM cross-sectional image of an n-Si/$SiO_{x,RCA}$/Co_3O_4 sample. The Co_3O_4 regions show the polycrystalline structure of the Co_3O_4 film.

Figure 3.2A shows a cross-sectional bright-field mode transmission-electron micrograph of the n-Si/$SiO_{x,RCA}$/Co_3O_4 interface. The black region at the bottom of the image corresponds to the Si wafer, the thin bright region atop the Si corresponds to SiO_x, and the polycrystalline layer atop the Si corresponds to the compact Co_3O_4 film, which was uniformly smooth and $\sim$ 50 nm thick, consistent with the low surface roughness (0.74

nm) determined using atomic-force microscopy (AFM, Figure 3.3A). Figures 3.2B and 3.2C show high-resolution transmission-electron microscope (HRTEM) images of the interface. An amorphous SiO_x layer ~2 nm thick was present between the Si substrate and the Co_3O_4 layer, and crystalline grain boundaries were evident in the Co_3O_4 regions of the image. The grain boundaries and in/out-of-plane orientation of the diffraction patterns suggest that the ALD Co_3O_4 films deposited at 150 °C using these methods were polycrystalline rather than amorphous, consistent with results obtained previously using grazing incidence X-ray diffractometry (GIXRD)[29].

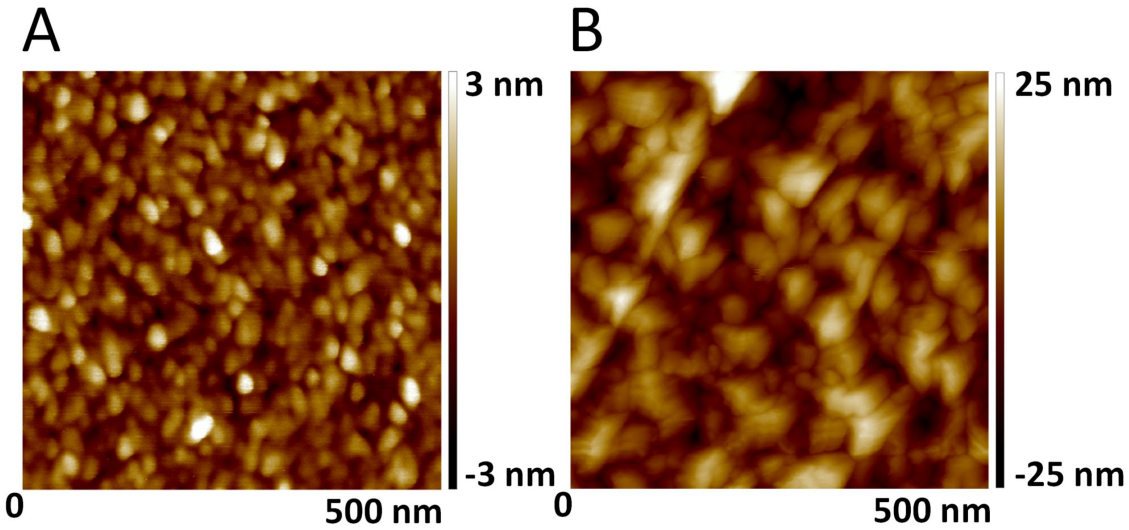

Figure 3.3: AFM image showing the surface morphology of an n-Si/$SiO_{x,RCA}$/Co_3O_4 device (A) before and (B) after the PEC stability test biased at 1.63 V vs RHE under 1.1 Sun of simulated solar illumination in contact with 1.0 M KOH(aq). The root-mean-square surface roughnesses were (A) 0.74 nm and (B) 7.2 nm. The increased surface roughness indicated the dissolution of the Co_3O_4 layer in 1.0 M KOH(aq) solution under bias and the possibility of pinholes formation. As a result, the interface between Co_3O_4/Si would be influenced after the long-term stability test. The reasons for the performance decay would come from both catalyst degradation and interface changes.

Figure 3.4A shows typical current-density versus potential (J-E) behavior for n-Si/$SiO_{x,RCA}$/Co_3O_4 photoanodes in contact with 1.0 M KOH(aq), in the dark or under 1.1 Sun of simulated solar illumination provided by a Xe lamp with AM1.5G filters. The behavior of a nonphotoactive p^+-Si/$SiO_{x,RCA}$/Co_3O_4 electrode is also shown under the same conditions. The light-limited photocurrent density was 30.2 ± 1.1 mA cm^{-2} under these conditions (1.1 Sun illumination), and corresponds to a photocurrent density of ~27 mA cm^{-2} under 1 Sun illumination. Figure 3.4B shows the spectral response data (external quantum yield as a function of wavelength) for an n-Si/$SiO_{x,RCA}$/Co_3O_4 photoanode in contact with 1.0

M KOH(aq) while the sample was maintained at 1.93 V versus RHE. When integrated with respect to the spectral irradiance distribution of the AM 1.5G 1.1 Sun solar spectrum, the spectral response of the n-Si/$SiO_{x,RCA}$/Co_3O_4 would be expected to yield a photocurrent density of 30.6 mA cm^{-2}, in good agreement with the observed light-limited photocurrent observed under 1.1 Sun illumination (see Appendix A.7 for detailed calculations).

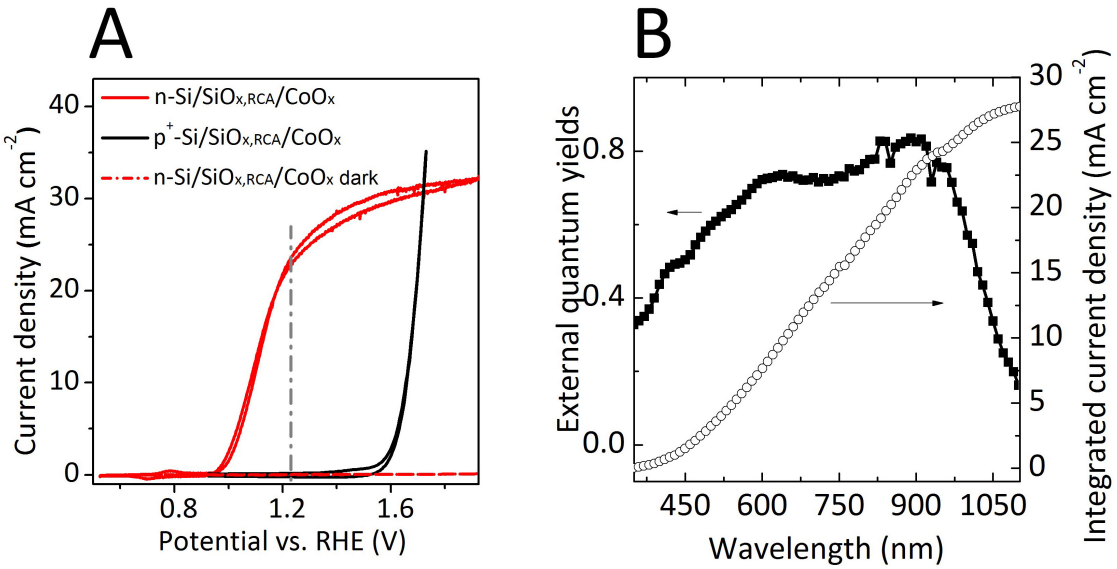

Figure 3.4: (A) Representative current-density versus potential (J-E) behavior for n-Si/ $SiO_{x,RCA}$/ Co_3O_4 photoanodes in contact with a 1.0 M KOH(aq) solution in the dark or under 110 mW cm^{-2} of simulated AM1.5G solar illumination. The J-E behavior of a non-photoactive p^+-Si/$SiO_{x,RCA}$/Co_3O_4 electrode is also shown. (B) External quantum yield for an n-Si/$SiO_{x,RCA}$/Co_3O_4 photoanode biased at 1.93 V versus a reversible hydrogen electrode (RHE) in contact with 1.0 M KOH(aq) while illuminated by light that had been passed through a monochromator (left ordinate), and the current density derived by integrating the external quantum yield with respect to the AM1.5G spectrum (right ordinate).

A representative n-Si/$SiO_{x,RCA}$/Co_3O_4 photoanode exhibited a photocurrent-onset potential of -212 mV relative to $E^{o'}(O_2/H_2O)$, 23.2 mA cm^{-2} of photocurrent density at $E^{o'}(O_2/H_2O)$, and a solar-to-O_2(g) ideal-regenerative-cell conversion efficiency, IRC, of 1.5% [30]. With three n-Si/$SiO_{x,RCA}$/Co_3O_4 electrodes tested, the photocurrent-onset potentials were -205 ± 20 mV relative to $E^{o'}(O_2/H_2O)$, the photocurrent densities were 22.9 ± 1.6 mA cm^{-2} at $E^{o'}(O_2/H_2O)$, and the solar-to-O_2(g) IRC was 1.42 ± 0.20%. The J-E behavior of the p^+-Si/$SiO_{x,RCA}$/Co_3O_4 dark electrode provides a measurement of the performance characteristics of the Co_3O_4 layer for the electrocatalysis of O_2(g) production in 1.0 M KOH(aq). A load-line analysis[31] indicated that a photodiode with an open-circuit voltage (V_{oc}) of 575 ± 20 mV, a short-circuit photocurrent density (Jsc) of 30.2 ±

1.1 mA cm^{-2}, a fill factor of 0.60 ± 0.01, and a photovoltaic efficiency of 11.1 ± 0.5 % would be required for a photodiode connected in series with a dark p^+-Si/$SiO_{x,RCA}$/Co_3O_4 anode to exhibit the electrochemical characteristics observed for the n-Si/$SiO_{x,RCA}$/Co_3O_4 photoanode.

Figure 3.5C shows the mass of O_2(g) generated as a function of time, as determined using an eudiometer, for an n-Si/$SiO_{x,RCA}$/Co_3O_4 photoanode in contact with 1.0 M KOH(aq). The photoanode was biased to maintain a constant current density of 6.7 mA cm^{-2}, and was illuminated by 100 mW cm^{-2} of AM 1.5G simulated solar illumination. The required bias was 1.6 V and did not change during the 24 h experiment (Figure 3.6). The mass of O_2(g) that would be produced as a function of time assuming 100% Faradaic efficiency for the oxidation of water to O_2(g) is included as a red curve in Figure 3.5C. The measured mass of O_2(g) was within experimental error of the calculated value, indicating that the n-Si/$SiO_{x,RCA}$/Co_3O_4 photoanodes exhibited essentially 100% Faradaic efficiency for the production of O_2(g) production under these conditions.

Figure 3.5B shows the photocurrent density as a function of time for an n-Si/$SiO_{x,RCA}$/Co_3O_4 photoanode in contact 1.0 M KOH(aq) while biased at 1.63 V versus RHE and under 1.1 Sun of ENH-type tungsten-halogen simulated solar illumination. The photocurrent density at 1.63 V versus RHE decreased by ~ 14% after more than 100 days (~2500 h) of continuous operation in 1.0 M KOH(aq), at which point the experiment was terminated but failure of the electrode was not apparent (see Appendix A.8 discussions about stability test). For comparison, the n-Si/$SiO_{x,RCA}$ interface without the Co_3O_4 overlayer showed rapid surface oxidation(Figure 3.7A). Figure 3.5C shows the J-E behavior of the photoelectrode as measured periodically during a 100-day stability test. The photocurrent-onset potential relative to $E^{o'}(O_2/H_2O)$ increased from -220 mV to -215 mV, -209 mV, -205 mV, and -202 mV, the photocurrent density at $E^{o'}(O_2/H_2O)$ decreased from 23.2 mA cm^{-2} to 22.1 mA cm^{-2}, 20.9 mA cm^{-2}, 18.7 mA cm^{-2}, and 17.7 mA cm^{-2}, the photocurrent density at 1.63 V versus RHE decreased from 30.4 mA cm^{-2} to 29.7 mA cm^{-2}, 29.2 mA cm^{-2}, 27.8 mA cm^{-2}, and 26.8 mA cm^{-2} and the solar-to-O_2(g) IRC decreased from 1.47% to 1.40%, 1.27%, 1.15% and 1.05% after 400 h, 800 h, 1600 h and 2400 h, respectively. The decay of the performance might be due to the dissolution of the Co_3O_4 layer, formation of pinholes at the electrode surface (Figure 3.3B), and the consequent generation of SiO_x islands at the pinholes. The average decay rates of the photocurrent-onset potential relative to $E^{o'}(O_2/H_2O)$, the photocurrent density at $E^{o'}(O_2/H_2O)$, and the solar-to-O_2(g) IRC for the n-Si/$SiO_{x,RCA}$/Co_3O_4 photoanode were 7.5 mV, 2.3 mA cm^{-2} and 0.17% per 1000 h, respectively. They were significantly lower than those for the n-Si/$SiO_{x,RCA}$/Co_3O_4/NiO_x

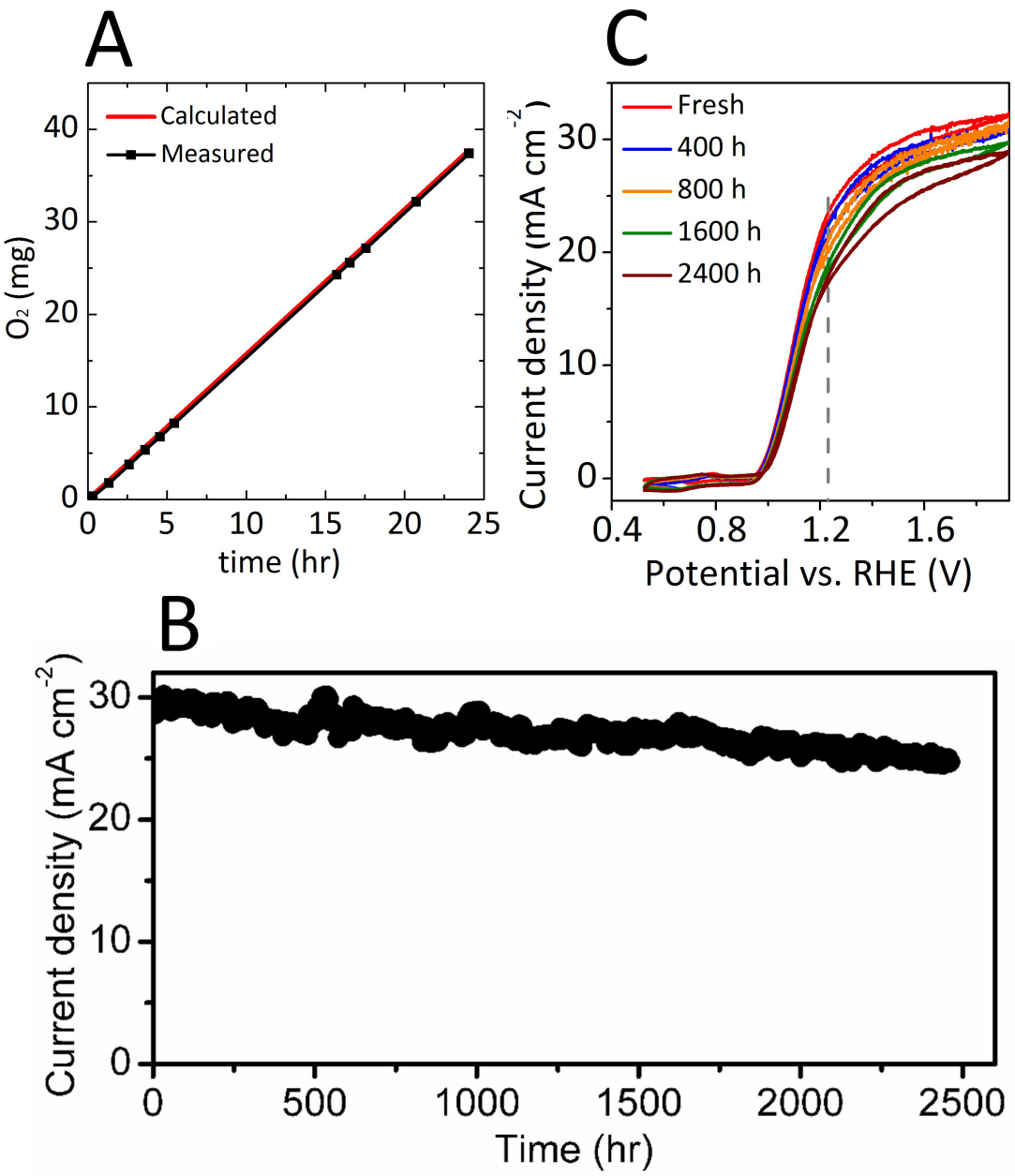

Figure 3.5: (A) O_2(g) production measured for an n-Si/$SiO_{x,RCA}$/Co_3O_4 photoanode held at a constant current of 6.7 mA cm^{-2} for 24 h while under AM 1.5G simulated illumination and in contact with 1.0 M KOH(aq), and O_2(g) production calculated based on the charge passed assuming 100% Faradaic efficiency (red line). (B) Chronoamperometry of an n-Si/$SiO_{x,RCA}$/Co_3O_4 photoanode held at 1.63 V vs RHE while under 1.1 Sun of simulated solar illumination and in contact with 1.0 M KOH(aq). (C) J-E behavior of the n-Si/$SiO_{x,RCA}$/Co_3O_4 photoanode as measured periodically during the chronoamperometric stability test shown in (B).

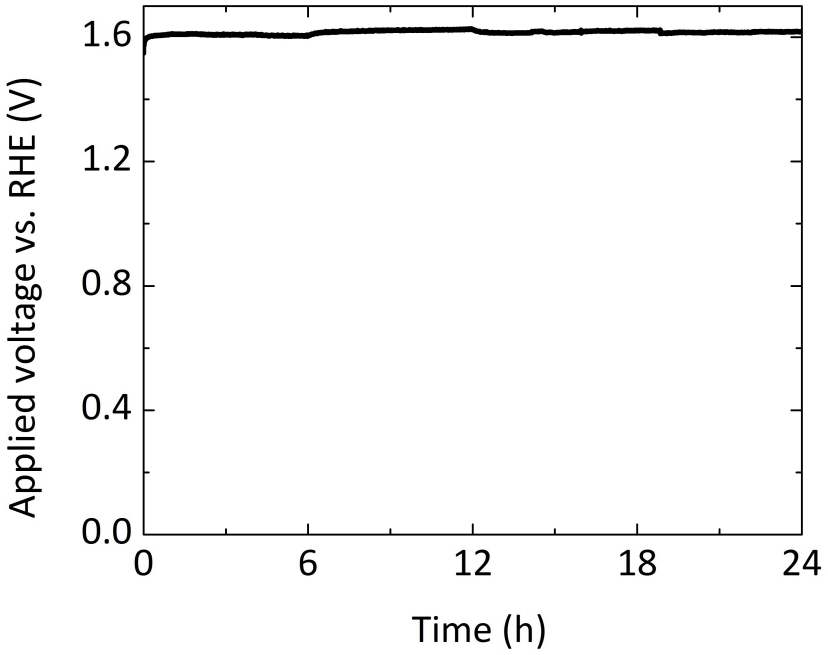

Figure 3.6: The voltage required to maintain 6.7 mA cm^{-2} of current density as a function of time for an n-Si/$SiO_{x,RCA}$/Co_3O_4 photoanode in contact with 1.0 M KOH(aq) and under 1 Sun of simulated 1.5 G solar illumination.

photoanode, which were 36 mV, 7.8 mA cm^{-2} and 0.97% per 1000 h. respectively[29].

The uniform and compact nature of the ALD Co_3O_4 film may explain the extended stability (~2500 h) and reduced performance decay rate of these devices in 1.0 M KOH(aq) because the compactness of the film may inhibit the formation of porous CoOOH at the grain boundaries, allowing effective isolation of the Si substrate from contact with the corrosive electrolyte. However, XPS spectra (Figure 3.8) showed the formation of CoOOH at the electrode surface, which could function as an OER catalyst[34].

Figure 3.9A shows the differential capacitance vs potential (Mott-Schottky) data for an n-Si/$SiO_{x,RCA}$/Co_3O_4 photoanode in contact with an aqueous solution that contained the electrochemically reversible, one-electron $Fe(CN)_6^{3-/4-}$ redox couple. The flat-band potential, Efb, calculated from the x intercept of the linear region of the data, was -0.85 ± 0.02 V versus E($Fe(CN)_6^{3-/4-}$) (see Appendix A.2, A.3), similar to the -0.83 ± 0.02 V versus E($Fe(CN)_6^{3-/4-}$) flat-band potential reported previously for n-Si/$SiO_{x,RCA}$ substrates coated with a thin layer of ALD Co_3O_4 as well as with a 100 nm layer of sputtered nickel oxide[29]. The flat-band potential of the n-Si/$SiO_{x,RCA}$/Co_3O_4 photoanodes is consistent with the presence of significant band bending and therefore with the presence

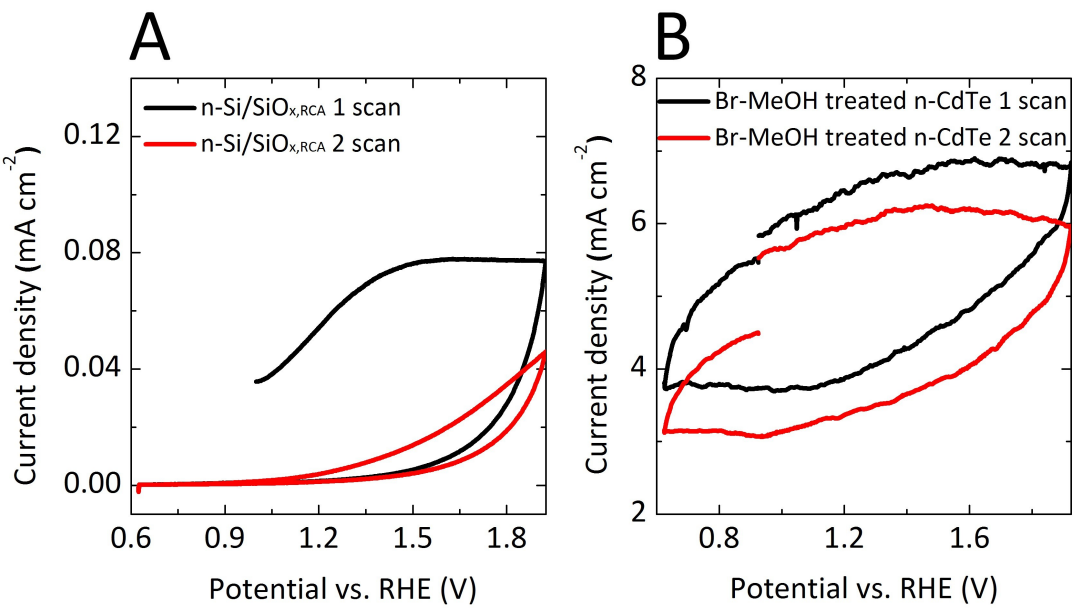

Figure 3.7: J-E data for etched n-Si/$SiO_{x,RCA}$ (A) and n-CdTe (B) photoelectrodes, without a Co_3O_4 coating. Measurements were performed in 1.0 M KOH(aq) under 1 Sun of simulated illumination.

of a large electric field in the space-charge region, which enables efficient separation of photogenerated charge carriers.

The properties of the n-Si/$SiO_{x,RCA}$/Co_3O_4 junction were evaluated further using non-aqueous electrochemical measurements. Figure 3.9B compares the photocurrent-onset potentials measured versus the Nernstian potential of the solution for n-Si/$SiO_{x,RCA}$/Co_3O_4 photoanodes under 100 mW cm^{-2} of simulated solar illumination and in contact with CH_3CN solutions that contained the one-electron redox couples cobaltocenium/cobaltocene ($Co(Cp)_2^{+/0}$), decamethylferrocenium/ferrocene ($Me_{10}Cp_2Fe^{+/0}$), and ferrocenium/ferrocene ($Fe(Cp)_2^{+/0}$), respectively. The n-Si/$SiO_{x,RCA}$/Co_3O_4 photoelectrodes exhibited photocurrent-onset potentials of -503 mV, 571 mV, and -563 mV relative to the Nernstian potential of the solution when in contact with $Co(Cp)_2^{+/0}$, $Me_{10}Cp_2Fe^{+/0}$, and $Fe(Cp)_2^{+/0}$, respectively. The variation in photocurrent-onset potentials observed for n-Si/$SiO_{x,RCA}$/Co_3O_4 photoelectrodes was negligible in comparison to the 1.524 V range over which the potential of the contacting solution was varied (0.951 V for $Co(Cp)_2^{+/0}$, -0.121 V for $Me_{10}Cp_2Fe^{+/0}$, and 0.573 V for $Fe(Cp)_2^{+/0}$ versus SCE), indicating that the junction is almost completely buried and therefore unaffected by the Nernstian potential of the solution. These results are consistent with the presence of a compact Co_3O_4 film with few defects that minimize contact between the underlying Si and the solution. In contrast, n-Si/$SiO_{x,RCA}$ substrates

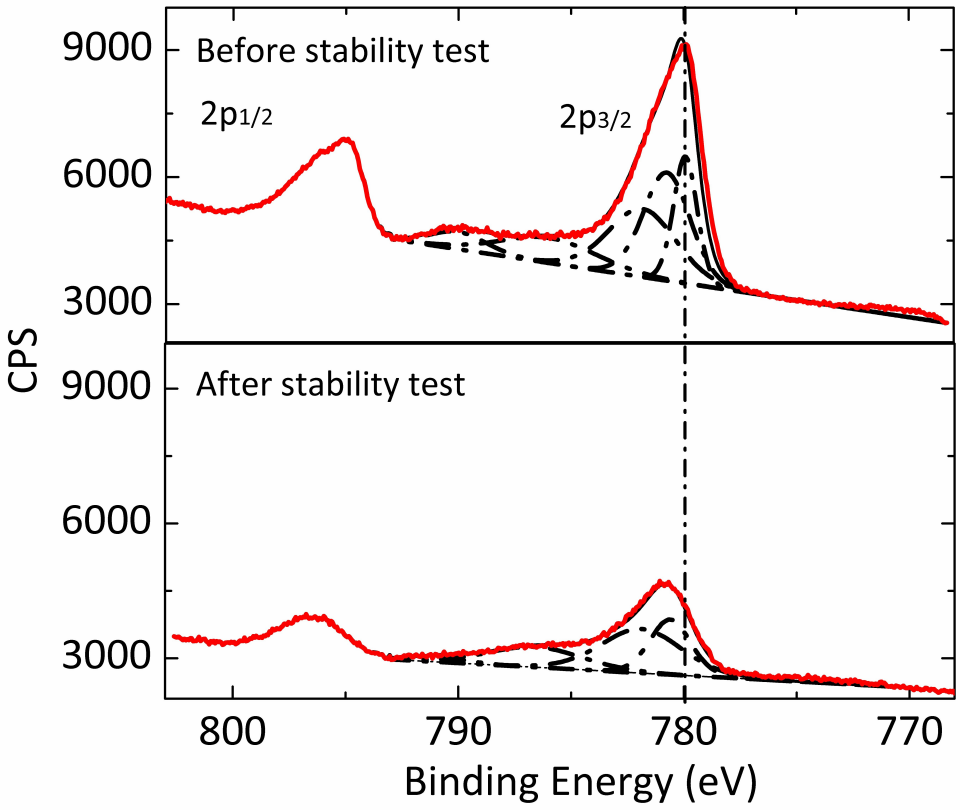

Figure 3.8: X-ray photoelectron spectroscopic (XPS) data for the n-Si/$SiO_{x,RCA}$/Co_3O_4 photoanode before and after the PEC stability test biased at 1.63 V vs RHE under 1.1 Sun of simulated solar illumination in contact with 1.0 M KOH(aq). The binding energies used for fitting of the Co $2p_{3/2}$ peaks were 779.9 eV, 780.7 eV, 781.8 eV, 786.0 eV, 790.0 eV (before stability test), and 780.6 eV, 781.9 eV,786.6 eV, 790.8 eV (after stability test). Peak fitting of the XPS spectra before the stability test in the Co $2p_{3/2}$ region and grazing incidence X-ray diffractometry (GIXRD) in previous work showed the existence of Co_3O_4 [29, 32, 33]. The shift of the Co 2p core level emission to higher binding energy indicated the transformation from Co_3O_4 to CoOOH [19].

coated with 2-3 nm of ALD Co_3O_4 exhibited photocurrent-onset potentials that varied by 510 mV in contact with these same redox species. Additionally, n-Si/$SiO_{x,RCA}$ substrates coated with ~100 nm columnar films of sputtered nickel oxide exhibited photocurrent-onset potentials that ranged over 225 mV in contact with the same set of redox couples (Figure 3.10). These results suggest that 50 nm thick ALD Co_3O_4 films exhibit fewer pinhole-type defects, which allow contact between the underlying Si and the electrolyte, than are exhibited by sputtered NiO_x films, which in turn exhibit fewer through-film defects than thin ALD Co_3O_4 films.

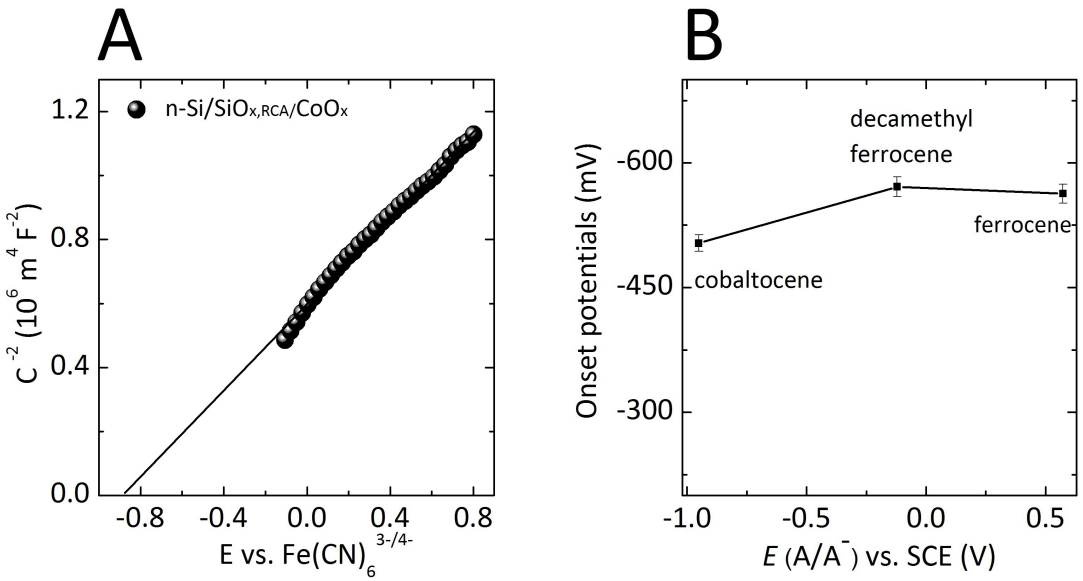

Figure 3.9: (A) Mott-Schottky plots of the inverse of the differential capacitance (C) of the electrode versus potential for an n-Si/$SiO_{x,RCA}$/Co_3O_4 photoanode in contact with a solution of 50 mM $K_3Fe(CN)_6$, 350 mM $K_4Fe(CN)_6$, and 1.0 M KCl aqueous $Fe(CN)_6^{3-/4-}$ (B) Photocurrent-onset potentials versus the Nernstian potential of the solution for n-Si/$SiO_{x,RCA}$/Co_3O_4 photoanodes under 100 mW cm^{-2} illumination and in contact with CH_3CN solutions containing the cobaltocenium/ cobaltocene, decamethylferrocenium/ decamethylferrocene, and ferrocenium/ ferrocene redox couples, respectively. The line only connects the experimentally observed values; no functional form is assumed

The compact ALD Co_3O_4 layer required an overpotential of 433 mV to drive the OER on p^+-Si at a rate corresponding to a current density of 10 mA cm^{-2} under these conditions. For comparison, under the same conditions, sputtered columnar NiO_x films on p^+-Si require a 330 mV overpotential to produce a current density of 10 mA cm^{-2} [17]. Compared to the n-Si/sputtered catalyst interface, the n-Si/ALD catalyst interface was free of detrimental effects produced by the oxygen plasma during the sputtering process, and was conformal and compact. Assuming that the interface characteristics do not depend on the doping of the substrate, the electrochemical behavior of the p^+-Si anodes can be compared to the photoelectrochemial behavior of the n-Si photoanodes, indicating that the n-Si/$SiO_{x,RCA}$/Co_3O_4 exhibited both a higher photovoltage and a higher overpotential, by 165 and 103 mV, respectively, relative to n-Si photoanodes protected by a columnar NO_x film. Hence, although an n-Si photoanode with a ALD Co_3O_4 layer exhibited higher solar-to-O2 conversion efficiency than an n-Si/$SiO_{x,RCA}$/NiO_x photoanode[29], the interfacial energetics control of the photovoltage provided by n-Si/$SiO_{x,RCA}$/Co_3O_4 heterojunctions,

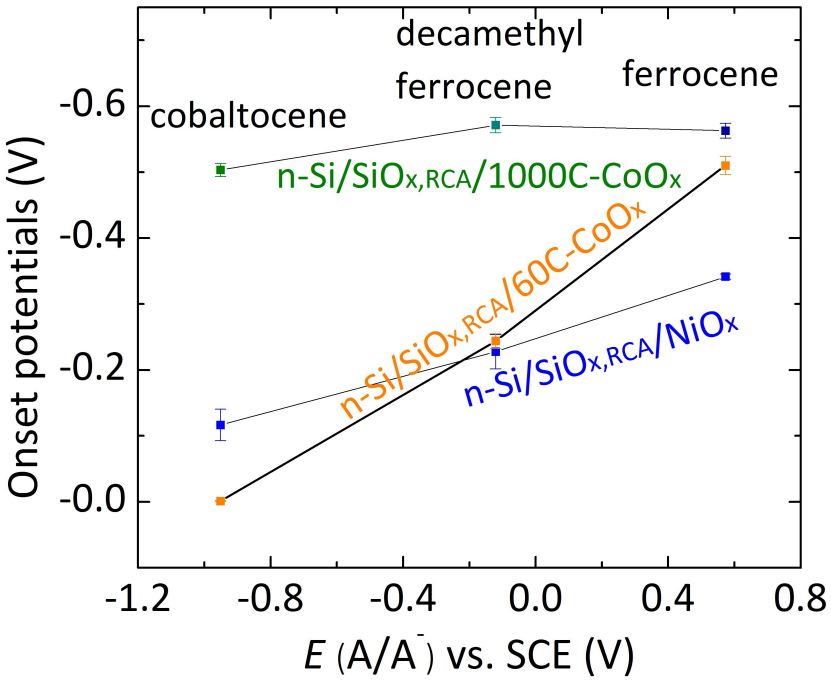

Figure 3.10: Photocurrent-onset potentials versus the Nernstian potential of the solution for n-Si/$SiO_{x,RCA}$/60C−Co_3O_4 (60 ALD cycles, 2 ∼ 3 nm thick Co_3O_4) (orange), n-Si/$SiO_{x,RCA}$/1000C−Co_3O_4 (1000 ALD cycles, ∼ 50 nm thick Co_3O_4) (green) and n-Si/$SiO_{x,RCA}$/NiO_x (∼100 nm thick sputtered NiO_x) (blue) photoelectrodes under 100W cm^{-2} illumination in cobaltocene, decamethyl ferrocene, and ferrocene redox systems, respectively. The data indicate the change in the observed photovoltage as the redox potential of the solution was varied. Lines only connect the experimentally observed values; no functional form is assumed.

in combination with the active OER electrocatalysis and protection provided by the NiO_x overlayer, provides a superior combination of properties for a Si heterojunction photoanode effecting water oxidation in alkaline electrolytes.

Prior work involving atomic-layer deposition of Co_3O_4 films (∼4-5 nm thick) onto planar np^+-Si substrates concluded that i) such devices are characterized by significant corrosion and a decline in J-E response after 30 min of operation in contact with 1.0 M NaOH(aq) while biased at 1.6 V versus RHE and under 1 Sun illumination; and ii) that nanoscale texturing the surface of the substrate prior to deposition of the Co_3O_4 film improved both the performance and the stability of devices[19]. For comparison, a Co_3O_4 film was deposited herein onto a planar n-Si/$SiO_{x,RCA}$ photoanode using 100 ALD cycles (n-Si/$SiO_{x,RCA}$/100C−Co_3O_4, Co_3O_4 film 4 ∼ 5 nm thick). When operated in contact with 1.0 M KOH(aq) under 1 Sun of simulated illumination, the

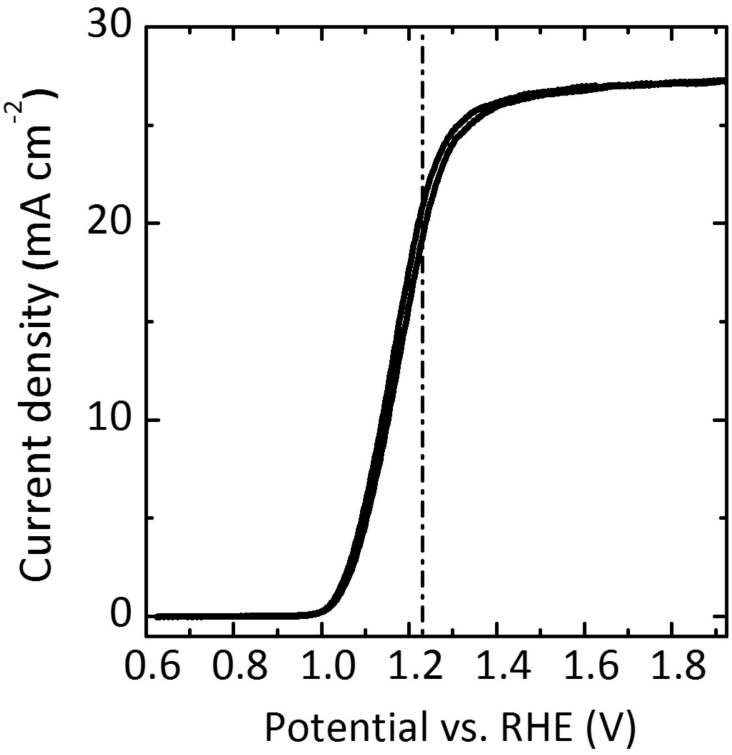

Figure 3.11: Representative J-E behavior of planar n-Si/$SiO_{x,RCA}$/100C$-Co_3O_4$ photoanodes with 100 ALD cycles of Co_3O_4 in 1.0 M KOH(aq) under 1 Sun simulated illumination.

n-Si/$SiO_{x,RCA}$/100C$-Co_3O_4$ device yielded a photocurrent density of 20.0 mA cm^{-2} at $E^{o'}(O_2/H_2O)$ and a light-limited current density of 27.3 mA cm^{-2} (Figure 3.11). The performance of the n-Si/$SiO_{x,RCA}$/100C$-Co_3O_4$ compared favorably to that reported for the planar and nanotextured np^+-Si/Co_3O_4 photoanodes, which exhibited photocurrent densities of 12 mA cm^{-2} and 17 mA cm^{-2} at $E^{o'}(O_2/H_2O)$ and saturation current densities of 27 mA cm^{-2} and 30 mA cm^{-2} under the same conditions, respectively[19]. An n-Si/$SiO_{x,RCA}$ substrate was additionally coated with a thinner layer of Co_3O_4 (~2-3 nm thick) that was deposited using 60 ALD cycles (n-Si/$SiO_{x,RCA}$/60C$-Co_3O_4$). Figure 3.12B shows the initial J-E behavior of the n-Si/$SiO_{x,RCA}$/60C$-Co_3O_4$, as well as the behavior after the one-hour stability test. No significant corrosion nor decline in J-E response was observed, in contrast to prior work on planar np^+-Si/60C$-Co_3O_4$ devices, which exhibited a decay in performance after 30 min of operation under similar conditions[19].

Several factors may contribute to the improved performance and stability observed in this

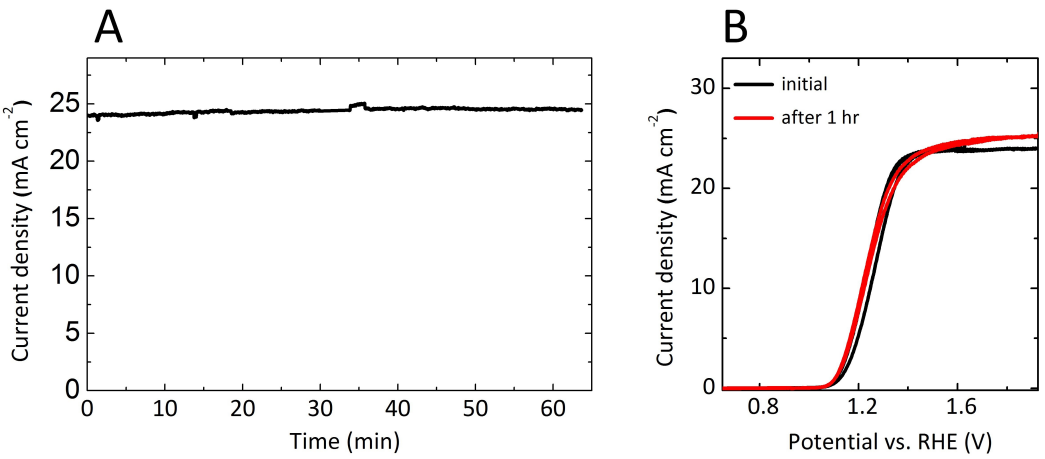

Figure 3.12: (A) Chronoamperometry curve of n-Si/$SiO_{x,RCA}$/Co_3O_4 (60 ALD cycles for Co_3O_4) photoanode biased at 1.63 V vs RHE under 1 Sun of simulated 1.5G solar illumination from an ENH-type tungsten-halogen lamp. (B) J-E data for planar n-Si/$SiO_{x,RCA}$/Co_3O_4 (60 ALD cycles for Co_3O_4) in contact with 1.0 M KOH(aq) under 100 mW cm^{-2} of simulated 1.5 G solar illumination collected before and after the stability test shown in (A).

work for n-Si/$SiO_{x,RCA}$ substrates coated by ALD Co_3O_4 as compared to prior observations of the behavior of np$^+$-Si homojunctions coated by ALD Co_3O_4. The n-Si/$SiO_{x,RCA}$/Co_3O_4 heterojunctions exhibit improved spectral response in the short-wavelength region of the solar spectrum (< 500 nm) relative to devices with np$^+$-Si homojunctions, because the heterojunctions do not suffer from the parasitic absorption inherent to a p$^+$-Si emitter layer. In addition, several differences in the methods for ALD of the Co_3O_4 layer may be important contributors to the differences in observations, particularly with respect to the initiation and adhesion of the ALD film, the uniformity of the resulting Co_3O_4 layer, and the nature of the SiO_x layer at the interface. These factors may include i) different oxidants (ozone versus oxygen plasma); ii) different deposition temperatures (150 °C versus 300 °C); and, iii) different preparation of substrates prior to ALD (RCA cleaning leaves a thin SiO_x layer on the surface, relative to HF etching which leaves a hydride-terminated Si surface). In combination with the previously reported behavior of n-Si/$SiO_{x,RCA}$/Co_3O_4/NiO_x photoanodes, the present work clearly demonstrates that ALD-deposited Co_3O_4 films are capable of providing a basis for high photovoltage, stablilized photoanodes on a variety of Si substrates.

We investigated whether the 50 nm ALD Co_3O_4 films could be extended readily to produce stable, high-performance heterojunctions with other semiconductors that could

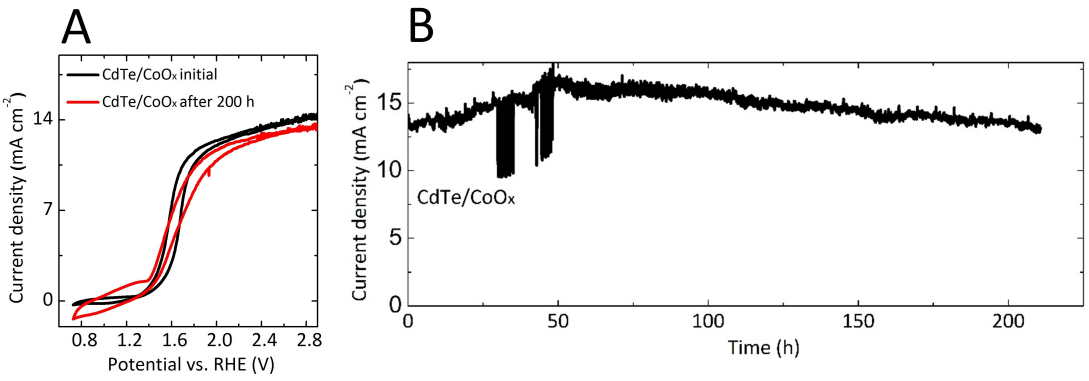

Figure 3.13: (A) J-E data for an n-CdTe/1000C-Co_3O_4 (1000 ALD cycles) photoanode in 1.0 M KOH(aq) under 1 Sun of simulated 1.5G solar illumination before and after 200 h of continuous operation at 2.8 V vs. RHE. (B) Chronoamperometry of n-CdTe/1000C-Co_3O_4 photoanode biased at 2.8 V vs. RHE under 1 Sun of simulated 1.5G solar illumination in contact with 1.0 M KOH(aq).

produce self-passivating oxides under anodic conditions, specifically n-CdTe. The n-CdTe/Co_3O_4 photoanode exhibited photocurrent-onset potential of ~+220 mV relative to $E^{o'}(O_2/H_2O)$, and light-limited current density of ~14 mA cm^{-2}, but produced no light-induced current at $E^{o'}(O_2/H_2O)$ in 1.0 M KOH(aq) under 1 Sun of simulated solar illumination. The poor performance of n-CdTe/Co_3O_4 might be due to the lattice mismatch or band structure misalignment between n-CdTe and Co_3O_4 layer, or the lack of an appropriate passivation layer, like the silicon oxide layer for n-Si, and the ozone for the ALD process would likely result in detrimental effects to the n-CdTe and Co_3O_4 interfaces. Although the n-CdTe/Co_3O_4 devices exhibited increased stability under oxygen-evolution conditions (Figure 3.13), further improvement is needed. For example, the current density from the n-CdTe/Co_3O_4 device operated in contact with 1.0 M KOH (aq) and biased to 2.8 V versus RHE while under 1 Sun of simulated solar illumination decreased by ~10% over a 200 h test period, whereas n-CdTe photoanodes that did not have Co_3O_4 protection layer showed rapid surface oxidation, as expected (Figure 3.7B).

3.4 Conclusions

In conclusion, stable and efficient photoanodes for the oxidation of water to O_2(g) in alkaline aqueous electrolytes can be constructed using heterojunctions between planar n-Si(100) substrates bearing a thin chemically grown oxide layer and a 50 nm thick ALD Co_3O_4 film. The Si/$SiO_{x,RCA}$/Co_3O_4 heterojunction simplifies the processing required to produce high-performance stable Si photoanodes by eliminating the need for homogeneous

buried np^+ junctions, nanotexturing, or intermediate interfacial engineering layers. The Co_3O_4 film provides multiple desired functions for fully integrated solar-fuels devices, including a high-energy barrier for charge separation, catalytic activity for the water-oxidation reaction, chemical stability, and structural compactness to enable the long-term operation of Si photoanodes.

References

[1] J. A. Turner. "Sustainable Hydrogen Production". In: *Science* 305 (2004), pp. 972–974.

[2] K. Maeda et al. "Photocatalyst Releasing Hydrogen from Water". In: *Nature* 440.7082 (2006), p. 295.

[3] M. J. Kenney et al. "High-Performance Silicon Photoanodes Passivated with Ultrathin Nickel Films for Water Oxidation". In: *Science* 342.6160 (2013), pp. 836–40.

[4] N. S. Lewis and D. G. Nocera. "Powering the Planet: Chemical Challenges in Solar Energy Utilization". In: *Proc. Natl. Acad. Sci. U.S.A.* 103.43 (2006), pp. 15729–15735.

[5] E. A. Hernandez-Pagan et al. "Resistance and Polarization Losses in Aqueous Buffer-Membrane Electrolytes for Water-splitting Photoelectrochemical Cells". In: *Energy Environ. Sci.* 5.6 (2012), pp. 7582–7589.

[6] J. Jin et al. "An Experimental and Modeling/Simulation-based Evaluation of the Efficiency and Operational Performance Characteristics of an Integrated Membrane-free, Neutral pH Solar-driven Water-splitting System". In: *Energy Environ. Sci.* 7 (2014), pp. 3371–3380.

[7] S. Haussener et al. "Modeling, Simulation, and Design Criteria for Photoelectrochemical Water-splitting Systems". In: *Energy Environ. Sci.* 5.12 (2012), pp. 9922–9935.

[8] J. R. McKone, N. S. Lewis, and H. B. Gray. "Will Solar-Driven Water-Splitting Devices See the Light of Day?" In: *Chem. Mater.* 26.1 (2014), pp. 407–414.

[9] K. Sun et al. "Enabling Silicon for Solar-Fuel Production". In: *Chem. Rev.* 114.17 (2014), pp. 8662–8719.

[10] S. Hu et al. "Thin Film Materials for the Protection of Semiconducting Photoelectrodes in Solar-Fuels Generators". In: *J. Phys. Chem. C* 119.43 (2015), pp. 24201–24228.

[11] S. Hu et al. "Amorphous TiO(2) Coatings Stabilize Si, GaAs, and GaP Photoanodes for Efficient Water Oxidation". In: *Science* 344.6187 (2014), pp. 1005–9.

[12] M. F. Lichterman et al. “Stabilization of n-Cadmium Telluride Photoanodes for Water Oxidation to O2(g) in Aqueous Alkaline Electrolytes using Amorphous TiO2 Films Formed by Atomic-layer Deposition”. In: *Energy Environ. Sci.* 7.10 (2014), pp. 3334–3337.

[13] M. R. Shaner et al. “Stabilization of Si Microwire Arrays for Solar-Driven H2O Oxidation to O2(g) in 1.0 M KOH(aq) Using Conformal Coatings of Amorphous TiO2”. In: *Energy Environ. Sci.* 8.1 (2015), pp. 203–207.

[14] M. T. McDowell et al. “The Influence of Structure and Processing on the Behavior of TiO2 Protective Layers for Stabilization of n-Si/TiO2/Ni Photoanodes for Water Oxidation”. In: *ACS Appl. Mater. Inter.* 7.28 (2015), pp. 15189–99.

[15] Y. W. Chen et al. “Atomic Layer-Deposited Tunnel Oxide Stabilizes Silicon Photoanodes for Water Oxidation”. In: *Nat. Mater.* 10.7 (2011), pp. 539–44.

[16] B. Mei et al. “Crystalline TiO2: A Generic and Effective Electron-Conducting Protection Layer for Photoanodes and -cathodes”. In: *J. Phys. Chem. C* 119.27 (2015), pp. 15019–15027.

[17] K. Sun et al. “Stable Solar-Driven Oxidation of Water by Semiconducting Photoanodes Protected by Transparent Catalytic Nickel Oxide Films”. In: *Proc. Natl. Acad. Sci. U.S.A.* 112 (2015), pp. 3612–3617.

[18] K. Sun et al. “Sputtered NiOx Films for Stabilization of p+n-InP Photoanodes for Solar-Driven Water Oxidation”. In: *Adv. Energy Mater.* (2015), p. 1402276.

[19] J. Yang et al. “Efficient and Sustained Photoelectrochemical Water Oxidation by Cobalt Oxide/silicon Photoanodes with Nanotextured Interfaces”. In: *J. Am. Chem. Soc.* 136.17 (2014), pp. 6191–4.

[20] L. Chen et al. “p-Type Transparent Conducting Oxide/n-Type Semiconductor Heterojunctions for Efficient and Stable Solar Water Oxidation”. In: *J. Am. Chem. Soc.* 137.30 (2015), pp. 9595–603.

[21] K. Sun et al. “Stable Solar-Driven Water Oxidation to O2(g) by Ni-oxide Coated Silicon Photoanodes”. In: *J. Phys. Chem. Lett.* 6 (2015), pp. 592–598.

[22] N. C. Strandwitz et al. “Photoelectrochemical Behavior of n-type Si(100) Electrodes Coated with Thin Films of Manganese Oxide Grown by Atomic Layer Deposition”. In: *J. Phys. Chem. C* 117.10 (2013), pp. 4931–4936.

[23] H. Gerischer. “Stability of Semiconductor Electrodes against Photodecomposition”. In: *J. Electroanal. Chem.* 82.1-2 (1977), pp. 133–143.

[24] E. Verlage et al. “A Monolithically Integrated, Intrinsically Safe, 10% Efficient, Solar-Driven Water-Splitting System Based on Active, Stable Earth-Abundant Electrocatalysts in Conjunction with Tandem III-V Light Absorbers Protected by Amorphous TiO2 Films”. In: *Energy Environ. Sci.* 8.11 (2015), pp. 3166–3172.

[25] A. Heller. In: *Photoeffects at Semiconductor-Electrolyte Interfaces*. Vol. 146. ACS Symposium Series. Washington, D.C.: American Chemical Society, 1981. Chap. 4, pp. 57–77.

[26] G. Grube and O. Feucht. "Behaviour of Cobalt Anodes in Alkaline Solutions". In: *Z. Elektrochem.* 28 (1922), pp. 568–579.

[27] H. Willems et al. "The Oxygen Evolution Reaction on Cobalt .1. Reaction Order Experiments and Impedance Measurements". In: *J. Electroanal. Chem.* 170.1-2 (1984), pp. 227–242.

[28] M. F. Lichterman et al. "Enhanced Stability and Activity for Water Oxidation in Alkaline Media with Bismuth Vanadate Photoelectrodes Modified with a Cobalt Oxide Catalytic Layer Produced by Atomic Layer Deposition". In: *J. Phys. Chem. Lett.* 4.23 (2013), pp. 4188–4191.

[29] X. Zhou et al. "Interface Engineering of the Photoelectrochemical Performance of Ni-oxide-coated n-Si Photoanodes by Atomic-Layer Deposition of Ultrathin Films of Cobalt Oxide". In: *Energy Environ. Sci.* 8.9 (2015), pp. 2644–2649.

[30] R. H. Coridan et al. "Methods for Comparing the Performance of Energy-Conversion Systems for Use in Solar Fuels and Solar Electricity Generation". In: *Energy Environ. Sci.* (2015).

[31] M. R. Shaner, K. T. Fountaine, and H.-J. Lewerenz. "Current-voltage Characteristics of Coupled Photodiode-Electrocatalyst Devices". In: *Appl. Phys. Lett.* 103.14 (2013).

[32] J. Yang et al. "Synthesis and Characterization of Cobalt Hydroxide, Cobalt Oxyhydroxide, and Cobalt Oxide Nanodiscs". In: *J. Phys. Chem. C* 114.1 (2010), pp. 111–119.

[33] M. C. Biesinger et al. "Resolving Surface Chemical States in XPS Analysis of First Row Transition Metals, Oxides and Hydroxides: Cr, Mn, Fe, Co and Ni". In: *Appl. Surf. Sci.* 257.7 (2011), pp. 2717–2730.

[34] J. C. Hill, A. T. Landers, and J. A. Switzer. "An Electrodeposited Inhomogeneous Metal-insulator-semiconductor Junction for Efficient Photoelectrochemical Water Oxidation". In: *Nat. Mater.* 14.11 (2015), pp. 1150–1155.

Chapter 4

SOLAR-DRIVEN REDUCTION OF 1 ATM CO_2 TO FORMATE AT 10% ENERGY-CONVERSION EFFICIENCY BY USE OF A TIO_2-PROTECTED III-V TANDEM PHOTOANODE IN CONJUNCTION WITH BIPOLAR MEMBRANE AND A PD/C CATHODE ELECTROCATALYST

[1]A solar-driven CO_2 reduction (CO_2R) cell was constructed, consisting of a tandem GaAs/InGaP/TiO_2/Ni photoanode in 1.0 M KOH(aq) (pH=13.7) to facilitate the oxygen-evolution reaction (OER), a Pd/C nanoparticle-coated Ti mesh cathode in 2.8 M $KHCO_3$(aq) (pH=8.0) to perform the CO_2R reaction, and a bipolar membrane to allow for steady-state operation of the catholyte and anolyte at different bulk pH values. At the operational current density of 8.5 mA cm^{-2}, in 2.8 M $KHCO_3$(aq), the cathode exhibited <100 mV overpotential and >94% Faradaic efficiency for the reduction of 1 atm of CO_2(g) to formate. The anode exhibited 320 ± 7 mV overpotential for the OER in 1.0 M KOH(aq), and the bipolar membrane exhibited ~480 mV voltage loss with minimal product crossovers and >90% and >95% selectivity for protons and hydroxide ions, respectively. The bipolar membrane facilitated coupling between two electrodes and electrolytes, one for the CO_2R reaction and one for the OER, that typically operate at mutually different pH values, and produced a lower total cell overvoltage than known single-electrolyte CO_2R systems, while exhibiting ~10% solar-to-fuels energy-conversion efficiency.

4.1 Introduction

The sustainable electrochemical reduction of CO_2 requires utilization of CO_2 from the atmosphere as well as use of the electrons and protons produced by the oxidation of water to O_2(g)[1]. However, the CO_2 reduction (CO_2R) reaction involves very different optimal electrolyte conditions than oxidation of water. For the cathodic CO_2R reaction, in alkaline conditions (e.g., pH>10) the low dissolved CO_2 concentration imposes severe mass-transport limitations on the electroactive reagent[2–4], whereas in acidic conditions (e.g., pH<1), the high proton concentration favors the competing hydrogen-evolution reaction (HER). Hence, the development of catalysts for the CO_2R reaction has generally focused on electrolytes having near-neutral pH values[5, 6]. At present, in near-neutral

[1]This chapter is adapted with permission from X. Zhou, R. Liu, K. Sun, Y. Chen, E. Verlage, S. A. Francis, N. S. Lewis, C. Xiang, ACS Energy Letters 2016, 1 (4), 764-770. Copyright 2016 American Chemical Society.

pH electrolytes, only electrochemical processes that involve the two-electron/two-proton reduction of CO_2, to produce either CO or formate, can be performed efficiently and selectively at an operating current density of 10^{1} mA cm^{-2}[5, 7–10]. In contrast, for the oxygen-evolution reaction (OER), mixed-metal oxides have been extensively studied in strongly alkaline conditions (1.0 M KOH(aq)), with state-of-the-art catalysts exhibiting ~250 – 300 mV overpotentials at 10 mA cm^{-2} of anodic current density[11, 12]. Electrocatalysts for the OER in near-neutral pH electrolytes exhibit substantially larger overpotentials than OER electrocatalysts in alkaline conditions[12–14], because the negatively charged hydroxide ion is more readily oxidized than a neutral water molecule and hydroxide is present in high concentration in alkaline solutions[15].

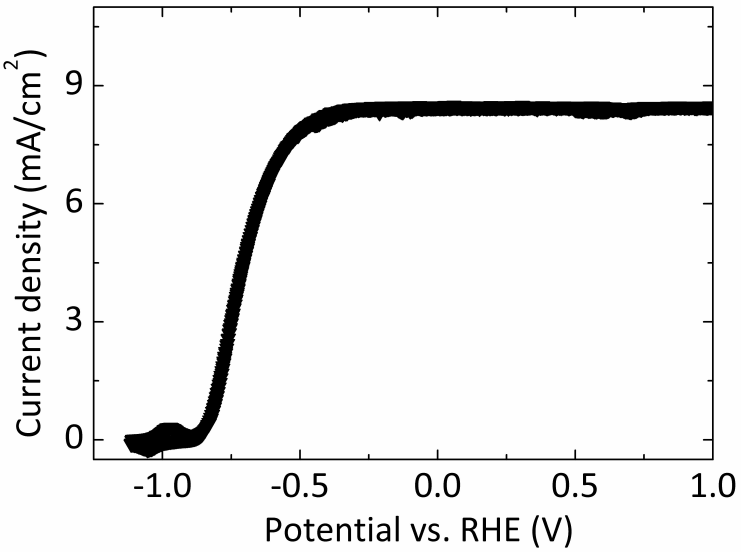

Figure 4.1: Cyclic voltammetry of GaAs/InGaP/TiO_2/Ni photoanode in 1.0 M KOH(aq) under 100 mW cm^{-2} of simulated AM1.5 illumination.[16]

Most laboratory demonstrations of solar-driven CO_2R devices have used a single electrolyte at near-neutral pH values, but consequently suffer substantial overpotential losses for the OER[8, 17–19]. For example, a 6.5% solar-to-fuel conversion efficiency, STF, was reported using a Au catalyst for CO generation in 0.5 M $NaHCO_3$(aq) electrolyte[8]. A value of STF = 4.6% was obtained using a polymeric Ru complex for formate generation in 0.1 M aqueous phosphate buffer[17]. In addition to requiring effective ionic coupling between the catholyte and anolyte, a full solar-driven CO_2R system also requires a robust means to separate the products as well as facile collection of the reduced fuels. We demonstrate herein the performance of a photovoltaic-assisted electrosynthetic cell

in which the photoanode is operated in 1.0 M KOH(aq) (pH=13.7) to perform the OER while the cathode performs the CO_2R reaction in 2.8 M $KHCO_3$(aq) (pH=8.0) under 1 atm CO_2 (g). The pH difference between the cathode chamber and the anode chamber was sustained at steady state with no accompanying chemical bias voltage by use of a bipolar membrane (fumasep FBM)[20–23]. Hence, two electrolytes having mutually different pH values, with each electrolyte individually optimized for the CO_2R reaction or the OER, were effectively coupled together to produce a modest combined cell overvoltage at the desired operational current density.

The photoanode (GaAs/InGaP/TiO_2/Ni) consisted of a tandem-junction III-V photoabsorber, an amorphous, hole-conductive TiO_2 protection layer, and a thin catalyst layer to facilitate the OER[16, 24]. The detailed fabrication method of the photoanode is described in Appendix B. The water oxidation behavior of the photoanode in 1.0 M KOH(aq) under simulated 1 sun illumination has been characterized previously[16], and the photoanode exhibited a light-limited photocurrent density of ~8.5 mA cm^{-2} and an equivalent open-circuit voltage of ~2.4 V, (Figure 4.1), in accord with prior results[16, 24].

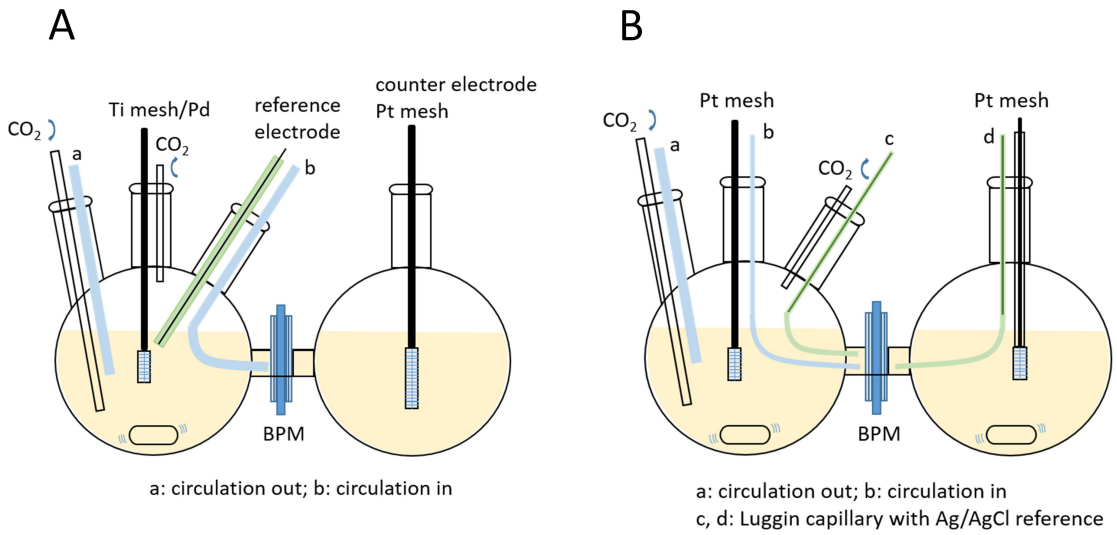

Figure 4.2: Schematic drawings showing the configuration for 3-electrode (A), electrochemical measurements and the 4-point measurement system for BPM measurements (B).

4.2 Results and Discussion

Figure 4.3A shows the cyclic voltammetry, at a scan rate of 10 mV s^{-1} without correction for uncompensated resistance (see Figure 4.2A for an illustration of the 3-electrode electrochemical measurement setup), of a Pd/C nanoparticle-coated Ti mesh cathode with

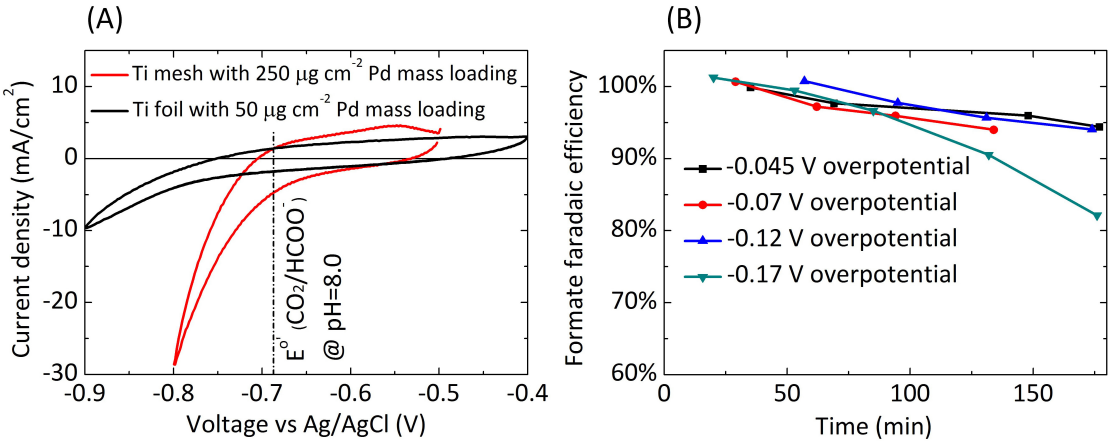

Figure 4.3: (A) Cyclic voltammetry of the Pd/C nanoparticle-coated stacked Ti mesh electrode with a Pd mass loading of 250 μg cm^{-2} (red) and the Pd/C nanoparticle-coated Ti foil with a Pd mass loading of 50 μg cm^{-2} (black) in CO_2-saturated 2.8 M $KHCO_3$(aq) at pH=8.0. The dotted line indicates the equilibrium potential for CO_2 reduction to formate at pH=8.0. The three-electrode cell configuration is shown in Figure 4.2A. (B) Faradaic efficiency of formate production as a function of time, for four different overpotentials, using the Pd/C nanoparticle-coated Ti mesh in CO_2-saturated 2.8 M $KHCO_3$(aq).

a Pd mass loading of 250 μg cm^{-2} (red), and a Pd/C coated Ti foil with a Pd mass loading of 50 μg cm^{-2} (black), respectively, in 2.8 M $KHCO_3$(aq) (pH=8) that was saturated with a stream of 1 atm CO_2 (g). The Pd/C cathode was fabricated by drop-casting a solution containing 2 mg mL^{-1} of Pd/C nanoparticles and ~0.15 wt% Nafion in isopropanol on a Ti mesh or a Ti foil. The Pd/C coated Ti foil (black curve in Figure 4.3A) exhibited very similar electrocatalytic activity to that reported previously[7]. The Pd/C coated stacked Ti mesh electrode exhibited improved performance because of the increased mass loading and larger electrochemically accessible surface area for CO_2R reduction. The forward scan indicated that the onset potential of cathodic current was close the equilibrium potential for CO_2 reduction to formate ($E°'(CO_2/HCOO^-)$) = -0.687 V versus the Ag/AgCl reference electrode)[25]. An overpotential of 57 ± 8 mV was required to drive the CO_2R reaction at a cathodic geometric current density of 10 mA cm^{-2}. Figure 4.3B shows the Faradaic efficiency for the production of formate using the Pd/C nanoparticle-coated Ti mesh cathode in CO_2-saturated 2.8 M $KHCO_3$(aq) as a function of time, at four different overpotentials. At all overpotentials, near-unity Faradaic efficiency was observed for the first 60 min of operation. The Faradaic efficiency then decreased slowly for overpotentials between -45 mV and -120 mV, but still exceeded $\geqslant$ 94% after 3 h of electrolysis (Figure 4.3B). In contrast, when the electrode was held at -170 mV vs $E°'(CO_2/HCOO^-)$, the Faradaic efficiency decayed quickly after 90 min, and decreased to ~80% after 3 h of

continuous operation (see Appendix A.9 for discussion about the time dependence of the Faradaic efficiency). The decrease of the Faradaic efficiency for formate production is consistent with the accumulation of CO at the surface of the Pd nanoparticles[7]. To characterize in detail the performance of the protection layer and electrocatalytic components of the anode, Figure 4.4C shows the current density vs potential (J-E) behavior of a p^+-Si/TiO_2/Ni dark anode effecting the OER in 1.0 M KOH(aq) (black) and in 2.8 M $KHCO_3$(aq) (red), respectively, without any correction for uncompensated resistance. The J-E behavior of p^+-Si/TiO_2/Ni dark electrode was used to provide a measure of the overpotentials of the OER catalyst in 1.0 M KOH(aq) and in 2.8 M $KHCO_3$(aq) (see Appendix A.10 for discussion of nickel catalyst). As shown in Figure 4.4C, an overpotential of 330 ± 10 mV was required to produce a current density of 10 mA cm^{-2} in 1.0 M KOH(aq), consistent with previous results[26]. In contrast, an overpotential of 793 ± 26 mV was required in 2.8 M $KHCO_3$(aq) to produce 10 mA cm^{-2} of current density.

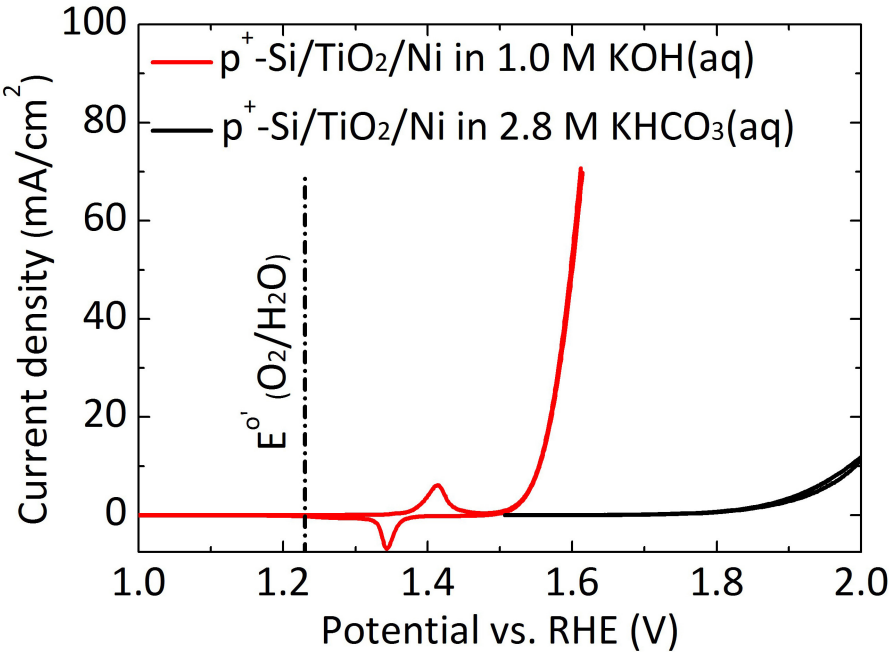

Figure 4.4: Current-voltage behavior of a p^+-Si/TiO_2/Ni electrode for the oxygen-evolution reaction (OER) in 1.0 M KOH(aq) (red) and in 2.8 M $KHCO_3$(aq) (black).

With the anolyte at pH = 13.7 (1.0 M KOH(aq)) and the catholyte at pH = 8.0 (2.8 M $KHCO_3$(aq), Figure 4.5A shows membrane voltage loss (left axis), as well as measured total membrane voltage (right axis) as a function of the current density normalized to the bipolar membrane (BPM) area (see Figure 4.2B for an illustration of the 4-point measurement configuration)[24]. Two Luggin capillaries with Ag/AgCl reference elec-

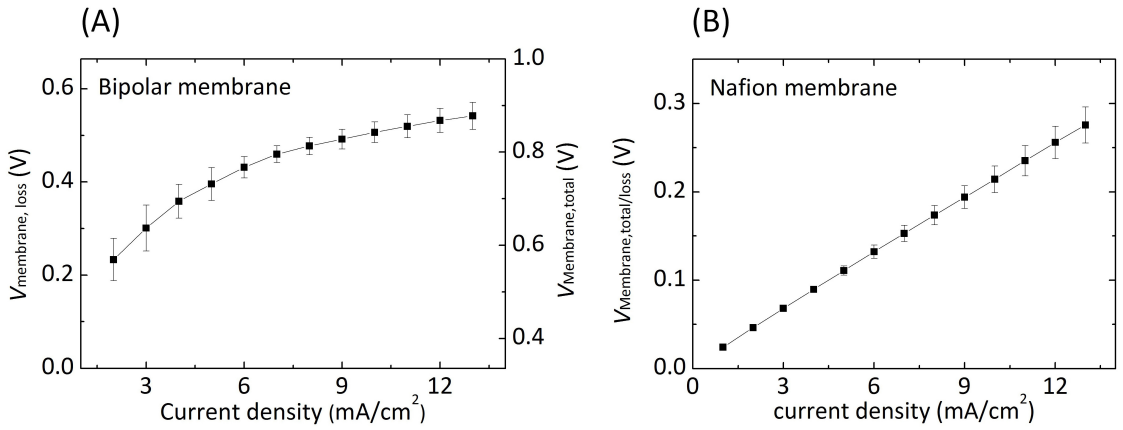

Figure 4.5: (A) Membrane voltage loss (left axis) and measured total membrane voltage (right axis) as a function of the current density normalized to the 0.03 cm^2 BPM area. The cell configuration was $KHCO_3$(aq) (pH=8.0)/BPM/KOH (aq, pH=13.7) (Figure 4.2B). (B) Measured total membrane voltage (or membrane voltage loss) as a function of the current density normalized to the Nafion area. The cell configuration was $KHCO_3$(aq) (pH=8.0)/Nafion/ $KHCO_3$(aq) (pH=8.0) (Figure 4.2B).

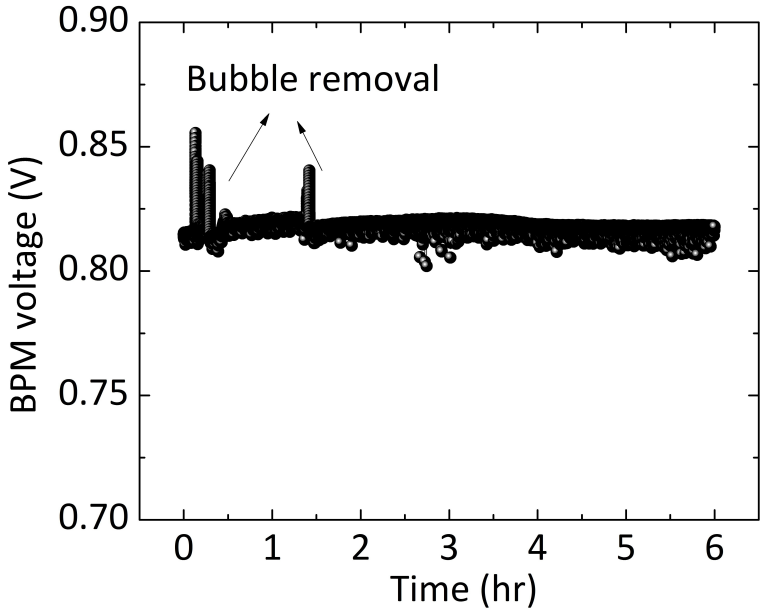

Figure 4.6: The bipolar membrane voltage as a function of time when the current density through the bipolar membrane was maintained at 8.5 mA cm^{-2}.

trodes were used to measure the electric potential drop across the bipolar membrane. A Luggin capillary is a small tube that can define a clear sensing point for reference elec-

trode. The equilibrium potential, $V_{membrane,equilibrium}$ was calculated to be 0.336 V in the anolyte/catholyte system. At a current density of 10 mA cm^{-2}, the measured membrane total voltage was 0.843 ± 0.038 V. Hence, to drive the CO_2 reduction to formate at steady state, the voltage loss in the BPM, $V_{membrane,loss} = V_{membrane,total} - V_{membrane,equilibrium}$ = 0.843 V – 0.059 V × (13.7 – 8.0), was 0.507 V. The voltage loss primarily resulted from the resistance loss of the bipolar membrane as well as from the overvoltage required for water dissociation at the transition region in the bipolar membrane. The observed membrane voltage losses in the 1.0 M KOH(aq) (pH=13.7)/2.8 M $KHCO_3$(aq) (pH=8.0) system were significantly smaller than those previously reported in 0.5 M KH_2BO_3(aq) (pH=9.3)/1.0 M H_2SO_4(aq) (pH=0)[24], because the flexible Luggin capillaries used in the present study were placed very close to the membrane and minimized the resistive losses due to the solution. To evaluate the ionic transport properties of the membrane, a cell with Pt mesh electrodes as the cathode and anode was operated continuously for 100 h at a current density of ~8.5 mA cm^{-2} normalized to the bipolar membrane area, with a resulting change by ~0.01 unit in the pH of the anolyte. If 100% of the charge passed were used for electrodialysis of the electrolytes, the pH of the anolyte would have changed by > 1 unit. After continuous operation of this cell for 6 h at 8.5 mA cm^{-2}, the bipolar membrane voltage changed by < 0.5% (Figure 4.6). Alternatively, for operation of CO_2R and OER in the same electrolyte, a cation exchange membrane, e.g., Nafion, could be used to separate the cathode chamber from the anode chamber. Figure 4.5B shows the measured total membrane voltage as a function of the current density normalized to the Nafion area, when both the anolyte and catholyte were 2.8 M $KHCO_3$(aq), but Nafion was used instead of a bipolar membrane. The total Nafion membrane voltage was equal to the Nafion membrane voltage loss, which largely arose due to the membrane resistance for transport of K^+ ions. At a current density of 10 mA cm^{-2}, the Nafion membrane voltage loss was 214 ± 15 mV.

The ion crossover fluxes in the BPM system were characterized using inductively coupled plasma mass spectrometry (ICPMS) in conjunction with a total inorganic carbon (TIC) analyser, to measure the ion concentrations in the catholyte and anolyte after charge was passed through the BPM at different current densities. At two different operational current densities, Figure 4.7A and 4.7B show the time-dependence of the selectivity for protons and hydroxide ions, respectively, through the bipolar membrane. Two major crossover pathways under the electric field, cation crossover from the anolyte to the catholyte, and anion crossover from the catholyte to the anolyte, were present due to the imperfect permselectivity of the cation-exchange membrane and anion-exchange membrane portions of the BPM. To determine the cation crossover, the $KHCO_3$(aq) catholyte

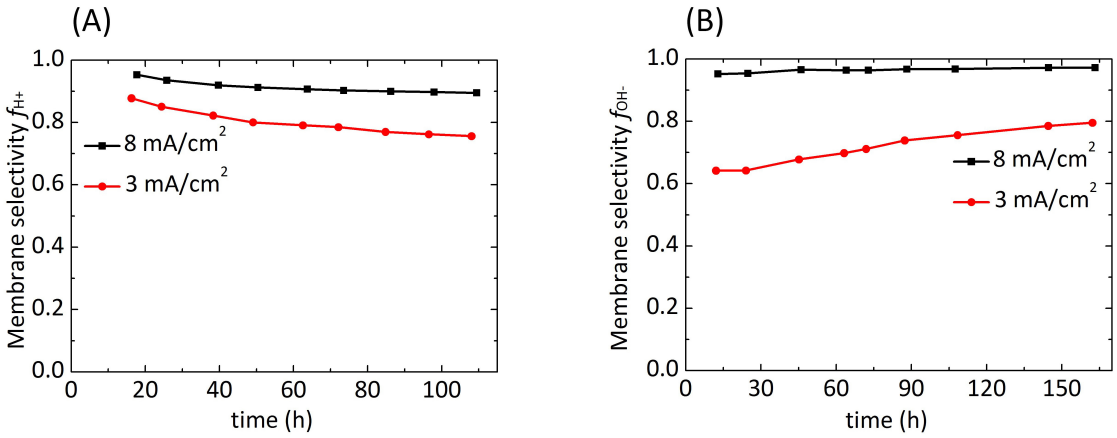

Figure 4.7: (A) Selectivity of the bipolar membrane for protons as a function of time, when operated at two different current densities. (B) Selectivity of the bipolar membrane for hydroxide ions as a function of time, for two different current densities. Pt mesh electrodes were used as cathode and anode in (A) and (B).

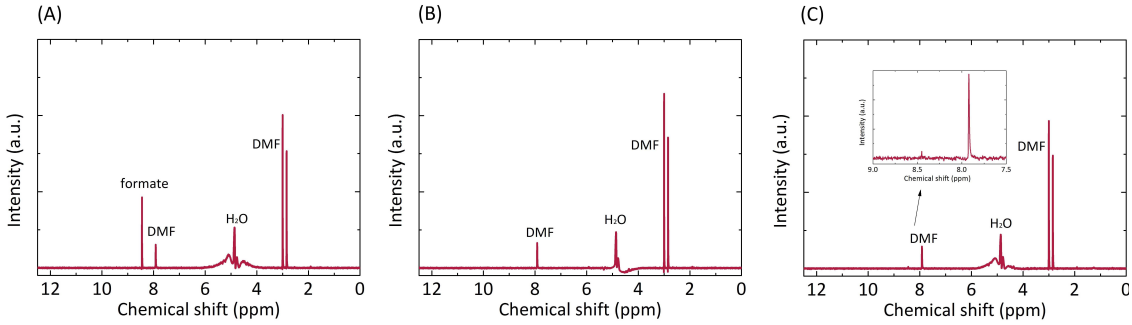

Figure 4.8: ^{1}H-NMR spectrum of the solutions in the cathode (A) and anode (B) compartments in a 2-electrode electrochemical configuration. Signals at 7.92, 3.01 and 2.98 ppm are the internal standard DMF, while the singlet at 8.44 ppm is formate. The concentration of formate in catholyte was ~ 1 mM, and no formate was detected in the anolyte by ^{1}H-NMR spectroscopy. The membrane area was ~0.03 cm^2, and the membrane current density during operation was 8.5 mA cm^{-2}. The volumes of the catholyte and anolyte were 50 ml and 25 ml, respectively. The operation time was 3 hours. When the concentration of formate in catholyte increased to 0.1 M, and the area of the BPM increased to 0.12 cm^2 (other conditions unchanged), a small amount of formate (~ 16 µM) in the anolyte was detected by ^{1}H-NMR spectrum (C) after 3 hours of operation. The current density for formate crossover from catholyte to anolyte was ~30 µA cm^{-2}.

was replaced by $CsHCO_3$(aq), so that small increases in the K^+ concentration could be detected. The measured K^+ leak rate in the $CsHCO_3$(aq)/KOH(aq) configuration also presented an upper-bound for the behavior of the $KHCO_3$(aq)/KOH(aq) configuration due to the absence of the diffusional driving force for K^+ transport from the anolyte to the

cathloyte in the all-K^+-containing system. The membrane selectivities, f_{H^+} (f_{OH^-}), were defined as the ratio of proton-carried (hydroxide-carried) charge passed relative to the total charge passed through the membrane. At an operational current density of 3 mA cm^{-2}, the potassium leak current and the bicarbonate leak current constituted 10 - 25% and 20 - 35%, respectively, of the total current passed through the bipolar membrane. When the membrane current density was increased to 8 mA cm^{-2}, the membrane selectivity for protons increased to >90%, and the membrane selectivity for hydroxide ions increased to >95%. The crossover of the formate product was low (Figure 4.8). In the 3-electrode electrochemical measurement, the cathode compartment was separated by from the Pt counter electrode by a BPM, so the high Faradaic efficiency (>94%) measured in the cathode compartment at low overpotentials (from 45 mV to -120 mV, Figure 4.3B) also provides evidence for a low rate of formate crossover through the BPM. The product crossovers were minimal because the negatively charged formate ion was effectively blocked by the negatively charged cation exchange membrane in the bipolar membrane system.

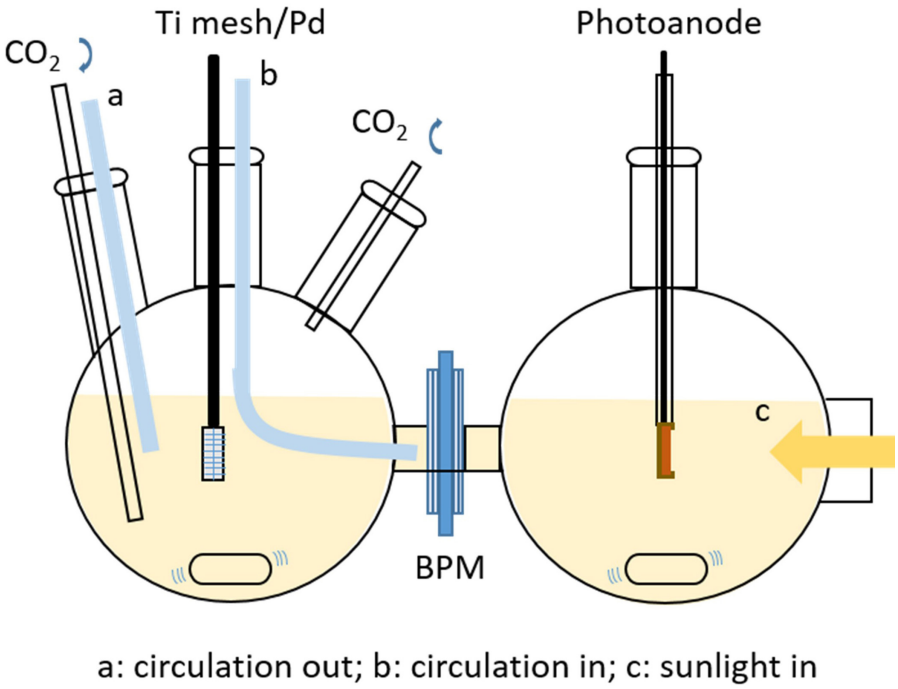

Figure 4.9: Schematic illustration of a 2-electrode electrochemical setup. The blue tubes were connected to a peristaltic pumping system, which facilitated the removal of CO_2 bubbles and prevented voltage loss caused by bubbles.

Figure 4.9 shows a schematic illustration of the 2-electrode electrochemical setup. CO_2 at 1 atm (ALPHAGAZ 1) was bubbled continuously into the 2.8 M $KHCO_3$(aq) catholyte. The blue tubes shown in the figure were connected to a peristaltic pumping system that

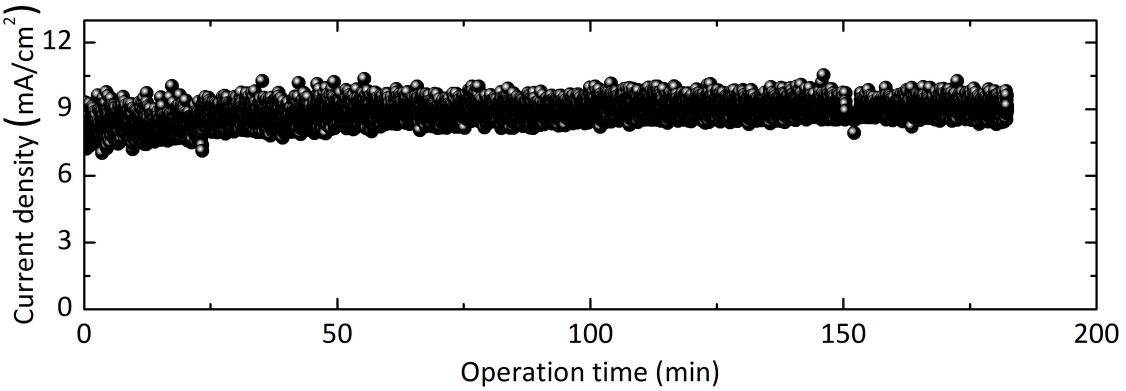

Figure 4.10: The unassisted CO_2R current density as a function of operational time using a GaAs/InGaP/TiO_2/Ni photoanode and a Pd/C-coated Ti mesh cathode in a 2-electrode electrochemical configuration (Figure 4.9) under 100 mW cm^{-2} of simulated AM1.5 illumination.

facilitated removal of CO_2 bubbles and thus minimized associated fluctuations in the cell voltage and current. The geometric areas of the GaAs/InGaP/TiO_2/Ni photoanode, bipolar membrane, Nafion membrane, and Pd/C/Ti cathode were mutually similar, at 0.030 cm^2, 0.030 cm^2, 0.030 cm^2, and 0.040 cm^2 respectively. The relatively small active device area was due to the behavior of the photoanode in 1.0 M KOH(aq). The electrocatalytic performance, stability, and Faradaic efficiency for product formation at the cathode, the J-E properties of the photoanode, and the current-voltage characteristics of the bipolar membrane, were independent of the geometric areas of these cell components (Figure 4.11), but the stability of the photoanode was dependent on the electrode area due to pinholes and other defects at large electrode areas providing a source for active dissolution and thus instability of the III-V semiconductors in 1.0 M KOH(aq) (see Appendix A.11). Small area photoanodes have exhibited stable operation for > 100 h with near-unity Faradic efficiency for the OER[16, 27]. Figure 4.10 shows the current density for the unassisted CO_2R reaction as a function of the time under 100 mW cm^{-2} of simulated AM1.5 illumination, when the GaAs/InGaP/TiO_2/Ni photoanode was directly wired to the Pd/C nanoparticle-coated Ti mesh cathode without application of any external bias. The photocurrent density was 8.7 ± 0.5 mA cm^{-2}. The overpotential for the Pd/C nanoparticle-coated Ti mesh cathode was recorded during the 3 h stability test, as shown in Figure 4.12A. During the stability test, the overpotential was between -40 mV and -100 mV, therefore as shown in Figure 4.3B, the Faradaic efficiency of CO_2 reduction to formate was ~100%, 98%, 95%, 94% after 30 min, 1 h, 2 h, 3 h, respectively. The corresponding solar-to-formate conversion efficiency at these times was thus 10.5%, 10.3%, 10.0%, and 9.9%, respectively (see Appendix A.12 for details on calculation of the solar-to-

formate conversion efficiency).[8, 28] The photocurrent density vs voltage behavior of the 2-electrode system (Figure 4.12B) exhibited mutually similar onset potentials and light-limited current densities before and after a 3 h stability test (Figure 4.10), indicating minimal corrosion of the photoanode over this time period.

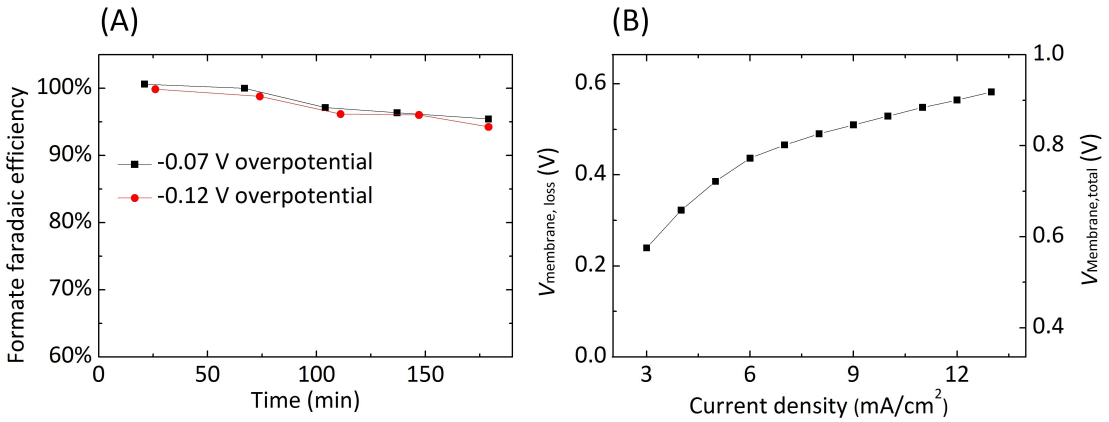

Figure 4.11: (A) Faradaic efficiency of formate production as a function of time, for -70 mV and 120 mV overpotentials, using 1 cm^2 Pd/C nanoparticle-coated Ti mesh in CO_2-saturated 2.8 M $KHCO_3$(aq). (B) Membrane voltage loss (left axis) and measured total membrane voltage (right axis) as a function of the current density normalized to the 0.785 cm^2 BPM area. The cell configuration was $KHCO_3$(aq) (pH=8.0)/BPM/KOH (aq, pH=13.7).

Figure 4.13 shows the measured (red) and calculated (dotted black) 2-electrode current density vs voltage behavior of the GaAs/InGaP/TiO_2/Ni photoanode wired to a Pd/C-coated Ti mesh cathode under 100 mW cm^{-2} of simulated Air Mass (AM) 1.5 illumination. The calculated 2-electrode current density vs voltage behavior (dotted black) was obtained by using the current-voltage behavior of the tandem solid-state photoabsorber (dotted orange) in conjunction with the overall polarization characteristic of a p^+-Si/TiO_2/Ni anode and a Pd/C-coated Ti mesh cathode in the 2-electrode BMP configuration ($KHCO_3$/BPM/KOH) (black). The calculated 2-electrode current density vs voltage behavior was in good agreement with the experimental measurements. The electrosynthetic cell component required 2.04 V to operate at a current density of 8.5 mA cm^{-2}, and was thus well matched to the maximum power point of the photovoltaic tandem junction component of in the photoanode. The electrosynthetic cell thus operated with an electrical-to-fuel conversion efficiency, $\eta_{electrolyzer}$, of 1.21 V/2.04 V = 59.3% at 8.5 mA cm^{-2} current density[15, 28]. Figure 4.13 also shows the overall polarization characteristics of the 2-electrode Nafion membrane configuration ($KHCO_3$/Nafion/$KHCO_3$) (blue) using the same electrode materials. Due to the large overpotential for the Ni catalyst

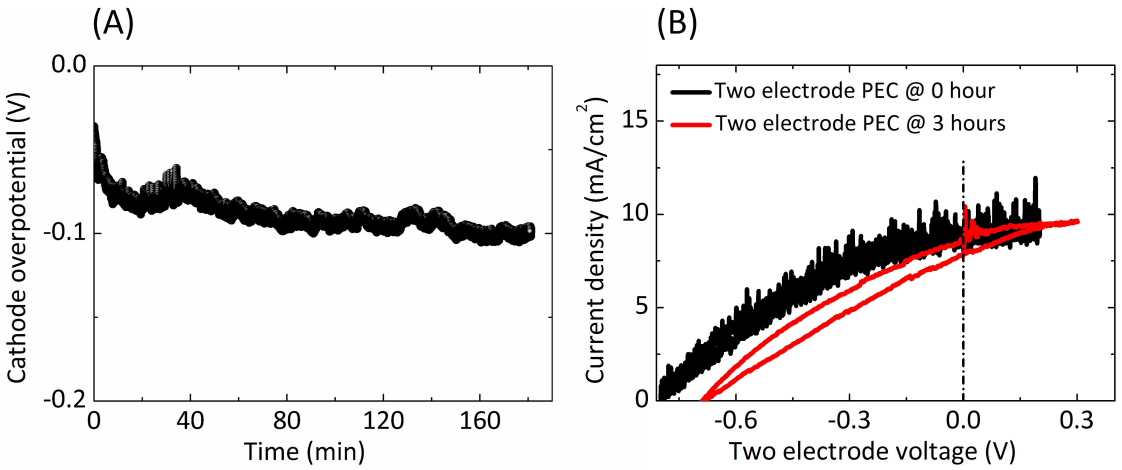

Figure 4.12: (A) The overpotential for a Pd/C cathode during solar-driven CO_2R using GaAs/InGaP/TiO_2/Ni as a photoanode in a 2-electrode electrochemical configuration under simulated AM1.5 1-Sun illumination. (see A.9 for discussion about the time dependence of the potential for the Pd/C-coated Ti mesh cathode.) (B) 2-electrode J-V behavior with a GaAs/InGaP/TiO_2/Ni photoanode and a Pd/C on Ti mesh cathode in a BPM configuration under simulated AM1.5 1-Sun illumination at 0 and 3 h, respectively, of the stability test.

to effect the OER at the near-neutral pH (Figure 4.4C), obtaining an operational current density of ~8.5 mA cm^{-2} to drive the overall CO_2R reaction in conjunction with the OER required an additional ~180 mV of voltage in the Nafion-containing cell relative to the voltage required to operate the BPM-containing cell (Table 4.1, 4.2). For comparison, a Nafion-containing cell for the electrochemical reduction of 1 atm of CO_2 to CO while performing the OER at the anode in 0.4 M buffered KH_2PO_4(aq) (pH=7.3)/Nafion/0.5 M $KHCO_3$(aq) (pH=7.3) required 2.5 V to produce a current density of 1 mA cm^{-2}[29]. Transport of K^+ between the anolyte and catholyte during steady-state operation would also electrodialyze the electrolytes in the Nafion-containing cell. Circulation or recirculation might potentially minimize the steady-state K^+-ion concentration polarization of the system[30], but would entail significant challenges in separation of the low concentration of the liquid product, formate, in the catholyte. In contrast, the robust product separation afforded by the BPM would allow for production of a high concentration of formate, which would be advantageous in a down-stream separation process. Additionally, the Ni catalyst is not stable for OER at near-neutral pH[31]. Use of the bipolar membrane thus relaxed the electrolyte constraints and allowed the incorporation of this active OER catalyst[32] in the device.

TiO2-protected tandem III-V photoanodes have been used in a variety of cell configu-

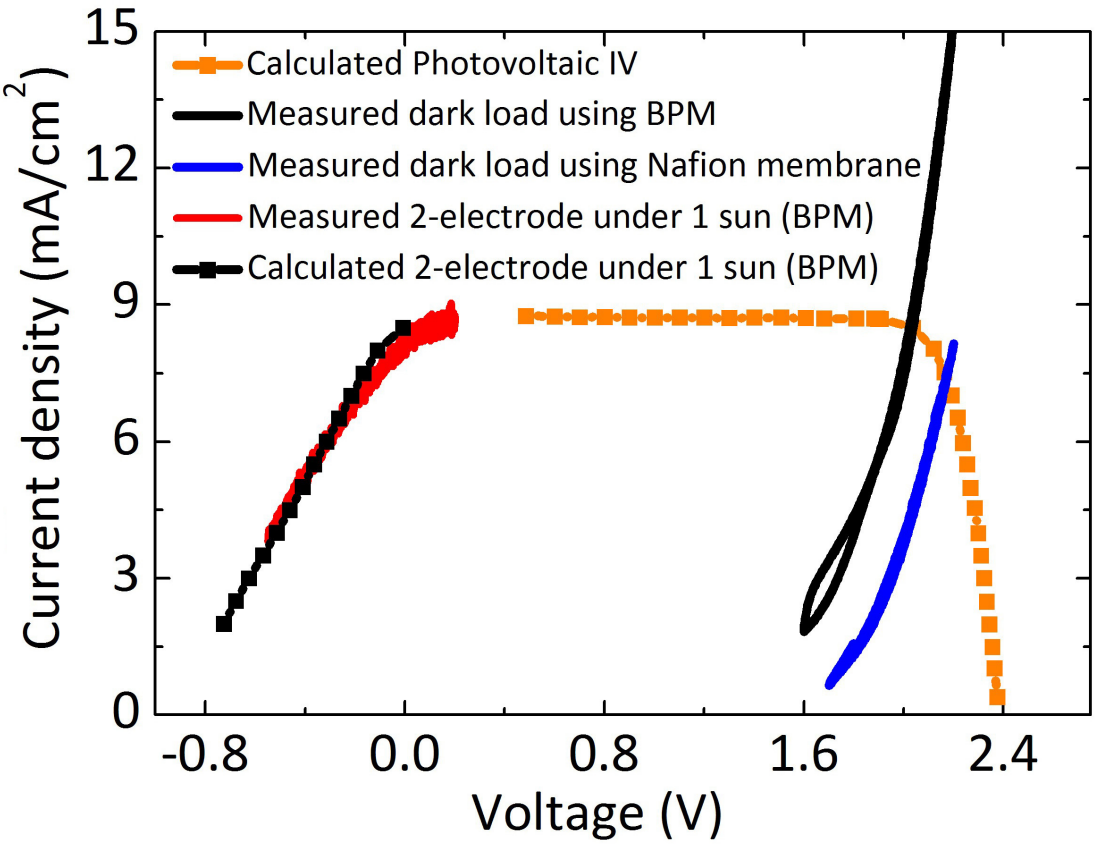

Figure 4.13: The overall polarization characteristics for the CO_2R reaction and the OER using a p^+-Si/TiO_2/Ni anode and a Pd/C-coated Ti mesh cathode in the 2-electrode BMP configuration ($KHCO_3$/Nafion/KOH) (black) as well as in the 2-electrode Nafion membrane configuration ($KHCO_3$/Nafion/ $KHCO_3$) (blue). The measured (red) and calculated (black) 2-electrode current-voltage behavior of the GaAs/InGaP/TiO_2/Ni photoanode wired to a Pd/C-coated Ti mesh cathode were measured under 100 mW cm^{-2} of simulated AM1.5 illumination. The calculated current density-voltage characteristic of the solid-state tandem cell (orange)[16, 24].

rations to construct high (>10%) efficiency solar-driven water-splitting cells[16, 24]. The J-E performance of the cathodes in such systems[33] are comparable to the J-E performance of the Pd/C nanoparticle-coated CO_2R cathodes used herein, providing a basis for comparison of the efficiency losses in each of the cell types in the limit of having a low overpotential, selective cathode in each system. Although the 10% efficiency for CO_2R reported herein is comparable in magnitude to the 10% efficiency reported for photoelectrosynthetic solar-driven water splitting cells that use either anion exchange or bipolar membranes[16, 24, 34], the efficiencies of these different electrosynthetic cells can not be directly compared at the systems level. Solar-driven water-splitting cells in alkaline

electrolytes produce physically separate streams of H_2(g) and O_2(g) (either at 1 atm or under higher pressures due to electrochemical compression. Electrochemical hydrogen compression means hydrogen is supplied to the anode, and compressed hydrogen is collected at the cathode.) from an abundant reagent (including liquid or vapor H_2O from humidified ambient air[35, 36], have minimal (<100 mV) voltage losses associated with the anion-exchange membrane and electrolyte, utilize relatively low (<300 mV) overpotential electrocatalysts for the OER, and thus will provide the highest STF[16, 37]. Use of a bipolar membrane allows for operation of the photoanode in electrolytes at near-neutral pH values, which are less corrosive to photoelectrodes, especially for III-V compound semiconductors, relative to the alkaline electrolyte (e.g., 1.0 M KOH), and facilitate the use of relatively large area ($\sim$1 cm^2) photoelectrodes due to stabilization by TiO_2 protective coatings[24]. However, bipolar membranes introduce additional membrane-derived voltage losses[20–24]. The near-neutral pH operation also entails increased overpotential losses due to the reduced activity of available OER catalysts operating under such conditions[12, 31, 38, 39]. The available OER catalysts also obscure light and are semi-soluble and unstable on the electrode surface during operation at near-neutral pH[31]. In addition, the finite ion crossovers in such cells would eventually lead to electrodialysis of the electrolyte during passive, long-term cell operation. The CO_2R cells evaluated herein share the same STF limitations as solar-driven water-splitting systems that utilize a bipolar membrane having one electrolyte at near-neutral pH and the other electrolyte under either strongly alkaline or acidic conditions (Table 4.1, 4.2). The CO_2R cells moreover require that concentrated, purified (to eliminate highly electroactive, ambient O_2) CO_2 feeds are distributed over large electrode areas, due to mass-transport limitations on the atmospheric CO_2 flux into aqueous electrolytes[4], as well as entail a loss of selectivity in reduction of CO_2 relative to H_2 production at atmospheric (400 ppmv) concentrations of CO_2 in the cathode feed. The formate would also have to be separated from the aqueous solution, as would any other water-soluble CO_2R product such as methanol, ethanol or isopropanol, requiring an energy-intensive separation step. Use of flue gas as the (unsustainable) CO_2 source would require removal of the electroactive O_2(g) as well as purification of the flue gas stream to remove NO_x, SO_x, Hg, and other trace flue gas components that are either electroactive or that can poison the cathode. The gas stream would then need to be humidified, cooled to near ambient temperatures, and the resulting gas feedstock distributed over the $\sim 10^7$ m^2 area that would be required to collect the incident solar photon flux necessary to reduce the CO_2 that is emitted from a 100 MW(electric) coal-fired power plant (see Appendix A.13 for calculation details). Large storage reservoirs for the CO_2 would also be required to compensate for the 20% capacity factor of the solar-driven pho-

toelectrosynthetic cell relative to the nearly continuous CO_2 emissions stream emanating from the power plant.

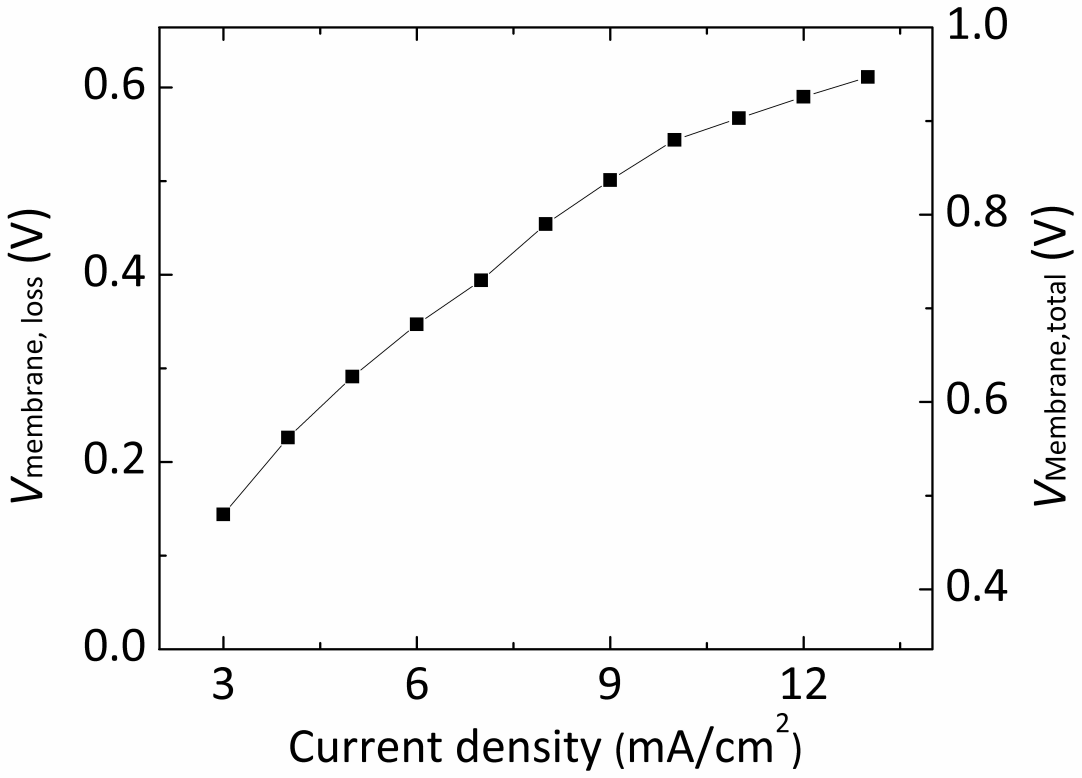

Figure 4.14: Membrane voltage loss (left axis) and measured total membrane voltage (right axis) as a function of the current density normalized to the 0.030 cm^2 BPM area. The cell configuration was $KHCO_3$(aq) (pH=8.0)/BPM/ $KHCO_3$(aq) (pH=8.0).

4.3 Conclusions

In summary, a solar-driven CO_2 reduction photovoltaic-assisted electrosynthetic cell was demonstrated at a solar-to-fuels energy-conversion efficiency of 10% using a tandem GaAs/InGaP/TiO_2/NiO_x photoanode in 1.0 M KOH(aq), a Pd/C nanoparticle coated Ti mesh cathode in 2.8 M $KHCO_3$(aq), and a bipolar membrane reducing a purified feed stream of 1 atm CO_2(g). At the operational current density of 8.5 mA cm^{-2}, the cathode exhibited <100 mV overpotential and >94% Faradaic efficiency for CO_2 reduction to formate in 2.8 M $KHCO_3$(aq) (pH=8.0), the anode exhibited 320 ± 7 mV overpotential for OER in 1.0 M KOH (aq) (pH=13.7), and the bipolar membrane exhibited ~480 mV voltage loss with minimal product crossovers and >90% and >95% selectivity for proton and hydroxide ions, respectively. The bipolar membrane effectively coupled together

Components	(Cathode) 2.8 M $KHCO_3$/BPM/1.0 M KOH (Anode)	(Cathode) 2.8 M $KHCO_3$/BPM/2.8 M $KHCO_3$ (Anode)	(Cathode) 2.8 M $KHCO_3$/Nafion Membrane/2.8 M $KHCO_3$ (Anode)
Membrane	0.507 ± 0.038 *V*	~ 0.880 V (Figure 4.14)	0.214 ± 0.015 *V*
Ni OER overpotential	0.33 ± 0.01 *V*	0.793 ± 0.026 *V*	0.793 ± 0.026 *V*
Pd/C coated Ti mesh CO_2R to formate overpotential	0.057 ± 0.008 *V*	0.057 ± 0.008 *V*	0.057 ± 0.008 *V*
Total voltage loss	~ 0.89 *V*	~ 1.73 *V*	~ 1.06 *V*

Table 4.1: Comparison of voltage losses for three cell configurations at $J_{electrode/membrane}$ = 10 mA cm^{-2}

Components	(Cathode) 2.8 M $KHCO_3$/BPM/1.0 M KOH (Anode)	(Cathode) 2.8 M $KHCO_3$/BPM/2.8 M $KHCO_3$ (Anode)	(Cathode) 2.8 M $KHCO_3$/Nafion Membrane/2.8 M $KHCO_3$ (Anode)
Membrane	~ 0.48 *V*	~ 0.82 V (Figure 4.14)	~ 0.18 *V*
Ni OER overpotential	0.320 ± 0.007 *V*	0.783 ± 0.026 *V*	0.783 ± 0.026 *V*
Pd/C coated Ti mesh CO_2R to formate overpotential	0.052 ± 0.008 *V*	0.052 ± 0.008 *V*	0.052 ± 0.008 *V*
Total voltage loss	~ 0.85 *V*	~ 1.66 *V*	~ 1.01 *V*

Table 4.2: Comparison of voltage losses for three cell configurations at $J_{electrode/membrane}$ = 10 mA cm^{-2}

two electrolytes that were separately effective for the CO_2R reaction and for the OER, and produced lower total overpotentials and higher efficiency than could at present be obtained in a single-electrolyte CO_2 reduction cell. The photoelectrosynthetic cells also allowed a comparative evaluation of the operational constraints associated with sustainable solar-driven CO_2 reduction systems relative to sustainable solar-driven water-splitting systems.

References

[1] N. S. Lewis. “Research Opportunities to Advance Solar Energy Utilization”. In: *Science* 351.6271 (2016), aad1920.

[2] N. Gupta, M. Gattrell, and B. MacDougall. “Calculation for the Cathode Surface Concentrations in the Electrochemical Reduction of CO2 in KHCO3 Solutions”. In: *J. Appl. Electrochem.* 36.2 (2006), pp. 161–172.

[3] M. R. Singh, E. L. Clark, and A. T. Bell. “Effects of Electrolyte, Catalyst, and Membrane Composition and Operating Conditions on the Performance of Solar-Driven Electrochemical Reduction of Carbon Dioxide”. In: *Phys. Chem. Chem. Phys.* 17.29 (2015), pp. 18924–18936.

[4] Y. Chen, N. S. Lewis, and C. Xiang. “Operational Constraints and Strategies for Systems to Effect the Sustainable, Solar-driven Reduction of Atmospheric CO2”. In: *Energy Environ. Sci.* 8.12 (2015), pp. 3663–3674.

[5] B. Kumar et al. “Photochemical and Photoelectrochemical Reduction of CO2”. In: *Annu. Rev. Phys. Chem.* 63 (2012), pp. 541–569.

[6] Y. Hori et al. “Electrocatalytic Process of CO Selectivity in Electrochemical Reduction of CO2 at Metal-Electrodes in Aqueous-Media”. In: *Electrochim. Acta* 39.11-12 (1994), pp. 1833–1839.

[7] X. Min and M. W. Kanan. “Pd-Catalyzed Electrohydrogenation of Carbon Dioxide to Formate: High Mass Activity at Low Overpotential and Identification of the Deactivation Pathway”. In: *J. Am. Chem. Soc.* 137.14 (2015), pp. 4701–4708.

[8] M. Schreier et al. “Efficient Photosynthesis of Carbon Monoxide from CO2 using Perovskite Photovoltaics”. In: *Nat. Commun.* 6 (2015), p. 7326.

[9] M. Asadi et al. “Robust Carbon Dioxide Reduction on Molybdenum Disulphide Edges”. In: *Nat. Commun.* 5 (2014), p. 4470.

[10] M. Asadi et al. “Nanostructured Transition Metal Dichalcogenide Electrocatalysts for CO2 Reduction in Ionic Liquid”. In: *Science* 353.6298 (2016), pp. 467–470.

[11] B. Zhang et al. “Homogeneously Dispersed Multimetal Oxygen-evolving Catalysts”. In: *Science* 352.6283 (2016), pp. 333–337.

[12] C. C. L. McCrory et al. “Benchmarking Heterogeneous Electrocatalysts for the Oxygen Evolution Reaction”. In: *J. Am. Chem. Soc.* 135.45 (2013), pp. 16977–16987.

[13] C. C. L. McCrory et al. “Benchmarking Hydrogen Evolving Reaction and Oxygen Evolving Reaction Electrocatalysts for Solar Water Splitting Devices”. In: *J. Am. Chem. Soc.* 137.13 (2015), pp. 4347–4357.

[14] J. O. M. Bockris, A. K. Reddy, and M. E. Gamboa-Aldeco. *Modern Electrochemistry*. New York City, U.S.A.: Springer, 2000.

[15] C. Xiang, K. M. Papadantonakis, and N. S. Lewis. “Principles and Implementations of Electrolysis Systems for Water Splitting”. In: *Mater. Horiz.* 3.3 (2016), pp. 169–173.

[16] E. Verlage et al. “A Monolithically Integrated, Intrinsically Safe, 10% Efficient, Solar-Driven Water-Splitting System Based on Active, Stable Earth-Abundant Electrocatalysts in Conjunction with Tandem III-V Light Absorbers Protected by Amorphous TiO2 Films”. In: *Energy Environ. Sci.* 8.11 (2015), pp. 3166–3172.

[17] T. Arai, S. Sato, and T. Morikawa. “A Monolithic Device for CO2 Photoreduction to Generate Liquid Organic Substances in a Single-compartment Reactor”. In: *Energy Environ. Sci.* 8.7 (2015), pp. 1998–2002.

[18] H. S. Jeon et al. “A Monolithic and Standalone Solar-fuel Device having Comparable Efficiency to Photosynthesis in Nature”. In: *J. Mater. Chem. A* 3.11 (2015), pp. 5835–5842.

[19] Y. Sugano et al. “Crucial Role of Sustainable Liquid Junction Potential for Solar-to-Carbon Monoxide Conversion by a Photovoltaic Photoelectrochemical System”. In: *RSC Adv.* 5.67 (2015), pp. 54246–54252.

[20] N. M. Vargas-Barbosa et al. “Assessing the Utility of Bipolar Membranes for use in Photoelectrochemical Water-Splitting Cells”. In: *ChemSusChem* 7.11 (2014), pp. 3017–3020.

[21] M. B. McDonald et al. “Use of Bipolar Membranes for Maintaining Steady-State pH Gradients in Membrane-Supported, Solar-Driven Water Splitting”. In: *ChemSusChem* 7.11 (2014), pp. 3021–3027.

[22] M. Ünlü, J. Zhou, and P. A. Kohl. “Hybrid Anion and Proton Exchange Membrane Fuel Cells”. In: *J. Phys. Chem. C* 113.26 (2009), pp. 11416–11423.

[23] D. A. Vermaas, M. Sassenburg, and W. A. Smith. “Photo-assisted Water Splitting with Bipolar Membrane Induced pH Gradients for Practical Solar Fuel Devices”. In: *J. Mater. Chem. A* 3.38 (2015), pp. 19556–19562.

[24] K. Sun et al. “A Stabilized, Intrinsically Safe, 10% Efficient, Solar-Driven Water-Splitting Cell Incorporating Earth-Abundant Electrocatalysts with Steady-State pH Gradients and Product Separation Enabled by a Bipolar Membrane”. In: *Adv. Energy Mater.* 6.13 (2016), p. 1600379.

[25] R. Kortlever et al. “Electrochemical CO2 Reduction to Formic Acid at Low Overpotential and with High Faradaic Efficiency on Carbon-Supported Bimetallic Pd–Pt Nanoparticles”. In: *ACS Catal.* 5.7 (2015), pp. 3916–3923.

[26] K. Sun et al. “Stable Solar-Driven Oxidation of Water by Semiconducting Photoanodes Protected by Transparent Catalytic Nickel Oxide Films”. In: *Proc. Natl. Acad. Sci. U.S.A.* 112 (2015), pp. 3612–3617.

[27] S. Hu et al. “Amorphous TiO(2) Coatings Stabilize Si, GaAs, and GaP Photoanodes for Efficient Water Oxidation”. In: *Science* 344.6187 (2014), pp. 1005–9.

[28] R. H. Coridan et al. “Methods for Comparing the Performance of Energy-Conversion Systems for Use in Solar Fuels and Solar Electricity Generation”. In: *Energy Environ. Sci.* (2015).

[29] A. Tatin et al. “Efficient Electrolyzer for CO2 Splitting in Neutral Water Using Earth-abundant Materials”. In: *Proc. Natl. Acad. Sci. U.S.A.* 113.20 (2016), pp. 5526–5529.

[30] M. A. Modestino et al. “Robust Production of Purified H2 in a Stable, Self-Regulating, and Continuously Operating Solar Fuel Generator”. In: *Energy Environ. Sci.* 7.1 (2014), pp. 297–301.

[31] A. Minguzzi et al. “Dynamic Potential-pH Diagrams Application to Electrocatalysts for Water Oxidation”. In: *Chem. Sci.* 3.1 (2012), pp. 217–229.

[32] L. Trotochaud et al. “Nickel-Iron Oxyhydroxide Oxygen-Evolution Electrocatalysts: The Role of Intentional and Incidental Iron Incorporation”. In: *J. Am. Chem. Soc.* 136.18 (2014), pp. 6744–6753.

[33] F. H. Saadi et al. “CoP as an Acid-Stable Active Electrocatalyst for the Hydrogen-Evolution Reaction: Electrochemical Synthesis, Interfacial Characterization and Performance Evaluation”. In: *J. Phys. Chem. C* 118.50 (2014), pp. 29294–29300.

[34] J. Luo et al. “Bipolar Membrane-Assisted Solar Water Splitting in Optimal pH”. In: *Adv. Energy Mater.* 6.13 (2016), p. 1600100.

[35] S. Kumari et al. “Solar Hydrogen Production from Seawater Vapor Electrolysis”. In: *Energy Environ. Sci.* 9.5 (2016), pp. 1725–1733.

[36] J. M. Spurgeon and N. S. Lewis. “Proton Exchange Membrane Electrolysis Sustained by Water Vapor”. In: *Energy Environ. Sci.* 4.8 (2011), pp. 2993–2998.

[37] Y. Chen et al. “A Sensitivity Analysis to Assess the Relative Importance of Improvements in Electrocatalysts, Light Absorbers, and System Geometry on the Efficiency of Solar-fuels Generators”. In: *Energy Environ. Sci.* 8.3 (2015), pp. 876–886.

[38] Y. Surendranath, M. Dincă, and D. G. Nocera. “Electrolyte-Dependent Electrosynthesis and Activity of Cobalt-Based Water Oxidation Catalysts”. In: *J. Am. Chem. Soc.* 131.7 (2009), pp. 2615–2620.

[39] M. W. Kanan and D. G. Nocera. “In Situ Formation of an Oxygen-Evolving Catalyst in Neutral Water Containing Phosphate and Co2+”. In: *Science* 321.5892 (2008), pp. 1072–1075.

Appendix A

SUPPLEMENTARY DISCUSSION AND CALCULATION DETAILS

A.1 Calculation of solar-to-O_2(g) ideal regenerative-cell conversion efficiency:

Given the J-E data for a photoanode (potential vs RHE), the potential axis was converted to the potential relative to $E^{o'}(O_2/H_2O)$ by subtracting the value of E versus RHE from 1.23 V. The resulting potential was then multiplied by the corresponding current at each point, and the maximum value of the product for the data was found and divided by 100 to yield the solar-to-O_2(g) ideal regenerative-cell conversion efficiency. Hence, the maximum value of (E vs $E^{o'}(O_2/H_2O)$) × J(at E vs $E^{o'}(O_2/H_2O)$) divided by 100 yielded the solar-to-O_2(g) ideal regenerative-cell conversion efficiency.

A.2 Electrochemical Impedance Spectroscopy and Mott-Schottky Analysis:

Electrochemical impedance spectroscopy was performed in 50 mM $K_3Fe(CN)_6$, 350 mM $K_4Fe(CN)_6$ and 1.0 M KCl(aq). The solution was in the dark during the measurements. The electrochemical impedance data were fit to a model that consisted of a parallel resistor and a capacitor with a fixed constant-phase element at the Si interface arranged electrically in series with another resistor and capacitor in parallel at the NiO_x/electrolyte interface.

The reverse-bias dependence of the area-normalized differential capacitance in the depletion region of the semiconductor is given by the Mott-Schottky relation:

$$\frac{1}{C^2} = \frac{2}{A^2 \epsilon_0 \epsilon_r q N_d}(V_{app} - V_{fb} - \frac{k_B T}{q})$$

where A is the device area, ϵ_0 is the vacuum permittivity, ϵ_r is the relative permittivity, q is the unsigned charge on an electron, N_d is the donar impurity concentration in the semiconductor, V_{app} is the difference between the applied potential and the redox potential of the solution, V_{fb} is the flat-band potential, k_B is the Boltzmann's constant, and T is the temperature in K. Mott-Schottky plots were linear ($R^2 > 0.999$).

The doping density was calculated using:

$$N_d = \frac{2}{A^2 q \epsilon_0 \epsilon_r [\frac{d(\frac{1}{C^2})}{dV_{app}}]}$$

A.3 Electrochemistry under different light intensities and effective Richardson constant calculation:

Neutral density filters with an optical density (OD) of either 0.2, 0.4, 0.6, 0.8, 1.0 were used to attenuate the intensity of light when performing electrochemistry under 1 Sun for the n-Si/$SiO_{x,RCA}$/Co_3O_4/NiO_x electrode in a solution of 50 mM $K_3Fe(CN)_6$, 350 mM $K_4Fe(CN)_6$ and 1.0 M KCl(aq).

The J-V characteristic of an n-Si/$SiO_{x,RCA}$/Co_3O_4/NiO_x electrode in the dark can be expressed as:

$$J = J_{01}(Exp(\frac{qV}{n_1 k_B T}) - 1) + J_{01}(Exp(\frac{qV}{n_2 k_B T}) - 1)$$

where J_{01} is related to thermionic emission, and J_{02} is the diffusion component.

If only one of the components dominates:

$$V_{oc} = \frac{nk_BT}{q} Ln(\frac{J_{sc} + J_0}{J_0}) \approx \frac{nk_BT}{q} Ln(\frac{J_{sc}}{J_0})$$

A linear fit ($R^2 > 0.99$) of a plot of V_{oc} versus $In(J_{sc})$ yielded $J_0 = 1.5 \times 10^{-7} mA\ cm^{-2}$ and a diode quality factor of n = 1.09.

An estimate of the diffusion component was obtained using:

$$J_{02} = \frac{P_n q D_p}{L_p} \approx 2.7 \times 10^{-10}\ mA\ cm^{-2}$$

A doping density of $N_A = 10^{17}\ cm^{-3}$, a hole-diffusion coefficient of $D_p = 8\ cm^2\ s^{-1}$ [1, 2], and a hole diffusion length of $L_p = 100 \mu m$ were used to estimate the diffusion component.

Under these conditions, $J_{02} << J_0$, so thermionic emission dominates.

To evaluate the thermionic emission component, the following relationship was used:

$$J_0 = \alpha A^* T^2 Exp(-\frac{q\phi_b}{k_B T})$$

where α is the transmission coefficient; the Richardson constant, A^*, for electrons in n-Si is 120 $A\ cm^{-2}\ K^{-2}$; and the barrier height, ϕ_b is:

$$\phi_b = V_{fb} + V_n$$

where V_n is the difference between the potential of the Fermi level and the conduction-band-edge potential of n-Si in the bulk. The value of V_n is 0.15 V for a doping density

of 10^{17} cm^{-3} at T = 298 K. V_{fb} = 0.83 ± 0.02 V was determined from analysis of the Mott-Schottky data. Therefore, ϕ_b = 0.98 ± 0.02 V, yielding:

$$\alpha = \frac{J_0}{A^* T^2 Exp(-\frac{q\phi_b}{k_B T})}$$

and resulting in a value of α = 1.1 for ϕ_b = 1.00 V, and α = 0.24 for ϕ_b = 0.96 V. Hence we estimate that α is on the order of unity for the system of interest.

A.4 Charge required to dissolve the Co_3O_4 interfacial layer:

The thickness of the interfacial Co_3O_4 layer was measured to be 2-3 nm, so 3 nm was used as the thickness in this calculation. Assuming that the mass density of the interfacial layer is 8.9 g cm^{-3} (the highest density among Co, CoO, Co_2O_3, and CoO_2), and that the interfacial layer is Co metal that is oxidized to form CoO2 before being dissolved by 1.0 M KOH(aq), the required charge per cm^2 is:

$$\frac{3 \times 10^{-7} \times 1 \times 8.9}{58.93} \times 96500 \times 4\ cm^{-2} = 0.017\ cm^{-2}$$

The charge passed per cm^2 is:

$$1700 \times 3600 \times 30 \times 10^{-3}\ C\ cm^{-2} = 183600\ C\ cm^{-2}$$

The ratio of the total charge passed to the charge required to dissolve the Co_3O_4 was therefore:

$$\frac{183600}{0.017} \approx 1 \times 10^7$$

A.5 Charge density needed to dissolve the Si wafer:

The thickness of the Si wafer was 0.525 mm, and the mass density of Si is 2.3 g cm^{-3}. Assuming that the Si wafer was oxidized to form K2SiO3, the charge density passed would be:

$$\frac{0.525 \times 10^{-1} \times 1 \times 2.3}{28} \times 4 \times 96500\ cm^{-2} = 1665\ C\ cm^{-2}$$

The ratio of the total charge passed to the charge required to dissolve Si wafer is thus:

$$\frac{183600}{1665} = 110$$

A.6 Discussions about the optimization of the Co_3O_4 thickness for n-Si/$SiO_{x,RCA}$/Co_3O_4 photoanodes:

Figure 3.10 shows that the n-Si/$SiO_{x,RCA}$/60C−Co_3O_4 (~2 nm thick Co_3O_4) photoelectrodes exhibited photocurrent-onset potentials of -1 mV, -244 mV, and -510 mV relative

to the redox couple solution potentials, in contact with $Co(Cp)_2^{+/0}$ – 1.0 M CH_3CN, $Me_{10}Cp_2Fe^{+/0}$ – 1.0 M CH_3CN and $Fe(Cp)_2^{+/0}$ – 1.0 M CH_3CN, respectively. The photocurrent-onset potentials varied significantly (> 500 mV) as the solution potential changed, indicating that some regions of the Si surface were exposed to the solution during the non-aqueous electrochemical experiments. The n-Si/$SiO_{x,RCA}$/60C–Co_3O_4 junction consisted of both low and high barrier-height regions, which reduced the overall open-circuit voltage of the n-Si/$SiO_{x,RCA}$/60C–Co_3O_4 photoanode. Therefore, a thick (> 2 nm) Co_3O_4 film would provide a higher photovoltage n-Si/$SiO_{x,RCA}$/Co_3O_4 junction than a thin Co_3O_4 film. As the thickness of the Co_3O_4 layer was increased up to > 600 ALD cycles, relatively little variation, within experimental error, was observed for the photocurrent-onset potentials for n-Si/$SiO_{x,RCA}$/Co_3O_4 photoanodes, (Figure 3.1B). However, when the Co_3O_4 film was very thick (> 1000 ALD cycles or > 50 nm), the resistance of the film was large (Figure 3.1A).

A.7 Photocurrent density from integration against the AM 1.5G spectrum:

The integrated photocurrent density according to the measured external quantum yield under the spectral distribution of the standard AM 1.5G spectrum was calculated using the following equation:

$$J = \int_{\lambda=350}^{\lambda} \frac{q}{hc} \Phi_{ext}(\lambda) \cdot E(\lambda) \cdot \lambda \cdot \, dx \approx \int_{\lambda=350}^{\lambda} \frac{\Phi_{ext}(\lambda) \cdot \lambda}{1240} \cdot E(\lambda) \cdot \, d\lambda$$

where J is the integrated photocurrent density in A m-2, q is the unsigned charge on an electron, E is the irradiance in W m-2 nm-1, h is Planck's constant (6.63×10^{-34} J s), c is the speed of light (2.998×10^{8} m s^{-1}), Φ_{ext} is the measured external quantum yield, λ is the light wavelength in nm, 1240 is in W nm A^{-1}, and $\Phi_{ext} \cdot \lambda/1240$ is the responsivity in A W^{-1}.

A.8 Extended Stability of n-Si/$SiO_{x,RCA}$/Co_3O_4 photoanodes:

The 100-day stability under continuous operation is encouraging, but it is not practical to perform stability tests lasting a year on every interface of interest. Accelerated testing protocols are needed to address this issue including variations in temperature, changes that might occur due to diurnal cycles, and environmental effects that will determine the rest potential of the electrode in the dark as well as during periods of low illumination.

A.9 Discussion of time dependence of the Faradaic efficiency and potential of the Pd/C coated Ti mesh cathode

The slight decay of the Faradic efficiency and potential of the Pd/C coated Ti mesh cathode was due to CO poisoning of the catalyst, which can be regenerated by brief exposure to air[3], but the pH of the electrolyte was maintained at the initial values throughput the experiments by the use of the bipolar membrane.

A.10 Discussion of nickel catalyst

The catalysts are denoted as Ni because $Ni(OH)_2$ was the catalyst precursor species, however high catalytic activity, such as that observed herein, generally originates from incorporation of trace amounts of Fe into the $Ni(OH)_2$ films to form a Fe-Ni oxyhydroxide OER electrocatalyst[4, 5].

A.11 Performance characteristics of larger area cathodes and bipolar membranes

The Faradaic efficiency of formate production as a function of time, for -70 mV and -120 mV overpotentials, using a 1 cm^2 Pd/C nanoparticle-coated Ti mesh in CO_2-saturated 2.8 M $KHCO_3$(aq) was similar to that observed for cathode that had a geometric area of 0.04 cm^2 (Figure 4.11A). The bipolar membrane voltage loss versus current density, normalized to the 0.785 cm^2 bipolar membrane area, was also similar to that observed for a bipolar membrane having a geometric area of 0.03 cm^2 (Figure 4.11B).

A.12 Calculation and discussion of solar-to-formate conversion efficiency η_{STF}

The equilibrium potential for the $CO_2/HCOO^-$ couple was 0.02 V versus the reversible hydrogen electrode (RHE)[6]. Hence, the voltage required for the full chemical reaction, $2OH^- + 2CO_2 = 2HCOO^- + O_2$, was 1.21 V. The solar-to-fuels efficiency is defined by[7, 8]:

$$\eta_{solar-to-fuels} = \frac{J_{op}[A\ cm^{-2}] \times E_0[V] \times Faradaic\ efficiency\ of\ fuels\ production}{I_{solar}[W\ cm^{-2}]}$$

where J_{op} is operating current density; E_0 is the voltage required for the full chemical reaction; and I_{solar} is the solar power density. In this example:

$$\eta_{STF} = \frac{1.21\ V \times J_{electrode}\ mA\ cm^{-2} \times Faradaic\ efficiency\ of\ formate}{100\ mW\ cm^{-2}}$$

During the stability test, the overpotential for Pd/C coated Ti mesh cathode was between -40 mV and -100 mV, therefore, as shown in Figure 4.3B, the Faradaic efficiency of CO_2 reduction to formate was ~100%, 98%, 95%, 94% after 30 min, 1 h, 2 h, 3 h, respectively. The corresponding solar-to-formate conversion efficiency was thus 10.5%, 10.3%, 10.0%, and 9.9%, respectively.

A.13 Calculation of the area required to collect enough solar photon flux for CO_2 reduction

Consider a coal plant operating 24 hours a day with a CO_2 emission rate of 1400 lb/MWh. Given that the photocurrent density is 8 mA cm^{-2}, and CO_2 is reduced to formate (2-electron process) with an average photocurrent density of 1.6 mA cm^{-2} (20% capacity factor), then for a 100 MW power plant:

The CO_2 emission rate:

$$\frac{1400\ lb/MWh \times 0.4536\ kg/lb}{3600\ s/h} \times 100\ MW = 17.64\ kg/s$$

Photocurrent:

$$\frac{17.64\ kg/s \times 1000\ g/kg}{44\ g/mol} \times 96500\ C/mol \times 2 = 7.74 \times 10^7\ A$$

Area:

$$\frac{7.74 \times 10^7\ A}{0.0016\ A/cm^2} \times 10^{-4} m^2/cm^{-2} = 5 \times 10^6\ m^2$$

Therefore, the required solar photon capture area is on the order of $10^7\ m^2$.

References

[1] C. H. Wang, K. Misiakos, and A. Neugroschel. "Minority-carrier Transport Parameters in n-type Silicon". In: *Electron Devices, IEEE Transactions on* 37.5 (1990), pp. 1314–1322.

[2] W. R. Thurber, R. L. Mattis, and Y. M. Liu. *The Relationship between Resistivity and Dopant Density for Phosphorus- and Boron-doped Silicon*. U.S. Dept. of Commerce, National Bureau of Standards, 1981.

[3] X. Min and M. W. Kanan. "Pd-Catalyzed Electrohydrogenation of Carbon Dioxide to Formate: High Mass Activity at Low Overpotential and Identification of the Deactivation Pathway". In: *J. Am. Chem. Soc.* 137.14 (2015), pp. 4701–4708.

[4] L. Trotochaud et al. "Nickel-Iron Oxyhydroxide Oxygen-Evolution Electrocatalysts: The Role of Intentional and Incidental Iron Incorporation". In: *J. Am. Chem. Soc.* 136.18 (2014), pp. 6744–6753.

[5] D. A. Corrigan. "The Catalysis of the Oxygen Evolution Reaction by Iron Impurities in Thin Film Nickel Oxide Electrodes". In: *J. Electrochem. Soc.* 134.2 (1987), pp. 377–384.

[6] R. Kortlever et al. "Electrochemical CO2 Reduction to Formic Acid at Low Overpotential and with High Faradaic Efficiency on Carbon-Supported Bimetallic Pd–Pt Nanoparticles". In: *ACS Catal.* 5.7 (2015), pp. 3916–3923.

[7] R. H. Coridan et al. “Methods for Comparing the Performance of Energy-Conversion Systems for Use in Solar Fuels and Solar Electricity Generation”. In: *Energy Environ. Sci.* (2015).

[8] M. Schreier et al. “Efficient Photosynthesis of Carbon Monoxide from CO2 using Perovskite Photovoltaics”. In: *Nat. Commun.* 6 (2015), p. 7326.

Appendix B

EXPERIMENTAL DETAILS

B.1 Chemicals

All materials were used as received unless noted otherwise: Sulfuric acid (H_2SO_4, Mallinckrodt Chemicals, ACS Reagent grade, 95%-98%), Potassium hydroxide pellets (KOH, Macron Chemicals, ACS 88%), buffered HF improved (Transene Company Inc.), concentrated hydrochloric acid (HCl, EMD, ACS Reagent grade, 36.5-38%), sulfuric acid (H_2SO_4, Mallinckrodt Chemicals, ACS Reagent grade, 95%-98%), hydrogen peroxide (H_2O_2, Macron Chemicals, ACS grade 30%), potassium chloride (KCl, Macron Chemicals, Granular ACS 99.6%), potassium ferrocyanide trihydrate ($K_4Fe(CN)_6 \cdot 3\,H_2O$, Acros, >99%), potassium ferricide ($K_3Fe(CN)_6$, Fisher Chemicals, certified ACS 99.4%), methanol (CH_3OH, low water content, J. T. Baker, 99.8%), 10 wt.% Pd on Vulcan XC-72 carbon black (Pd/C, Premetek Co.), titanium wire (Ti wire, Alfa Aesar, 99.7%), CO_2 gas (ALPHAGAZ 1), and 10 wt.% Nafion (Sigma-Aldrich). Water with a resistivity $\geqslant$ 18 $M\Omega$ ·cm was obtained from a Barnsted Nanopure deionized (DI) water system. The $KHCO_3$ solution was prepared by vigorously bubbling CO_2(g) through K2CO3 solutions until the pH did not change. The bipolar membrane (fumasep® FBM) was obtained from FuMA-Tech GmbH (St. Ingbert, Germany) and was stored in 1.0 M NaCl(aq) at room temperature. The bipolar membrane (BPM) was cut into 1.5×1.5 cm pieces and rinsed with H_2O before use. Nafion® PFSA 117 membrane (Chemours) with a thickness of 183 μm was obtained from Dupont. The Nafion was soaked in H_2O for > 4 h and rinsed with H_2O before use.

For non-aqueous electrochemistry, acetonitrile (CH_3CN, anhydrous, Sigma-Aldrich, 99.8%) was dried by flowing the solvent through a column of activated Al2O3, followed by storage over 3 activated molecular sieves (Sigma-Aldrich). Lithium perchlorate ($LiClO_4$, Sigma-Aldrich, battery grade 99.99%) was dried at 300 K under a pressure < 1 × 10-3 Torr. Bis(cyclopentadienyl) iron(II) (ferrocene, $FeCp_2$, Sigma-Aldrich), bis (pentamethylcyclopentadienyl) iron ($Me_{10}Cp_2Fe$, decamethyl ferrocene, Strem, 99%), bis (cyclopentadienyl) cobalt(II) (Cp_2Co, cobaltocene, Strem, 98%) and bis (methylcyclopentadienyl) iron (Me_2Cp_2Fe, 1,1'-dimethylferrocene, Sigma-Aldrich, 95%) were purified by sublimation under vacuum. Bis (cyclopentadienyl) iron(III) tetrafluoroborate (ferrocenium, $FeCp_2^+ \cdot BF_4^-$, Sigma Aldrich, technical grade), and bis (cyclopentadienyl)

cobalt(III) hexafluorophosphate (Cobaltocenium hexafluorophosphate, $CoCp_2^+ \cdot PF_6^-$, Sigma-Aldrich, 98%) were recrystallized from diethyl ether (EMD, ACS grade) and CH_3CN (EMD Chemicals, ACS grade), and dried under vacuum. Bis (pentamethylcyclopentadienyl) ferrocenium tetrafluoroborate (decamethylferrocenium, $(Me_{10}Cp)_2Fe^+ \cdot BF_4^-$) and bis (methylcyclopentadienyl) iron tetrafluoroborate ($(Me_2Cp)_2Fe^+ \cdot BF_4^-$) were synthesized by chemical oxidation of the neutral metallocenes [1].

B.2 Preparation of substrates:

Phosphorus-doped (n-type, (100)-oriented, single-side polished, resistivity 0.1-1 ohm cm) and degenerately boron-doped (p^+-type, (100)-oriented, single-side polished, resistivity < 0.005 ohm cm) Si wafers were purchased from Addison Engineering Inc. The n-Si wafers were first cleaned using a piranha etching procedure by soaking the wafers in a mixed solution of H_2SO_4 and H_2O_2 (3:1 by volume) for 10 min. The n-type wafers were then cleaned in a buffered HF etchant for 1 min, followed by etching the Si wafers using an RCA SC-2 procedure consisting of soaking the wafers in a solution of H_2O, concentrated hydrochloric acid and hydrogen peroxide (6:1:1 volume ratio) for 10 min at 75 °C. Finally, the n-type wafers were thoroughly rinsed using DI water and dried with a flow of N_2. This procedure left a thin layer of SiO_x ($SiO_{x,RCA}$) on the surface of the n-Si wafers. The p^+-Si wafers were etched by soaking the samples in a buffered HF oxide etchant for 1 min to remove the native oxide layer before sputter-deposition of NiO_x.

B.3 Atomic-layer deposition of transition metal oxides:

Atomic-layer deposition (ALD) of Co_3O_4 was conducted at 150 °C using cobaltocene and ozone in a Cambridge Nanotech S200 ALD system (all ALD processes were conducted in this system). The cobaltocene precursor was heated and maintained at 80 °C. An ALD cycle consisted of a 2 s pulse of the cobaltocene precursor, a 10 s purge under 20 cm^3 min^{-1} flow of research-grade N_2(g), a 5 s ozone pulse and another 10 s N_2 (g) purge.

ALD of FeO_x was conducted at 150 °C from ferrocene and ozone. The ferrocene was heated and maintained at 85 °C. An ALD cycle consisted of a 5 s pulse of the ferrocene precursor, a 15 s purge under a 20 cm^3 min^{-1} flow of research-grade N_2(g), a 5 s ozone pulse, and another 15 s N_2 (g) purge.

ALD of NiO_x was conducted at 150 °C using $Ni(EtCp)_2$ and ozone. The Ni(EtCp)2 precursor was heated and maintained at 60 °C. An ALD cycle consisted of a 0.5 s pulse of the $Ni(EtCp)_2$ precursor, a 4 s purge under a 20 cm^3 min^{-1} flow of research-grade N_2(g), a 7 s ozone pulse, and another 60 s N_2 (g) purge.

B.4 Sputter-deposition of NiO_x

NiO_x was deposited via reactive RF sputtering from a Ni target (Kurt Lesker, 2" diameter 0.125" thickness, 99.95%) using an AJA high-vacuum magnetron sputtering system (AJA International Inc.). The O_2 and Ar flows were kept at 1 sccm and 20 sccm, respectively, while the working pressure was held at 5 mTorr, with the substrates maintained at 300 °C. A deposition rate of 0.04 nm/s was maintained by tuning the sputtering power on the Ni target.

Sputtered NiO_x films deposited on semiconductor substrates have demonstrated multiple desired functionalities simultaneously, including protection against corrosion, hole conduction, and inherent activity for the water-oxidation reaction. Moreover, tuning the physical thickness of the film to 75-85 nm (depending on the refractive index of the substrate) results in enhanced transparency of the film especially under water-oxidation conditions, negligible losses due to film resistivity, and antireflective properties which optimize absorption within the Si substrate [2–4].

B.5 Preparation of electrodes:

The back sides of the Si samples were rubbed with an In-Ga alloy (Alfa Aesar, 99.99%) to form ohmic contacts. Ag paste was then used to attach the ohmic contact to a coiled, tin-plated Cu wire (McMaster-Carr) which was then threaded through a glass tube (Corning Inc., Pyrex tubing, 7740 glass). The samples were then encapsulated and sealed to the glass tube using grey epoxy (Hysol 9460F). The exposed electrode surfaces were imaged with a high-resolution optical scanner (Epson perfection V370 with a resolution of 2400 psi) and the areas were measured using ImageJ software. All of the electrodes were 0.1-0.2 cm^2 in area unless specified otherwise.

B.6 Aqueous and methanol electrochemical measurements:

For electrochemical measurements in 1.0 M KOH(aq), including photoelectrochemical, spectral response and electrochemical impedance spectroscopy, a mercury/mercury oxide (Hg/HgO in 1.0 M KOH(aq), CH instruments, CH152) electrode was used as the reference electrode, and a carbon cloth in a fritted glass tube (gas dispersion tube Pro-D, Aceglass, Inc.) was used as the counter electrode. The Hg/HgO reference electrode had a potential of 0.926 V versus the reversible hydrogen electrode, RHE. For electrochemical measurements performed in 50 mM $K_3Fe(CN)_6$, 350 mM $K_4Fe(CN)_6$ and 1.0 M KCl as well as for measurements in non-aqueous solutions, a Pt wire (0.5 mm diameter, 99.99% trace metal basis, Alfa, Aesar) was used as the reference electrode and a Pt gauze was used as the counter electrode. A custom electrochemical cell with a flat glass (Pyrex) bottom was

used for all electrochemical measurements. During measurements, the electrolyte was vigorously agitated with a magnetic stir bar driven by a model-train motor (Pittman). A Xe arc lamp (Newport 67005 and 69911) equipped with an IR filter (Newport 61945) and with an AM 1.5 filter (Newport 81094 and 71260), as well as ELH-type (Sylvania/Osram) and ENH-type (EIKO) tungsten-halogen lamps with a custom housing with a transformer (Staco Energy Products Co.), were used for photoelectrochemical stability measurements. The illumination intensity was calibrated by placing a Si photodiode (FDS100-Cal, Thorlabs) in the cell, in the same position as the exposed area of the photoelectrode. Because all of the photoelectrodes were bottom-facing, a broadband reflection mirror (Newport dielectric mirror, 10Q20PR-HR) was used to direct the light beam from the horizontal to the vertical direction. For non-aqueous tests in methanol, the cell was assembled in an Ar-filled glove box, but photoelectrodes were measured outside the glove box while the cell was purged with Ar. All of the data presented for electrochemical measurements in aqueous solutions did not include compensation for the series resistance of the solution.

Cyclic voltammetry, quantum yield, and electrochemical impedance spectroscopy data were obtained using a Biologic SP-200 potentiostat (Bio-Logic Science Instruments). The stability test data were obtained using a Biologic MPG-2-44 potentiostat (Bio-Logic Science Instruments). The cyclic voltammetric data was recorded at a constant rate of 40 mV s^{-1}. The external quantum yield data were collected with the potentiostat connected to a lock-in amplifier while scanning the wavelengths produced by a monochromated light source were chopped at a frequency of 20 Hz.

B.7 Measurement of Faradaic efficiency for production of O_2:

To monitor the concentration of O_2 throughout the experiment, a Neofox fluorescence probe (Foxy probe, Ocean Optics) was used in an airtight cell with a side-facing quartz window. The measured concentration of O_2 was calibrated against the standard concentration of oxygen in water (7700 μg L^{-1} or 2.4×10^{-4} M) under a standard 20.9% (by volume) oxygen atmosphere. The reference electrode was a Hg/HgO/1.0 M KOH electrode and the counter electrode was a Pt mesh (Alfa-Aesar, 100 mesh, 99.9% trace metal basis), which was placed in a fritted compartment. The cell had a volume of 43.6 mL and was purged with a stream of ultra-high purity Ar (g) for ~ 1 h before data collection. The geometric area of the working electrode was ~ 0.6 cm^2, and the current was maintained at 0.30 mA to prevent the formation of bubbles on electrode surfaces. The amount of oxygen generated versus time assuming 100% Faradaic efficiency was calculated by converting the charge passed into coulombs by multiplying the current passed (in mA h as measured by the potentiostat) by 3.6, and then converting to units of μg O_2 by multiplying by the

charge passed by 83 (because 83 is the conversion factor for 1 coulomb of electrons to micrograms of O_2).

B.8 Transmission-electron microscopy (TEM):

Samples were prepared for cross-sectional TEM using conventional polishing and milling techniques. Cross-section samples were mounted on Mo slot grids (SPI Supplies) with an M-Bond 610 adhesive. The samples were then manually polished with diamond lapping film discs (Allied High Tech Products, Inc.). The samples were further polished with a dimpling machine (E.A. Fischione Instruments, Inc.), and final thinning was performed with Ar ion milling. TEM and scanning-TEM (STEM) imaging were performed with an FEI Tecnai F30ST microscope with an accelerating voltage of 300 kV. Energy-dispersive spectroscopy (EDS) line scans were collected in STEM mode using an Oxford energy-dispersive x-ray detector.

B.9 UV-Visible absorptance measurements:

The optical absorptance of metal-oxide-coated silicon samples was indirectly determined by separately measuring the total reflectance and transmittance using an Agilent Cary 5000 UV-Vis spectrometer, and subtracting the measured values from unity.

B.10 Atomic-force microscopy:

Atomic-force microscopy (AFM) was performed using a Bruker Dimension Icon operating in ScanAsyst mode with Bruker ScanAsyst-Air probes (silicon tip, silicon nitride cantilever, spring constant: 0.4 N/m, frequency: 50-90 kHz) for n-Si, n-Si/$SiO_{x,RCA}$/Co_3O_4 and n-Si/$SiO_{x,RCA}$/Co_3O_4/NiO_x, and operating in KPFM-FM mode with Bruker PFQNE-AL probes (silicon tip, silicon nitride cantilever, spring constant: 0.4-1.2 N/m, frequency: 200-400 kHz) for n-Si and n-Si/Co_3O_4. The scan size was 500 nm×500 nm and 3 μg×3 μg for the ScanAsyst and KPFM-FM modes, respectively. The images were analyzed using NanoScope Analyst software (version 1.40).

B.11 X-Ray Photoelectron Spectroscopy:

X-ray photoelectron spectroscopic (XPS) data were obtained using an AXIS Ultra DLD instrument (Kratos Analytical), at a background pressure of 1×10^{-9} Torr. High-intensity excitation was provided by monochromatic Al K_α X-rays that were 1486.6 eV in energy with a 0.2 eV resolution at full width at half-maximum. Photoelectrons were collected at the surface normal using a retarding (pass) energy of 20 eV. The peak energies were calibrated against the binding energy of the adventitious C 1s peak, which was taken to be 284.5 eV.

B.12 Grazing incidence X-ray diffraction:

Grazing incidence X-ray diffraction analysis was performed using Bruker D8 Discover system equipped with 2-dimentional Vantec-500 detector. Cu-K radiation (1.54 A) was generated at a tube voltage of 1 kV and a tube current of 50 mA. The incident beam was focused with a mono-capillary collimator. A laser beam marked the focal spot on the specimen fixed on an xyz stage. The scattered diffraction was registered by a 2-dimensional detector with an angular resolution < 0.04 degrees, and enabled the simultaneous detection of the diffraction data in a 2theta range of 5 degrees. The detected radiation was counted for 2000 s to obtain an appropriate XRD profile. Data were analyzed with Bruker EVA software.

B.13 Growth of III-V dual junction photoabsorbers

The tandem-junction III-V device was grown commercially (Sumika Electronic Materials, Inc.) according to specifications determined by 1-D numerical simulation using Helmholtz-Zentrum Berlin's AFORS-HET software. Planar III-V layers were grown epitaxially by metal-organic chemical-vapor deposition (MOCVD) on an n^+-GaAs wafer that had a (100)-oriented polished surface (Si-doped, acceptor concentration of 1×10^{19} cm^{-3}, 6" diameter). Detailed information on the cell stack, including the thickness and the dopants for the III-V layers, has been provided previously[5].

B.14 Atomic-layer deposition of TiO_2 layer

Atomic-layer deposition (ALD) of TiO_2 was conducted at 150 °C using tetrakis (dimethylamido) titanium (TDMAT, Sigma-Aldrich, 99.999%, used as received) and H_2O (>18.2 $M\Omega - cm$ resistivity, Millipore) in an Ultratech Fiji 200 plasma atomic-layer deposition system. Prior to ALD, the epitaxial surface was immersed in 1.0 M KOH(aq) (aqueous solution of potassium hydroxide pellets, semiconductor grade, 99.99% trace metal basis, Sigma-Aldrich) for 30 s, rinsed with copious amounts of H_2O, dried using a stream of N_2(g), and loaded immediately into the ALD chamber. An ALD cycle consisted of a 0.06 s pulse of H_2O, a 15 s purge under a constant 0.13 L min^{-1} flow of research-grade Ar(g), a 0.25 s pulse of TDMAT, and another 15 s Ar(g) purge. ALD-TiO_2 films with thickness of 62.5 nm were used to protect III-V surfaces.

B.15 Ohmic contacts and deposition of Ni

Ohmic contact to the n^+-GaAs wafer was formed using a Ge-Au eutectic (20 nm Ge/ 30 nm Au/ 15 nm Ni/ 100 nm Au) deposited by radio-frequency (RF) sputtering. The contact layers were annealed under N_2(g) at 400 °C for 30 s using rapid thermal annealing

(RTA) with a ramp-up rate of 40 °C s^{-1}. For all photoanode surfaces, an optically transparent nominally 2 nm thick Ni film was deposited on TiO_2 via RF sputtering from a Ni target (Kurt Lesker, 2" diameter × 0.125" thickness, 99.95%) using an AJA high-vacuum magnetron sputtering system. The Ar flow was kept at 10 sccm, while the working pressure was held at 5 mTorr. A deposition rate of ~0.1 A s^{-1} was maintained by adjusting the sputtering power on the Ni target.

ALD-deposited amorphous TiO_2 coatings have been used on various single crystalline substrates, including Si, III-V and II-VI compound semiconductors previously, and have showed excellent ohmic behavior due to similar growth chemistry. Degenerately doped Si substrates with an acceptor concentration > 10^{19} cm^{-3} p^+-Si were used in this study as the dark electrode control sample, to be consistent with the actual sample that had a window layer consisting of a 30-nm p^+-$In_{0.48}Al_{0.57}P$ and a 7-nm thick p^+-GaAs with acceptor concentrations > 10^{19} cm^{-3}. The tandem III-V n-type photoelectrode was rectifying in the dark and therefore could not be used as a reliable reference for the behavior of the photoelectrode under illumination[6]. The J-E behavior of the p^+-Si/TiO_2/Ni dark electrode effecting the OER in 1.0 M KOH(aq) thus provided a measure of the OER overpotential properties of the Ni-containing catalyst on a relevant substrate.

B.16 Preparation of Pd/C electrodes

The preparation of electrodes comprising Pd/C on a Ti mesh was similar to that reported previously for Pd/C on a Ti foil electrode[7]. A Ti mesh was first cut into 0.04 cm^2 pieces. Five pieces of Ti mesh were stacked and stringed together with a Ti wire. The stacked Ti mesh was etched in boiling 10% oxalic acid, rinsed thoroughly with H_2O, and dried overnight 75 °C in an oven. 4.8 mg of Pd/C powder was then mixed with 2.4 ml isopropanol and 40 μL 10 wt.% Nafion and the mixture was sonicated for > 30 min. The resulting solution was drop-dried onto the Ti mesh, with a Pd mass loading of 250 μg cm^{-2}. The Pd mass loading of Pd/C coated Ti foil reported previously was 50 μg cm^{-2}. As a comparison, a Pd/C nanoparticle-coated Ti foil electrode was made using the same conditions as on the Ti mesh except that the Pd mass loading was 50 μg cm^{-2}.

B.17 Preparation of III-V dual junction photoanodes

The ohmically contacted tandem-junction wafers were cleaved into samples that were ~ 0.1 cm^2 area. Ag paste was then used to attach the ohmic contact to a coiled, tin-plated Cu wire (McMaster-Carr) which was then threaded through a glass tube (Corning Inc., Pyrex tubing, 7740 glass). The samples were encapsulated and sealed to the glass tube using grey epoxy (Hysol 9460F). The epoxy was allowed to dry under ambient pressure for > 12 h.

The exposed electrode surfaces were imaged with a high-resolution optical scanner (Epson perfection V370 with a resolution of 2400 dpi) and the areas were measured using ImageJ software. Electrodes were ~ 0.03 cm^2 in photoactive area unless specified otherwise.

B.18 3-electrode measurements

For electrochemical measurements in 2.8 M $KHCO_3$(aq), a Ag/AgCl/1.0 mol/kg KCl electrode was used as the reference electrode, and a Pt mesh was used as the counter electrode. The Ag/AgCl/1.0 mol kg^{-1} KCl electrode had a potential of 0.235 V vs the normal hydrogen electrode (NHE). The pH of the CO_2-saturated 2.8 M $KHCO_3$(aq) solution was 8.0, as measured by a VWR SympHony SB70P Digital, Bench-model pH Meter. The equilibrium potential for the $CO_2/HCOO^-$ redox couple at pH 8 is 0.02 V versus the reversible hydrogen electrode (RHE)[8]. Therefore, the equilibrium potential for CO_2 reduction to formate in CO_2-saturated 2.8 M $KHCO_3$(aq) solution was calculated to be -0.687 versus Ag/AgCl/1.0 mol kg^{-1} KCl. Figure 4.2A shows the configuration of 3-electrode electrochemical measurement. Two custom-made three-necked cells were used in the 3-electrode measurement. The BPM was used for prevention of formate product cross-over, and to prevent the formate from being oxidized at the counter electrode. The electrolyte was vigorously agitated with a magnetic stir bar driven by a model-train motor (Pittman) with a Railpower 1370 speed controller (Model Rectifier Corporation). The data presented for electrochemical measurements in aqueous solutions does not include compensation for the series resistance of the solution. CO_2(g) was bubbled into the $KHCO_3$ solution during electrochemical measurements, to prevent oxygen dissolution. Cyclic voltammetric data (10 mV s^{-1} scan rate) were obtained with a Biologic MPG-2-44 potentiostat (Bio-Logic Science Instrument).

B.19 2-electrode measurements

The configuration for 2-electrode measurements was similar to that used to obtain 3-electrode measurements (Figure 4.9). In addition to the stirring described above, a peristaltic pumping system (Simply Pumps PM300F) with a minimum flow rate of 500 mL min^{-1}, as controlled by a tunable power supply, was used to facilitate the removal of CO_2 bubbles at the BPM surface, and to minimize the voltage loss at the BPM caused by bubbles. The BPM in this configuration was replaced as required by a Nafion membrane for additional 2-electrode measurements. For photoelectrochemical experiments, a Xe arc lamp (Newport 67005 and 69911) equipped with an IR filter (Newport 61945) and with an AM 1.5 filter (Newport 81094 and 71260) was used as the light source for J-E measurements. The intensity in the solution-containing cell was then calibrated by placing

a Si photodiode (FDS100-Cal, Thorlabs) with a similar area as that of the photoanode (0.03 cm^2) in the custom-made three-necked beaker with flat quartz windows, with the Si located at nominally the same position as that occupied by the exposed area of the photoelectrode. The Si photodiode had been previously calibrated by measurement of the short-circuit current density under 100 mW cm^{-2} of AM 1.5 simulated sunlight. The voltage scan range was confined to be more positive than the onset of photoanodic current, to ensure a constant direction of ionic current flow in the membrane. The areas for the photoanode, BPM, Nafion membrane and Pd/C cathode were 0.03 cm^2, 0.03 cm^2, 0.03 cm^2, 0.04 cm^2, respectively. A 0.2 cm diameter hole was punched at the middle of a piece of rubber using a hole making tool. An O-ring with 0.2 cm diameter was glued with epoxy on the rubber with the hole aligned. The BPM was right between two pieces of rubber, and the hard rubber/O-ring/BPM/O-ring/hard rubber was tightly clamped between the two cells as shown in Figure 4.9.

B.20 Four-point measurement system for the bipolar membrane

The four-point measurement setup was similar to that used for the 2-electrode measurement (Figure 4.2B). Two Luggin capillaries with Ag/AgCl/1.0 mol kg^{-1} KCl reference electrodes were used to measure the potential near the membrane. A peristaltic pumping system was also used in these experiments to facilitate the removal of CO_2 bubbles from the BPM surface, and to minimize the voltage loss at the BPM caused by bubbles and concentration gradients. The BPM in this configuration could be replaced by Nafion membrane as appropriate for four-point measurements of the Nafion membrane. The voltage loss at 10 mA cm^{-2} was lower than previously measured[9], due to the use of Luggin capillaries as well as an efficient pumping system.

B.21 ICP-MS potassium ion crossover measurements

To measure the potassium ion crossover from the anolyte to the catholyte through the BPM, the $KHCO_3$ catholyte was replaced by $CsHCO_3$ (Sigma-Aldrich, 99.9% trace metals basis). Two Pt mesh electrodes were used as the source and drain electrodes during the potassium ion crossover tests. The potassium ion concentrations in the catholyte in a 2-electrode BPM configuration were determined as a function of time by Inductively Coupled Plasma - Mass Spectrometry using an Agilent 8800 spectrometer. The sample-introduction system consisted of a MicroMist nebulizer with a Scott-type spray chamber. A fixed-injector quartz torch was used with a guard electrode, and the plasma was operated at 1500 W. In addition to use of single-quad (MS) mode with no gas, elements were determined by MS-MS modes in which different collision or reactive gases were present

in the gas cell located between the quadrupoles. These modes were no-gas, He, H. External standards were used to quantify the analytes determined.

B.22 TIC/TOC carbonate ion crossover measurements

To measure the carbonate ion crossover from the catholyte to the anolyte through the BPM, the anode chamber was sealed and purged with O_2(g) (ALPHAGAZ 1) to prevent sorption of CO_2(g) from ambient air. Samples were analyzed for total inorganic carbon (TIC) using an OI Analytical Aurora Total Organic Carbon Analyzer. Briefly, a sample aliquot was combined with phosphoric acid and heated in a closed vessel. At the end of the reaction time, carbon dioxide was swept out of the vessel by a purge of N_2(g). The gas stream was dried and passed through a non-dispersive infrared (NDIR) detector. The instrument was calibrated against potassium hydrogen phthalate that had been oxidized to form carbon dioxide by heating persulfate, after removal of TIC as described above. For these experiments, the instrument was calibrated and showed a linear response between 5 and 50 ppm.

B.23 Faradaic efficiency for formate generation

^{1}H-NMR spectroscopy was performed on a Bruker 400 MHz Spectrometer to quantify the amount of formate generation. Standards of 40 to 500 μM sodium formate solutions were prepared by serial dilution, and were used to calibrate the instrument (Figure B.1). In general, 100 μL of 0.0800 vol.% 1,1'-dimethylformamide, DMF (internal standard), in H_2O were added to a 2 mL aliquot of the standard solution. 0.5 mL of this solution was then transferred to a NMR tube that contained 200 μL of D_2O. A water suppression method was used to suppress the signal of the water in the electrolyte and to allow visualization of the formate peaks. The same procedure was used to quantify the formate product, with 100 μL of 0.0800 vol.% DMF solution added to 2 mL of the electrolyte after electrolysis, and 0.5 mL of the solution added in a NMR tube with 200 μL of D_2O.

References

[1] H. B. Gray, D. N. Hendrickson, and Y. S. Sohn. "Magnetic Susceptibility Study of Various Ferricenium and Iron(III) Dicarbollide Compounds". In: *Inorg. Chem.* 10.8 (1971), pp. 1559–1563.

[2] K. Sun et al. "Sputtered NiOx Films for Stabilization of p+n-InP Photoanodes for Solar-Driven Water Oxidation". In: *Adv. Energy Mater.* (2015), p. 1402276.

[3] K. Sun et al. "Stable Solar-Driven Oxidation of Water by Semiconducting Photoanodes Protected by Transparent Catalytic Nickel Oxide Films". In: *Proc. Natl. Acad. Sci. U.S.A.* 112 (2015), pp. 3612–3617.

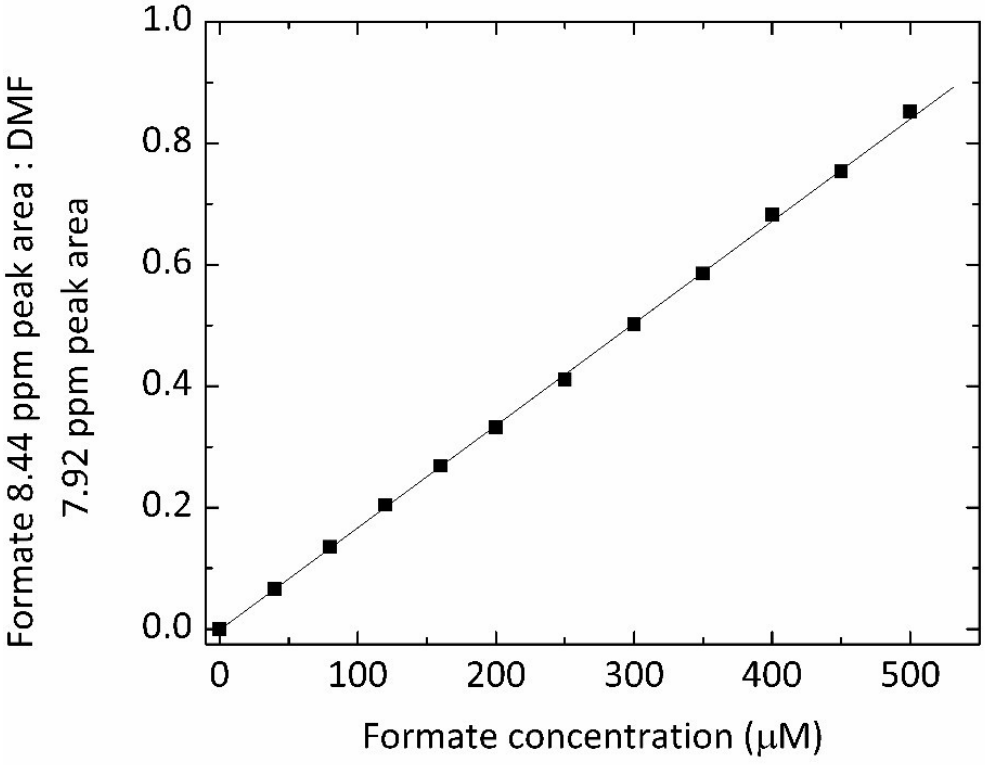

Figure B.1: Formate concentration calibration curve: the ratio of the formate 8.44 ppm peak area and the DMF 7.92 ppm peak area as a function of formate concentration. (R^2 = 0.9996)

[4] K. Sun et al. "Stable Solar-Driven Water Oxidation to O2(g) by Ni-oxide Coated Silicon Photoanodes". In: *J. Phys. Chem. Lett.* 6 (2015), pp. 592–598.

[5] E. Verlage et al. "A Monolithically Integrated, Intrinsically Safe, 10% Efficient, Solar-Driven Water-Splitting System Based on Active, Stable Earth-Abundant Electrocatalysts in Conjunction with Tandem III-V Light Absorbers Protected by Amorphous TiO2 Films". In: *Energy Environ. Sci.* 8.11 (2015), pp. 3166–3172.

[6] R. H. Coridan et al. "Methods for Comparing the Performance of Energy-Conversion Systems for Use in Solar Fuels and Solar Electricity Generation". In: *Energy Environ. Sci.* (2015).

[7] X. Min and M. W. Kanan. "Pd-Catalyzed Electrohydrogenation of Carbon Dioxide to Formate: High Mass Activity at Low Overpotential and Identification of the Deactivation Pathway". In: *J. Am. Chem. Soc.* 137.14 (2015), pp. 4701–4708.

[8] R. Kortlever et al. "Electrochemical CO2 Reduction to Formic Acid at Low Overpotential and with High Faradaic Efficiency on Carbon-Supported Bimetallic Pd–Pt Nanoparticles". In: *ACS Catal.* 5.7 (2015), pp. 3916–3923.

[9] K. Sun et al. “A Stabilized, Intrinsically Safe, 10% Efficient, Solar-Driven Water-Splitting Cell Incorporating Earth-Abundant Electrocatalysts with Steady-State pH Gradients and Product Separation Enabled by a Bipolar Membrane”. In: *Adv. Energy Mater.* 6.13 (2016), p. 1600379.

INDEX